The opportunity for synchrophasors in monitoring sources of renewable energy integrated into distribution networks

RA Lotriet

22078630

Dissertation submitted in fulfilment of the requirements for the degree *Magister* in Electrical and Electronic Engineering at the Potchefstroom Campus of the North-West University

---

Supervisor: Prof APJ Rens

December 2015

The Stone Age did not end because we ran out of stones; we transitioned to better solutions. The same opportunity lies before us with energy efficiency and clean energy.

Steven Chu

Nobel Prize winner

Preface

The contents of this dissertation presents the opportunity to monitor large-scale renewable energy sources integrated into distribution networks using micro-synchrophasor measurements.

The research presented henceforth was conducted under the supervision and guidance of Professor A.P.J. Rens at the North-West University School for Electric, Electronic and Computer Engineering.

Metrological work was performed using IEC 61000-4-30 Class A, ed. 3 certified Power Quality recording instruments comprising embedded synchrophasor technology.

International cooperation with the University of Ghent was performed in the testing of micro-synchrophasor metrological capabilities at a test laboratory located in Kortrijk, Belgium.

Field data was obtained from a real-life grid connected 75 MW PV power plant integrated onto a distribution network at 132 kV. Research was conducted during the period when large-scale renewable power plants were added to the South African power grid through the Government-supported REIPPP programme.

Results presented in this dissertation are of interest to parties associated with power system operations, such as those who manage grid operation, assesses network power quality and affiliate with the renewable energy sector.

This dissertation is submitted for the requirements of Magister in Electrical and Electronic Engineering. Research was conducted between January 2014 and November 2015. The work presented in this dissertation is original research conducted by the author, R.A. Lotriet.

Acknowledgements

To my wife, Beanca, for morally supporting me in all my endeavours form start to finish.

To my study leader, Professor Johan Rens, for the supervision and guidance he has provided throughout the course of my research.

For the instrumentation provided, I wish to thank Charl Marias and Willie van Wyk from CT Lab (Pty) Ltd.

Special recognition to Professor Jan Desmet, Colin Debruyne, Cis Vansteenberge and Jurgen van Ryckeghem from the University of Ghent, Belgium for assistance on tests conducted at their laboratories in Kortrijk.

For all the prayers and support from my parents, Ronnie and Wilma; also to my friends, colleagues and the rest of my family for all their continuous support and motivation.

And to the greatest study leader of all, Jesus Christ, for the grace He has given me.

Abstract

Synchrophasor measurements have traditionally been reserved for monitoring the operation of transmission systems. This technology enabled direct supervision over transmission system operation without any complex estimation modelling. As a result, system operators could better manage the operational stability in transmission systems.

With significant developments occurring in distributions networks, specifically the integration of renewable power plants (RPPs), synchrophasor monitoring at distribution level have become of interest. Distribution network operation generally have smaller voltage phase angle differences, which would require higher metrological capabilities in synchrophasors.

The concept of high-precision synchrophasor measurements with time synchronisation accuracies better than a μ-second is known as a micro-synchrophasor. High-resolution recording capabilities of micro-synchrophasors enable the detection of voltage phase angle offsets between two locations at fractions of a degree. This research demonstrates the usefulness of the micro-synchrophasor to quantify the interaction between a PV power plant and the distribution network it integrates with, which would provide a better understanding on the impacts of RPPs on distribution networks.

The metrological capabilities of the recording instruments used in this research were first tested and verified for micro-synchrophasor level recordings. During the tests, the practical viability of micro-synchrophasor measurements were also validated. After the tests, micro-synchrophasor field recordings were performed at a 75 MW PV power plant feeding into a kV distribution grid. The field data was then used to visualise the steady-state and voltage stability levels between the PV plant and upstream distribution station over a period of 24-hours.

Results were analysed to study the impact of a RPP integrated onto a distribution network, which demonstrated the opportunity for micro-synchrophasors to monitor renewable energy sources integrated in distribution networks.

Keywords: *Synchrophasor, Distribution Network, Renewable Energy, Photovoltaic (PV).*

Table of Contents

List of Figures

List of Tables

Nomenclature

List of Abbreviations

AC	Alternating Current
ANSI	American National Standards Institute
BVI	Bus Voltage Improvement
C	Capacitance
CT	Current Transformer
DC	Direct Current
DoE	Department of Energy
DSO	Distribution System Operator
DTFT	Discrete Time Fourier Transform
ESKOM	Electricity Supply Commission of South Africa
FE	Frequency Error
GPS	Global Positioning System
HV	High Voltage
IEEE	Institute of Electric and Electronic Engineering
IEC	International Electrotechnical Commission
IG	Induction Generator
IPP	Independent Power Producer
KCL	Kirchhoff's Current Law
KVL	Kirchhoff's Voltage Law
L	Inductance
LV	Low Voltage
MPP	Maximum Power Point
MV	Medium Voltage
NDP	National Development Plan
NERSA	National Energy Regulator of South Africa
NIPS	National Integrating Power System
NRS	National Regulatory Standards
P-V	Power-Voltage

PMU	Phasor Measurement Unit
pf	Power Factor
PFC	Power Factor Correction
PLC	Programmable Logic Controller
PMSG	Permanent Magnet Synchronous Generator
POC	Point of Connection
PQ	Power Quality
PT	Potential Transformer
PV	Photovoltaic
PWM	Pulse Width Modulation
QoS	Quality of Supply
R	Resistance
RES	Renewable Energy Source
REIPPP	Renewable Energy Independent Power Producer Procurement
RMS	root-mean-square
ROCOF	Rate of Change of Frequency
RPP	Renewable Power Plant
SAPVIA	South African Photovoltaic Industry Association
SCDR	Symmetrical Component Distance Relay
STC	Standard Test Conditions
SQL	Structured Query Language
STATCOM	Static var Compensation
SCDR	Symmetrical Component Distance Relay
TVE	Total Vector Error
UL	Underwriters Laboratory
UTC	Coordinated Universal Time
VSC	Voltage Source Converter
VSM	Voltage Stability Margin
VT	Voltage Transformer
VTHD	Voltage Total Harmonic Distortion
XLPE	Cross Linked Polyethylene

List of Units

A	ampere
AM	Air Mass
C	celsius
F	farad
H	henry
hPa	hectopascal
Hz	hertz
k	kilo
M	Mega
G	Giga
m	milli
n	nano
s	Seconds
μ	micro
VA	Volt-Ampere
V	Volt
VA	Volt-Ampere
var	Volt-Ampere Reactive
W	watt
Wh	watt-hour
W/m^2	Watt per square meter
Ω	ohm

List of Symbols

ω	Angular Velocity
I	Current
β	Current Phase Angle
*	Conjugate
$^\circ$	Degrees
η	Efficiency
f	Frequency
$\overline{x}$	Mean Value
$\angle$	Phasor Angle
π	Pi
θ	Power Angle
σ	Standard Deviation
t	Time
V	Voltage
δ	Voltage Phase Angle
λ	Wave Length

Chapter 1: Introduction

1.1 Introduction

The introduction of synchronised phasor measurements provided engineers with a broad range of new monitoring applications that were previously not possible. Referred to as synchrophasors, these measurements allow visualisation over the true behaviour of a system, opposed to traditional state estimators that require complex iterative arithmetics.

Synchrophasors have been proven in transmission systems where the grid stability over hundreds of kilometres are centrally visualised. A similar need for synchrophasor supervision in distribution networks has emerged due to the widespread integration of distributed generation (DG), specifically in the form of renewable energy sources.

It is well known that the acquisition of renewable power plants (RPPs) poses concern over grid reliability and security. This is predominantly due to combination of stochastic generation increased power consumption has caused conventional operation of distribution network to become more dynamic.

The long-term perspective of using renewable energy sources is to serve as an asset to the power system, this not only includes incentives such as clean energy and environmental responsibility, but should also support secure network operation.

Resiliency of networks with integrated renewable energy sources can be improved by providing system operators with visibility over the interaction between RPPs and distribution networks. By introducing synchrophasors in distribution network monitoring the same sophistication in network supervision found in transmission systems can be achieved.

This chapter introduces the concept of using a high precision version of the synchrophasor, i.e. the micro-synchrophasor, to monitor the integration of RPPs in distribution networks. Background on the development of the renewable energy infrastructure in South

Africa is provided in the first section of this chapter. Afterwards, the historical advancements in synchrophasor technology leading up to the micro-synchrophasor are investigated.

The rest of this chapter discusses the presented research problem statement and formulates the empirical research methodology followed to address the fundamental research questions posed.

1.2 Background

1.2.1 Photovoltaic energy in South Africa

Concerns on limited fossil fuel reserves and the environmental impact thereof are a global concern. A rapid development of renewable energy sources (RES) followed as a result of incentives introduced by governing bodies. The potential in South Africa for establishing renewable energy are among the best in the world, especially for photovoltaic (PV) generation.

Over recent years South Africa set many goals in terms of renewable energy generation. The National Development Plan (NDP) laid emphasis on reducing greenhouse gas emissions by a 42% baseline by 2025 [1]. This goal serves as foundation to oversee the target of obtaining a RES capacity of 20 000 MW by 2030 [2].

South African RES predominantly comprises wind, PV, concentrated solar power (CSP), hydro and landfill gas. From the proposed 20 000 MW, 8 400 MW would consist of cumulative PV generation and in conjunction with the aimed 1 200 MW from CSP; solar energy will comprise 45% of total RES [3]. Rational behind the feasibility of solar energy is justified by South Africa's favourable irradiance conditions, illustrated in Figure1-1.

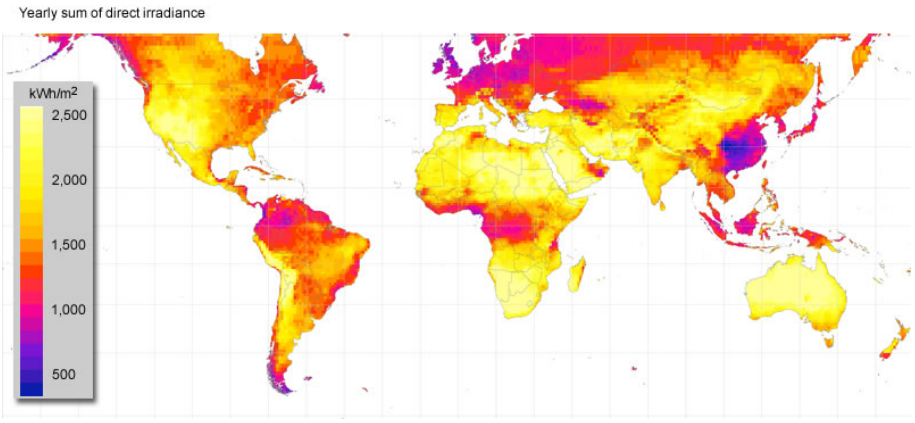

Figure 1-1: Global irradiance levels in kWh/m^2 [4]

On average South Africa experiences 2 500 hours of annual sunlight, providing daily irradiance levels of up to 2.5 kWh/m^2 [5]. These conditions provide viable investment opportunities for PV energy development, which were recently brought on by tenders that the Government set out for Independent Power Producers (IPPs) to construct and integrate PV power plants onto local distribution networks.

With Renewable Power Plant (RPP) tenders initiating its third phase, the Government have identified PV energy as the most favourable form of distributed generation, as stipulated in the Integrated Resource Plan for Electricity [6]. Considering the ongoing struggle of Eskom to supply sufficient power and the global migration towards renewable energy solutions, IPPs are finding themselves in a favourable position in South Africa.

1.2.2 Monitoring renewable energy sources in distribution networks

PV is one of several forms of distributed generation (DG) connected to the power system. The acquisition of DG, predominantly in the form of renewable energy sources, have started to gain momentum over the past decade, due to the reduction in associated costs, global pressure on sustainability and relative simplicity in installation.

The widespread installation of RPPs have started to cause a decentralisation in power generation. Moreover, these new energy sources generally tend to integrate in distribution networks. This caused a number of challenges since power generation is now occurring much closer to the downstream customer and the infrastructure of distribution networks are not designed for power flow in both directions.

For the generation of distributed energy sources to be considered reliable, the existing distribution network and regulation of the network need to be smarter. The Institute of Electrical and Electronics Engineers (IEEE) defines the term smart grid as the integration of power, communications and information technologies for an improved electric power infrastructure serving loads while providing for an ongoing evolution of end-use applications [7].

A smart grid manages electricity demand and its various forms of generation in a steadfast manner and can actively balance energy demand with supply. This would essentially require the addition of an intelligent monitoring system over distribution network operation that would attribute towards the following [8]:

- Load demand and response optimisation
- Visibility over network stability in real-time
- Advancements in fault analysis
- Substation control and management automation
- Situational awareness over production of distributed sources

In technical terms, the integration of RPPs have four parameters that must be actively managed to secure network operation, which are the voltage phase angle (δ), voltage magnitude (V), real power (P) and reactive power (Q).

By controlling these parameters between the RPP and the point of integration, the generated power can be distributed securely across the network. However, the utilisation of such monitoring and management systems have not yet been included in distribution networks, since power system stability was only managed at transmission system levels.

To achieve a similar level of supervision in distribution networks with integrated RPPs, the same technology used at transmission systems must be incorporated here. One of the most profound smart grid technologies that are currently used for advanced supervision and control optimisation in transmission systems are phasor measurement units (PMUs).

PMUs are instruments that record time-synchronous phasor measurements, termed synchrophasors. These type of measurements have improved visibility of transmission system operation [9].

Such improvements have made transmission system operations more reliable, since steady-state parameters (δ, V, P, Q) can now be directly recorded using synchrophasors, which eliminates the need for any complex and possibly inaccurate state estimations.

With the resounding success of synchrophasor monitoring in transmission systems, the application into distribution systems have become attractive [10]. It is anticipated that the implementation of synchrophasors in distribution systems would provide a better understanding in the integration of renewable energy sources.

1.2.3 Historical advancements of synchrophasors

Synchrophasors refers to measurements of fundamental frequency voltage and current phasors synchronised with Coordinated Universal Time (UTC), using time-stamping units such as Global Positioning System (GPS) tracking [11].

In the IEEE C37.118.1 Standard for Synchrophasor Measurements, a synchrophasor is defined as a phasor that is calculated from data samples recorded at a standard time signal as measurement reference [12].

The term phasor, first described by Charles Steinmetz in 1893, presented a novel means of quantifying power parameters by representing the amplitude, frequency and phase angle parameters of a sinusoidal waveform as a complex number [13].

The history of synchrophasor development is attributed by the following important stages [14]:

a) Symmetrical Component Distance Relay (SCDR) Development

b) First Sampling Clock Synchronisation

c) Introduction of the Phasor Measurement Unit (PMU)

d) Synchronised Wide Area Monitoring Field Application

After the 1965 power blackout in the United States a need for improved visibility of the power system emerged. The SCDR, presented in 1979, presented a new means in power

measurements by being the first relay to measure symmetrical components [15].

This provided ground-breaking applications such as fault location detection, protective relaying and instantaneous unbalance measurements. As a result, investigation in wide area visibility recording soon followed.

Initial synchronous data sampling was implemented by synchronising the internal sampling clocks towards UTC, which is the reference point from which all time is regulated globally. By applying UTC synchronisation the sampled phasor data used the same time reference. This made the comparison of data measured in different places possible [14].

With the advent of GPS time stamping further advancements in local time reference were made. This systematically replaced the use of radio clock time synchronisation, where local time was received by terrestrial time signals through longwave transmission.

By applying GPS time-stamping for clock synchronisation data measurements were synchronised towards UTC within a time offset of less than 1 second. [14].

The first prototype Phasor Measurement Unit (PMU), presented in 1988 at Virginia Polytechnic Institute, was derived from the SCDR estimation algorithm. Comprising more sophisticated processing and an internal GPS receiver, this instrument was capable of conducting the first synchrophasor measurements [16].

After this prototype was commercially manufactured the IEEE standard 1344 *Synchrophasor* was introduced as the first standard defining compliance requirements for synchronised PMU recordings.

Over the past decade, the accuracy of synchrophasor estimators and the certainty in time-stamping synchronisation improved. This initiated the implementation of synchrophasors in transmission systems to also increase.

But it was not until recent events, such as the 2011 blackouts in the United States, that a need for wide area monitoring and predictive tools development have emerged. This caused a global trend in the implementation of synchrophasors to provide improved net-

work visualisation [17].

Figure 1-2 illustrates the increase in PMUs for synchrophasor measurements in the United States between 2012 and 2015.

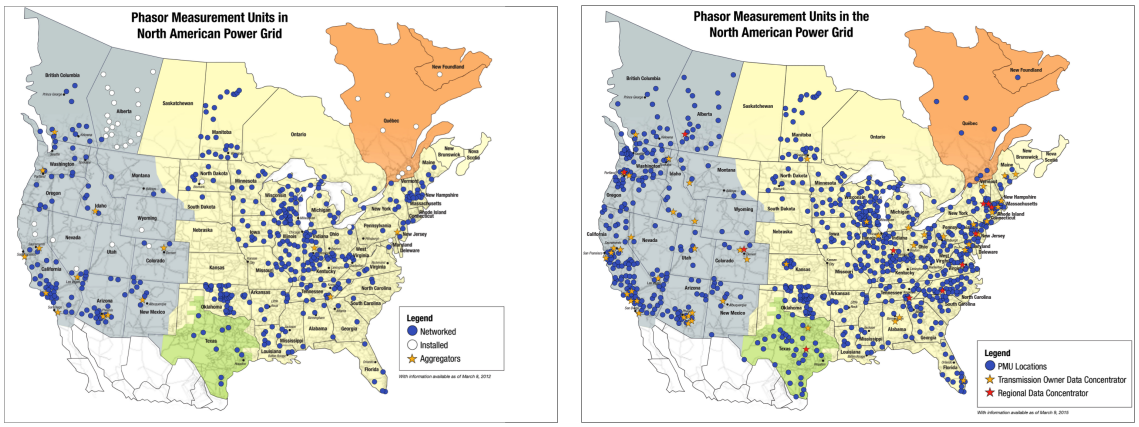

(a) Installed PMUs in 2012

(b) Installed PMUs in 2015

Figure 1-2: Increase in installed PMUs on the United States transmission system [18]

Synchrophasors are now the transmission system monitoring application of choice. They comprise the capacity to provide real-time stability supervision over transmission networks, opposed to conventional models that require complex calculations to estimate the state of network operation.

Continuous advancements in synchrophasor technologies pertaining to sampling resolution and clock accuracies, enable PMUs to detect smaller phase angle values at a high certainty. Such advancements enabled engineers to start exploring the application of high precision synchrophasors for advanced distribution network monitoring purposes [10].

1.2.4 Introduction of the micro-synchrophasor

Distribution networks are subject to many developments such as widespread distributed sources and ever-expanding downstream load connections. As a result network behaviour has become dynamic, making it reasonably complex to manage.

It is therefore proposed that the same operational visibility found in transmission systems are now required for distribution networks. With persistent improvements being done on synchrophasor technologies, PMU measurements have become capable of measuring discrepancies at distribution voltage level.

The concept of the micro-synchrophasor was first introduced in 2014 [19] and refers to high resolution synchrophasors able to record at synchronised clock accuracies in the order of μ-seconds.

Instruments capable of micro-synchrophasor measurements are also referred to as μPMUs and have predominantly been developed for operational visibility over distribution networks. The concept of how distribution network operation can be visualised by means of micro-synchrophasor measurements is illustrated in Figure 1-3.

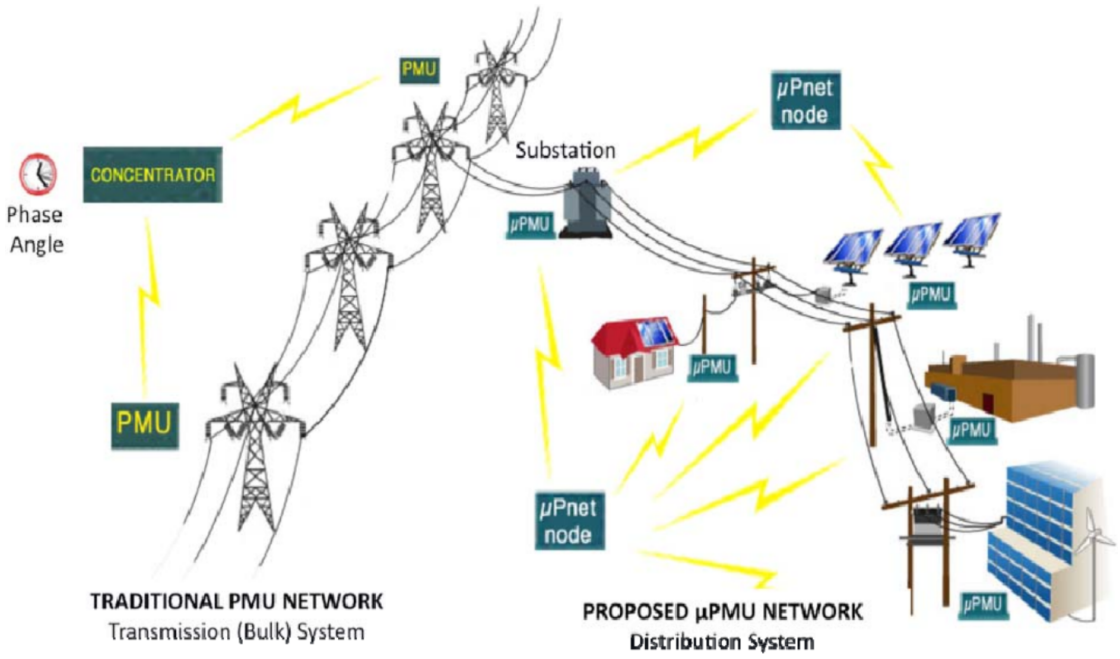

Figure 1-3: Concept of distribution network supervision with micro-synchrophasors [19]

The predominant difference between synchrophasor supervision in transmission systems and micro-synchrophasor supervision in distribution networks is the measurement resolution required to conduct small angular difference recordings. In distribution networks the voltage phase angle between two locations will be significantly smaller due to reduced impedance magnitudes.

It is therefore essential for micro-synchrophasor measurements to comprise the needed accuracy and resolution to effectively monitor at the same quality on which transmission systems is monitored.

A big challenge for the implementation of micro-synchrophasors is the economical feasibility surrounding the technology. At transmission levels the cost of PMUs are justified by the need to monitor large amounts of energy transported over long distances.

In distribution networks the energy being transported is much less, which causes a predicament since synchrophasor-based supervision in distribution networks requires more advanced recording capabilities than conventional PMUs.

A solution to this challenge was obtained by incorporating micro-synchrophasor measurements on instruments that comply with the IEC 61000-4-30 Class A, ed. 3 requirements.

This initiation made micro-synchrophasors in distribution networks feasible since the costs of installing dedicated μPMUs were eliminated. It also provides the added benefit of measuring micro-synchrophasor simultaneously with power quality (PQ) trends. Realisation of micro-synchrophasors led to a number of applications being identified [10]:

- Distribution network state estimation
- Large-scale DG and IPP integration monitoring
- Wide area visibility in real-time
- Residential generation supervision
- Stability analysis
- Post-mortem evaluation
- Micro-grid synchronisation control
- Protective relaying
- Fault induced delayed voltage recovery

With the continuous development on distribution networks, particularly the addition of large-scale RPPs operated by IPPs, the need for distribution network visibility with micro-synchrophasors will become equally import as transmission system supervision.

1.3 Problem statement

"The grid was not built for renewables."

- Trieu Mai
National Renewable Laboratory, Senior Analyst

1.3.1 Renewable energy integration onto distribution networks

Widespread integration of commercial RPPs lead to distribution networks attaining generation tasks traditionally reserved for transmission systems. These acquisitions caused concern involving network reliability due to challenges such as [20], [21]:

- Reverse power flow
- Protection coordination
- Stochastic changes influencing system instability
- Voltage harmonic distortion
- Supply and demand inequity
- Active and reactive power profile variations

Power generation by sources of renewable energy such as PV and wind is variable in principle due to changes in irradiance levels and wind speed. These variations are not only daily or seasonal patterns, but can be instantaneous when clouds move over PV panels or when the wind speed changes.

The flow of energy is also opposite to the normal direction by injecting energy at points in the network where it was designed for voltage drops. Detrimental effects associated with these stochastic production patterns caused a dispute revolving renewable energy integration in South African distribution grids.

The national utility, Eskom, have since taken conservative measures to allow renewable integration due to "technical issues" it introduces onto the grid, stated by dr Wolsey Barnard, acting director-general of the Department of Energy (DoE). Controversially, South African Photovoltaic Industry Association (SAPVIA) argued that in order to mitigate Eskom's capacity limit crisis, priority should be given to power plants that are the quickest to connect, such as PV generation that conforms to this requirement [22].

International experience has shown that concerns on network stability when connecting renewable power plants to distribution networks, are valid [23].

Careful consideration is required on the technology used in the interface between the RPP

and the network, the location of the plant, (fault levels) and how the network operator can retain control over voltage stability and QoS.

1.3.2 Monitoring renewable energy with micro-synchrophasors

The renewable energy paradigm comprises numerous characteristics, such as dynamic, stochastic, decentralized, variant in capacity and closer to the end consumer. Emergence of such qualities introduced to the power system has brought about new challenges for system operators.

Renewable energy sources characteristics requires special consideration due to the possibility of sudden changes. This changes are inflicted by variant climatic conditions imposed on the generation source, for example clouds and rain.

The variable output profiles of RPPs such as those from PV power plants have been associated with both detrimental and beneficial effects on local grid operation. For the distribution system operator to control network operation to be stable and reliable, a support platform providing situation awareness made possible by the micro-synchrophasor is needed.

The impedance between two points of coherent measurements (synchrophasors) in a distribution system can be relatively low. This results in smaller phase angle variation being measured between the synchronised phasors. To record these phase angles high precision recordings from the micro-synchrophasor instruments are demanded.

Micro-synchrophasors are a novel concept with metrological requirements not well defined and the ability of instrumentation to record it with sufficient certainty has not been validated. Therefore an empirical approach is applied in this research to determine if such requirements are indeed viable.

1.4 Research questions

1.4.1 Can micro-synchrophasors be used to monitor the performance of distribution systems with integrated PV generation?

This is the fundamental question posed for the research problem. Research on micro-synchrophasors predicted promising monitoring applications for RPP integration supervision in distribution networks[19], [10]. Micro-synchrophasors need to be validated in this context as a viable solution to monitor a PV power plant.

1.4.2 What are the metrological requirements for micro-synchrophasor measurements?

The significant difference between conventional synchrophasors and micro-synchrophasors is dictated by the recording resolution requirements while adhering to the IEEE standard C37.118.1-2011 for synchrophasor measurements [12]. PQ monitoring of distribution networks are well developed and these instruments are expected to be an affordable solution to distribution network operators if the same instrument can also record synchrophasor data.

With the time-synchronisation requirement of the third edition of the IEC61000-4-30 Class A PQ parameters implemented by means of GPS, PQ instruments can produce synchrophasor data in principle. Instruments with this capability are proposed for micro-synchrophasor implementation. These instruments are also and validated towards the opportunity of micro-synchrophasors in the research reported in this dissertation.

1.4.3 How does a PV power plant affect network stability?

Similar to other renewable energy sources, PV power plants produce stochastic output power profiles. PV power plants are however the most predictable renewable energy source since they solely rely on daily irradiance. The only abrupt change that PV generation could be subjected to is the loss of power due to cloud coverage or dust storms.

The impact of an integrated PV power plant on distribution network operation must be evaluated. It must be determined if the slow change in PV production bears any concern over network stability. The significance of an abrupt loss in PV power on network instability due to must also be evaluated.

1.5 Research objectives

1.5.1 Primary objective

The primary objective is to validate the opportunity for the micro-synchrophasor to support distribution network stability analysis.

Network coherent data can be used to derive the micro-synchrophasor. It presents the opportunity to track network stability. Given the success of synchrophasors in transmission system monitoring, ground-breaking applications of micro-synchrophasors at distribution levels are anticipated [19], [10].

1.5.2 Secondary objectives

1.5.2.1 Micro-synchrophasor resolution and constraints

Possible constraints to achieve the required resolution needs to be investigated as pertaining to the Class A requirements of IEC 61000-4-30, ed 3. Furthermore, the recording instrument's metrological capabilities must tested with high-precision signal generators to verify compliance with the proposed metrological requirements for micro-synchrophasor measurements [19] .

1.5.2.2 Visualisation of network stability

A platform containing the composition of diagrams to visually track stability with micro-synchrophasors that can prove beneficial for monitoring applications needs to be constructed. The intent of visual tracking is to provide a simplistic manner on which the state of operation can be diagnosed.

1.5.2.3 Steady-state and voltage stability diagnostics

PV generation comprises a dynamic profile subject to ambient changes. Depending on the PV power plant integration capacity, the network steady-state are susceptible to such changes. The steady-state stability must be visually tracked on a power-transfer curve so that the associated effects of PV production on the network steady-state can be assessed.

The impact on voltage stability in a distribution network also needs to be visualised that will assist with stability assessments. This can be done on a curve where the locus of active power is plotted against voltage, which is commonly known as a P-V curve (not the "PV" of photovoltaic).

The advantage of applying the micro-synchrophasor in tracking the operating point on power-transfer and P-V curves have to be evaluated.

1.6 Research methodology

The research methodology is categorised into three primary sections:

1. Test and validate the metrological capabilities of the instruments used for micro-synchrophasor measurements.

2. Perform conceptual analysis through theoretical integration analysis, simulation study with Simulink® and a real-life case study.

3. Analyse field recordings of micro-synchrophasor data obtained at a on a 75 MW PV power plant.

1.6.1 Validating the metrological requirements for micro-synchrophasors

The concept of what a micro-synchrophasor entails, is based on [19] and serves as benchmark for the metrological environment needed to practically record a micro-synchrophasor.

In this dissertation PQ instruments with the ability to synchronise data at different locations well enough to comply with the measurement specifications of the synchrophasor as set by the IEEE Std. C37-118.1 [12] are used as the field recorders.

These instruments sample the time-domain waveforms at 500 kHz and due to the precision by which time-stamping is implemented, perfectly align the 128 samples of each waveform used for the synchrophasor between zero crosses.

It is expected that these PQ instruments, which have time-stamp capabilities at an uncertainty better than 1 μs will be able to comply with the metrological micro-synchrophasors requirements.

Should the PQ instruments be verified to conduct micro-synchrophasor recordings, the usefulness of such recordings can be practically validated.

1.6.1.1 Metrological evaluation of micro-synchrophasor data

Evaluation of the recording instrument used to record micro-synchrophasor data was done by emulating micro-synchrophasors on a certified high precision signal generator, the Omicron CMC256plus ™. A Class A IEC61000-4-30 ed 3 PQ instrument recorded the emulated micro-synchrophasors.

1.6.1.2 Laboratory Evaluation of the Micro-Synchrophasor

A laboratory test network was used to emulate a LV distribution network [24]. Calibrated laboratory equipment was used to measure the impedance of the emulated distribution line to a high degree of certainty. This cable was long enough to include measurable impedance values, which served as the benchmark.

The laboratory test emulations served as a second and complimentary verification of the instrumentation in use to record the micro-synchrophasor within the definition of [19].

1.6.2 Theoretical analysis, simulations and a reference case study

To determine the expected impacts an PV power plant integrated into a local distribution grid, the following conceptual studies were performed:

a) Theoretical impact analysis.

b) Simulation study.

c) Evaluation of a published case study.

1.6.2.1 Theoretical impact analysis

A theoretical study was conducted to evaluate the effects of a large scale DG source connected to a network bus. This was done with the goal to determine the conceptual effects on a bus comprising two voltage sources.

The impact on steady-state and voltage stability was assessed through nominal power equations such that the of the PV generation source can be comprehended. A theoretical study was conducted to evaluate the effects of a large-scale DG source connected to a network bus. The associated impacts pertaining to steady-state and voltage stability were assessed.

1.6.2.2 Simulation study

A simulation of a distribution network comprising a large-scale PV power plant was conducted to diagnose the stability interaction between the Point of Connection (PoC) of the PV plant and the Point of Common Coupling (PCC). The simulation study was conducted by constructing a power system with an integrated PV power plant using Simulink®.

The IEEE introduced many simulation guidelines and topology layouts such as the IEEE 9 and IEEE 14 bus networks regarding power system simulations [25]. These IEEE simulation guidelines have been followed to imitate similar conditions of the distribution network under study.

1.6.2.3 Evaluation of a published case study

The results and findings of a published case study on PV power plant integration into the distribution networks was evaluated to support the results deducted from the simulations.

1.6.3 Field performance of the micro-synchrophasor

Micro-synchrophasor data was obtained in a 132 kV distribution network with relatively low fault level. Recordings were made at the PoC of a 75 MW PV power plant and at the PCC 100 km away over a representative period of network operation.

1.7 Conclusion

This Chapter introduced the opportunity for the micro-synchrophasor to monitor the performance of distribution networks with integrated renewable energy sources. South Africa has favourable year-round irradiance conditions, leading to PV power production identified as a viable option to substitute the shortfall in generation by traditional coal-fired power stations as currently experienced.

These renewable energy sources are predominantly found in distribution level networks, causing more responsibility to be taken over by distribution network infrastructures. Such developments induced the need for advanced supervision over distribution systems.

Synchrophasor applications in transmission systems are a proven asset for system operators to monitor network stability. Similar opportunities at distribution voltage levels have stated to emerge due to continuous advancements in synchrophasor recording capabilities.

Smaller phase angle values are expected between different locations in distribution networks. Therefore higher recording resolutions in synchrophasor measurements are required. The concept of micro-synchrophasor measurements capable of detecting small angular variations was introduced in this chapter.

The outcomes of the research conducted in this dissertation aims to evaluate the viability of micro-synchrophasor recordings to monitor PV power plant integration. It is expected that visualisation of micro-synchrophasor recordings can provide a better baseline understanding in the impact of RPPs on distribution network stability.

Chapter 2:
Literature Study

2.1 Introduction

Since inception of distributed energy sources, distribution network structures have undergone significant development. The possibility of synchrophasor deployment at distribution voltage levels is an important progression that can enable the stability concerns on network operation comprising DG to be fully addressable. In this chapter the relevant literature concerning micro-synchrophasor monitoring applications at commercial PV plants in distribution networks are reviewed.

The definition of what is regarded as a micro-synchrophasor is presented and then used to derive the measurement criteria for synchrophasor recordings to comply as micro-synchrophasors.

In this chapter the scientific literature of the aspects relevant provide an extensive understanding of applying micro-synchrophasors to monitor sources of renewable energy in sub-transmission levels are reviewed.

2.2 Distribution line modelling

2.2.1 The distribution line equivalent circuit

An equivalent circuit for a distribution line can be derived based on the distributed nature of the line parameters. Consider an equivalent transmission line circuit with length Δx:

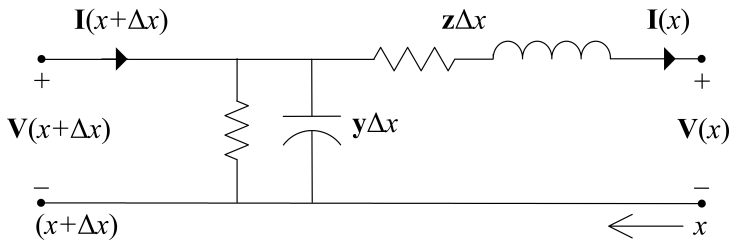

Figure 2-1: Equivalent line model of length Δx [13]

The shunt and series impedance of the line are:

$$\begin{aligned} \mathbf{z} &= R + j\omega L \\ \boldsymbol{y} &= G + j\omega C \end{aligned} \tag{2.1}$$

The shunt conductance, G, exist between conductors or between conductors and the ground. It constitutes the losses in leakage current across the insulators of overhead lines and through the insulation of cables.

Since the leakage across insulators is substantially small, it is ordinarily neglected. Therefore the shunt conductance parameter is not considered. Using Kirchhoff's Voltage and Current Laws (KVL and KCL) to obtain voltage current equations [13].

.

$$\boldsymbol{V}(x+\Delta x) = \boldsymbol{V}(x) + (\mathbf{z}\Delta x)\,\boldsymbol{I}(x) \tag{2.2}$$

$$\boldsymbol{I}(x+\Delta x) = \boldsymbol{I}(x) + (\boldsymbol{y}\Delta x)\,\boldsymbol{V}(x+\Delta x) \tag{2.3}$$

If the per unit length Δx is infinitesimal short, then (2.2) and (2.3) can be rewritten as

$$\mathbf{z}\boldsymbol{I}(x) = \lim_{x\to 0}\left(\frac{\boldsymbol{V}(x+\Delta x) - \boldsymbol{V}(x)}{\Delta x}\right) = \frac{d\boldsymbol{V}(x)}{dx} \tag{2.4}$$

and

$$\boldsymbol{y}\boldsymbol{V}(x) = \lim_{x\to 0}\left(\frac{\boldsymbol{I}(x+\Delta x) - \boldsymbol{I}(x)}{\Delta x}\right) = \frac{d\boldsymbol{I}(x)}{dx} \tag{2.5}$$

***I**(x)* can be eliminated by differentiating (2.4) and substituting into (2.5),

$$\frac{d^2\boldsymbol{V}(x)}{dx^2} = \mathbf{z}\boldsymbol{y}\boldsymbol{V}(x) \tag{2.6}$$

Integrating (2.6) by means of first principles, a solution for *V(x)* is obtained:

$$\boldsymbol{V}(x) = \boldsymbol{A}_1 e^{\gamma x} + \boldsymbol{A}_2 e^{-\gamma x} \tag{2.7}$$

with:

$\boldsymbol{A}_1$, $\boldsymbol{A}_2$ Integration constants
γ Propagation constant

***I**(x)* is solved by means of substituting (2.7) into (2.4) and applying integration using first principles:

$$\boldsymbol{I}(x) = \frac{\boldsymbol{A}_1 e^{\gamma x} - \boldsymbol{A}_2 e^{-\gamma x}}{Z_C} \tag{2.8}$$

with,

$Z_c = \sqrt{\frac{z}{y}}$ Characteristic impedance

The receiving end of the line is defined at length x=0, has receiving end voltage and current magnitudes defined from (2.7) and (2.8):

$$\boldsymbol{V}_R = \boldsymbol{V}(0) = \boldsymbol{A}_1 + \boldsymbol{A}_2 \tag{2.9}$$

$$\boldsymbol{I}_R = \boldsymbol{I}(0) = \frac{\boldsymbol{A}_1 - \boldsymbol{A}_2}{Z_C} \tag{2.10}$$

Solving $\boldsymbol{A}_1$ and $\boldsymbol{A}_2$:

$$\boldsymbol{A}_1 = \frac{\boldsymbol{V}_R + Z_C \boldsymbol{I}_R}{2} \tag{2.11}$$

$$\boldsymbol{A}_2 = \frac{\boldsymbol{V}_R - Z_C \boldsymbol{I}_R}{2} \tag{2.12}$$

$\boldsymbol{A}_1$ and $\boldsymbol{A}_2$ are substituted into (2.7) and (2.8) where they are solved in order to obtain differential transmission line equations for voltage and current values at a given length x.

$$\boldsymbol{V}(x) = \cosh(\gamma x)\boldsymbol{V}_R + Z_C \sinh(\gamma x)\boldsymbol{I}_R \tag{2.13}$$

$$\boldsymbol{I}(x) = \frac{1}{Z_C}\sinh(\gamma x)\boldsymbol{V}_R + Z_C \cosh(\gamma x)\boldsymbol{I}_R \tag{2.14}$$

The equivalent line *ABCD* parameters are subsequently denoted in (2.13) and (2.14) with the following characteristics:

$$\begin{aligned} A(x) &= D(x) = \cosh(\gamma x) \\ B(x) &= Z_C \sinh(\gamma x) \\ C(x) &= \tfrac{1}{Z_C}\sinh(\gamma x) \end{aligned} \tag{2.15}$$

Exact parameters can be obtained by considering the two-port network model of the line, presented in the following section below.

2.2.2 Two-port network parameters for distribution lines

The appropriate *ABCD* parameters from the equivalent line parameters are acquired through two-port network modelling [13]:

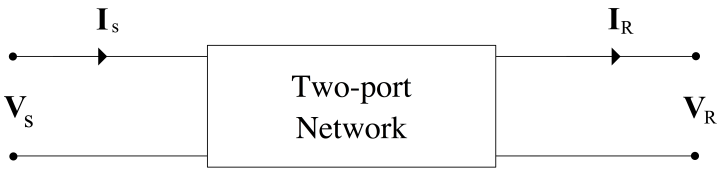

Figure 2-2: Two-port model [13]

By considering a finite length of the line, the exact model for sending end voltage and current are obtained. Let the length of the line be regarded as x=ℓ, such that $\mathbf{V}(\ell)$=$\mathbf{V}_s$,

$\mathbf{I}(\ell)$=$\mathbf{I}_s$. Which results in:

$$\begin{aligned} \boldsymbol{V}_S &= AV_R + BI_R \\ \boldsymbol{I}_S &= CV_R + DI_R \end{aligned} \tag{2.16}$$

The parameters are assigned to each term that represents respective line characteristics. These equations can also be expressed in matrix format,

$$\begin{bmatrix} V_S \\ I_S \end{bmatrix} = \begin{bmatrix} A & B \\ C & D \end{bmatrix} \begin{bmatrix} V_R \\ I_R \end{bmatrix} \tag{2.17}$$

The *ABCD* parameters given in (2.15) are exact parameters and obey the condition [13],

$$AD - BC = 1 \tag{2.18}$$

Distribution lines predominantly represents short distance lines (< 100 km). The capacitance between the line and ground is very small across short distances, causing the losses in the form of a leading charge current to be low. Along with the low conductance losses, distribution lines comprise negligible shunt admittance. [13].

The two-port distribution line model with neglected shunt admittance is presented in Figure 2-3.

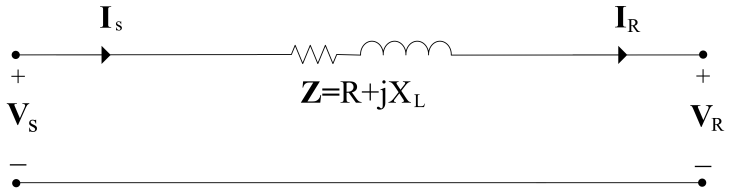

Figure 2-3: Two-port distribution line model with neglected shunt admittance [13]

The short distance *ABCD* parameters are obtained by applying Kirchhoff's Voltage Law (KVL) and Kirchhoff's Current Law (KCL) to the two-port model. Since the shunt admittance, *Y*, is neglected the sending end current is equal to the current at the receiving end. Sending end voltage equals the sum of the receiving end voltage and the voltage drop over the line, given in 2.19.

$$\begin{aligned} V_S &= V_R + ZI_R \\ I_S &= (0)V_R + I_R \end{aligned} \tag{2.19}$$

Direct equalisation of (2.19) with the two-port model provide the *ABCD* parameters with the following line characteristics:

A: 1 per unit (*pu*)
B: Series line impedance (*Z*)
C: Shunt admittance (*Y*)
D: 1 per unit (*pu*)

These characteristics apply to linear, passive and bi-lateral two-port network calculations, with the shunt admittance neglected, the parameters are specified in accordance to short transmission lines [13].

$$A = D = 1$$
$$B = Z = R + jX_L$$
$$C = Y = 0$$

Subsequently, (2.19) can be displayed in matrix format [13]:

$$\begin{bmatrix} V_S \\ I_S \end{bmatrix} = \begin{bmatrix} 1 & (R + jX_L) \\ 0 & 1 \end{bmatrix} \begin{bmatrix} V_R \\ I_R \end{bmatrix} \tag{2.20}$$

By taking these two-port network parameters for distribution lines into account, the power transfer across such short distance overhead lines are derived in the following section.

2.2.3 Power transfer across short distance lines

The equivalent two-bus short-distance line in Figure 2-3 is considered with a voltage source,$\mathbf{V}_S$. Power is propagated to the P + jQ load at the receiving end of the line, presented in Figure 2-4.

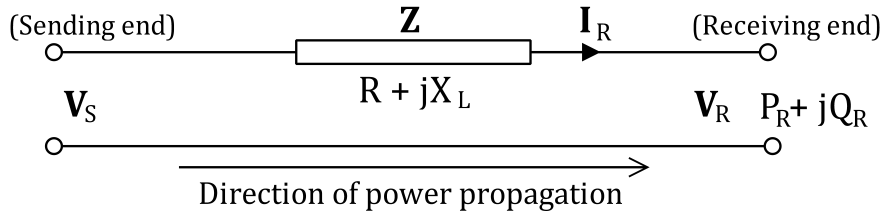

Figure 2-4: Equivalent model and PV propagation direction of the interconnecting overhead line

The transferable apparent power over the distribution line, $\boldsymbol{S}_R$, is expressed in (2.21):

$$\boldsymbol{S}_R = P_R + \mathrm{j}Q_R \tag{2.21}$$

$\boldsymbol{S}_R$ can also be expressed in terms of voltage and current:

$$\boldsymbol{S}_R = \boldsymbol{V}_R \times \boldsymbol{I}_R^* \tag{2.22}$$

Where $I_R{}^*$ represents the complex conjugate of the line current and is given as:

$$\boldsymbol{I_R}^* = \left(\frac{\boldsymbol{V}_S - \boldsymbol{V}_R}{\boldsymbol{Z}} \right)^* \tag{2.23}$$

It was stated earlier that losses of an overhead distribution line are relatively low and can

be neglected:

$$\boldsymbol{I_R}^* = \left(\frac{\boldsymbol{V_S}^* - \boldsymbol{V_R}^*}{\mathrm{j}X^*}\right) \tag{2.24}$$

The expanded conjugate expression of the line current in (2.24) is substituted in (2.22), which gives:

$$\begin{aligned} \boldsymbol{S_R} &= \boldsymbol{V_R}\left(\frac{\boldsymbol{V_S}\, e^{-(\mathrm{j}\delta)} - \boldsymbol{V_R}}{-(\mathrm{j}X)}\right) \\ \therefore\ \boldsymbol{S_R} &= \left(\frac{\boldsymbol{V_R}\boldsymbol{V_S}\, e^{-(\mathrm{j}\delta)} - \boldsymbol{V_R}^2}{-\mathrm{j}X}\right) \end{aligned} \tag{2.25}$$

Recalling Euler's Identity:

$$e^{\mathrm{j}\delta} = cos(\delta) + \mathrm{j}sin(\delta) \tag{2.26}$$

This identity is applied to the transmitted apparent power in (2.25) that results in:

$$\boldsymbol{S_R} = \frac{V_S V_R\left(\cos(\delta) - \mathrm{j}\sin(\delta)\right) - {V_R}^2}{-\mathrm{j}X} \tag{2.27}$$

The expression for transferred power over a distribution line is given by setting (2.21) and (2.26) equal to each other.

$$P_R + \mathrm{j}Q_R = \mathrm{j}\frac{V_S V_R \cos(\delta)}{X} + \frac{V_S V_R \sin(\delta)}{X} - \mathrm{j}\frac{{V_R}^2}{X} \tag{2.28}$$

From (2.28) the real and reactive power transmitted are obtained:

$$P_R = \frac{V_S V_R}{X}\sin(\delta) \tag{2.29}$$

$$Q_R = -\frac{{V_R}^2}{X} + \frac{V_S V_R}{X}\cos(\delta) \tag{2.30}$$

These power transfer equations are the basis from which system stability calculations using micro-synchrophasor recordings will be done. In the following section the fundamental principles of phasors are reviewed.

2.3 Fundamentals of a phasor

A phasor is a phase vector representation of a sinusoidal function. Current and voltage waveforms are functions of time, characterised by a given waveform amplitude and phase angle displacement [13]:

$$\boldsymbol{x}(t) = X_m \cos(\omega t + \phi) \tag{2.31}$$

with:

X_m	Amplitude
ω	Angular velocity

ϕ Phase angle

Applying Euler's identity, $e^{j\phi} = \cos(\phi) + j\sin(\phi)$ and the root-mean-square (RMS) value of the amplitude, $X = \frac{X_m}{\sqrt{2}}$, (2.31) can be written in three variations:

a) **Rectangular**

$$\boldsymbol{X} = X\cos(\phi) + \mathrm{j}X\sin(\phi) \tag{2.32}$$

b) **Exponential**

$$\boldsymbol{X} = Xe^{\mathrm{j}\phi} \tag{2.33}$$

c) **Polar**

$$\boldsymbol{X} = X\angle\phi \tag{2.34}$$

Calculations with phasors enable sinusoidal waveforms to be evaluated simplistically. Phasors are also easily converted from one mathematical notation to another, depending on the arithmetic preference. In power system calculations the polar form is usually applied; in signal processing the tendency is to use rectangular form and with calculus exponential phasors are preferred.

A visual representation of the phasor in (2.31) on the cartesian plane is represented in Figure 2-5.

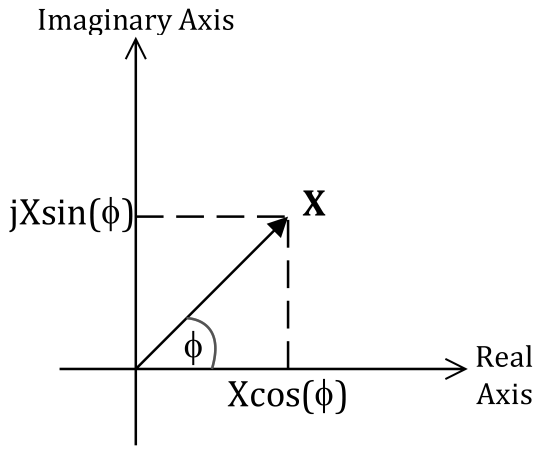

Figure 2-5: Phasor representation on the cartesian plane

Cartesian plane phasor representations are commonly implemented in the industry as a visual aid to assist with condition assessment such as illustrating the operating quadrant of synchronous machines on their excitation systems.

In synchrophasor analysis the voltage phasors between two locations are usually compared against each other to acquire the voltage phase angle difference. By obtaining the voltage phase angle difference between two locations will enable system operators and

engineers to assess the stability interaction between those two locations. The significance of the voltage phase angle is discussed in the section below.

2.4 The Significance of the voltage phase angle

Consider the expression for instantaneous voltage given as [13]:

$$v(t) = V_{\max} \cos(\omega t + \delta) \tag{2.35}$$

Where,

t Instantaneous time
ω Angular velocity
δ Voltage phase angle

The voltage phase angle represents the voltage waveform displacement (quantified in degrees) relevant to the voltage waveform of the reference bus (0°) in the given network. Phase angle displacement between two sinusoidal waveforms is referred to as voltage phase angle shifts and is always measured from a single point of reference. This phenomenon is illustrated in Figure 2-6.

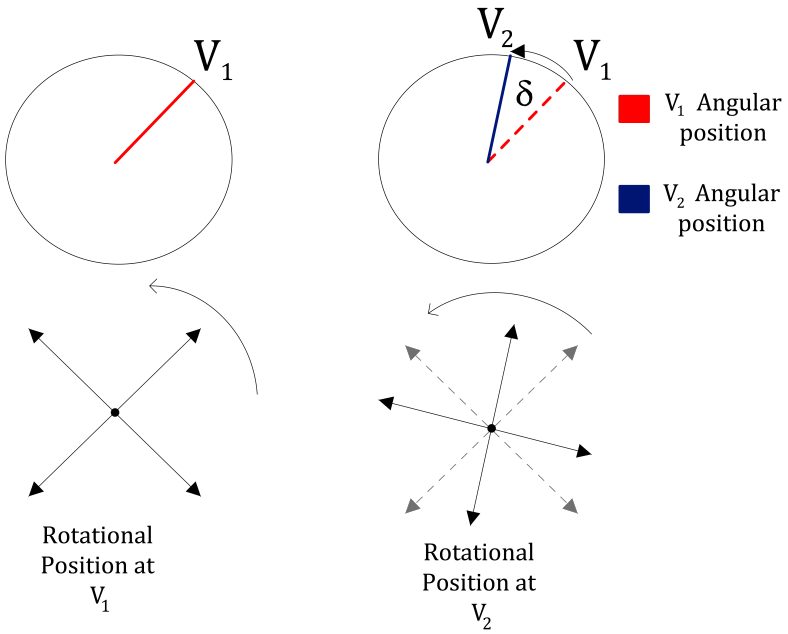

Figure 2-6: Phase shift between positions V_1 and V_2

As an example, Figure 2-6 presents the rotational positions of a generator (V_1) and a motor load (V_2) at the same instance of time. It can be seen that the rational position differs between the generator and motor, which a phase angle difference.

The phase shift difference between V_1 and V_2 is caused by reactance (capacitive or inductive) across the local network. Any voltage phase angle shift would subsequently influence to the power factor (pf), since the power angle is subject to the difference between the voltage and current phase angles [26].

2.4.1 Relation to the power factor

The pf in a network is an indication of how effective the network is utilised to deliver active (useful) power to a load. Reactive power cannot be completely avoided due to the intrinsic principle of operation of three-phase AC power systems, resulting in the loading of a network to be "apparently" higher than the active power delivered to the load. Power factor is usually expressed as a ratio of the total active power over apparent power [26]:

$$pf = \frac{P}{S} \tag{2.36}$$

The pf characteristics are based on the phase angle difference between the voltage and current waveforms, as presented in Figure 2-7.

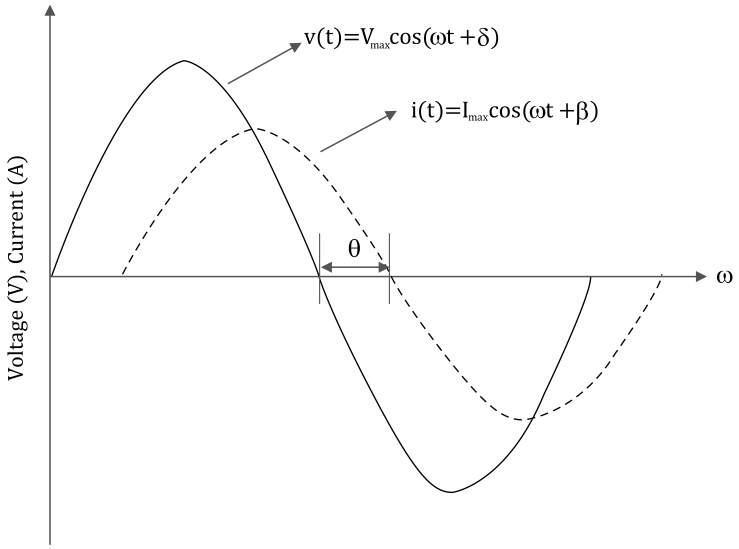

Figure 2-7: Power angle represents the voltage and current phase angle difference

The voltage and current sinusoidal waveforms have individual phase angles as is indicated by δ and β respectively. The power angle, θ, is the resultant phase angle displacement between the voltage and current waveforms, which is the principle characteristic that defines the pf. This quantity is determined by means of calculating the cosine function of the difference between voltage and current phase angles, shown in (2.37)

$$pf = \cos(\theta) = \cos(\delta - \beta) \tag{2.37}$$

The instantaneous apparent power, given in (2.38) can constitute a leading or lagging pf, depending on the type of impedance found in the network and is mostly dictated by the

type of load [13].

$$p(t) = v(t)i(t) = VI\cos(\omega t + \delta)\cos(\omega t + \beta) \tag{2.38}$$

2.4.2 Dependence on line construction

The voltage phase angle difference between two locations has a direct correlation to the impedance between the two points. The X/R ratio, which is evidently the ratio of reactance over resistance, is an important factor of the phase angle's magnitude. This is illustrated on the phasor diagram of a distribution line [13].

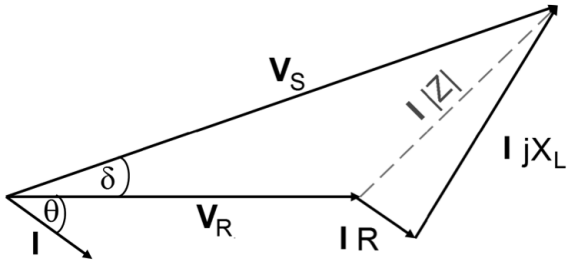

Figure 2-8: Phasor diagram of a short-distance transmission line

The receiving voltage phasor, $\mathbf{V}_R$, is considered as reference. The voltage phase angle, δ, can be altered by the X/R ratio. For instance, a transmission line with a low X/R ratio would induce a small voltage phase angle. X/R ratios of a line is a function of the line construction, i.e. the area of the conductors and its line spacing. Therefore a transmission line with a lower X/R ratio would induce a smaller voltage phase angle. Figure 2-9 shows this concept by displaying the dependency of the voltage phase angle on the X/R ratio magnitude.

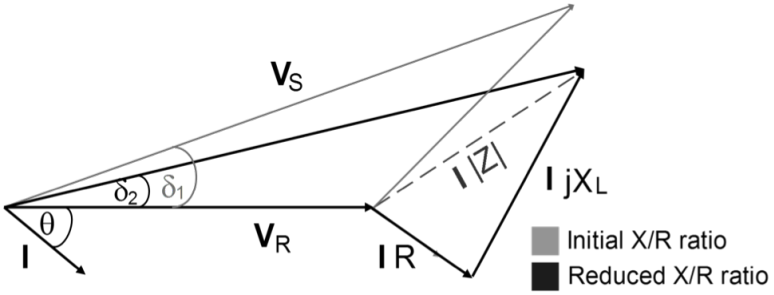

Figure 2-9: Phasor diagram of a short-distance transmission line with reduced X/R ratio

Due to a smaller X/R ratio the voltage phase angle has been effectively reduced ($\delta_2 < \delta_1$). It is therefore shown that the voltage phase angle across line is influenced by the X/R ratio of the line.

2.4.3 Voltage phase angle as stability indicator

Network stability concepts include: torque-angle stability, steady-state stability, transient stability, frequency stability and voltage stability. The phase angle between two voltage

phasors across a distribution line is a direct indicator of the transferred power over a line, $P = (V_S V_R / X) \times \sin(\delta)$.

The voltage phase angle can therefore be applied to determine the steady-state and voltage stability, as shown in Figure 2-10.

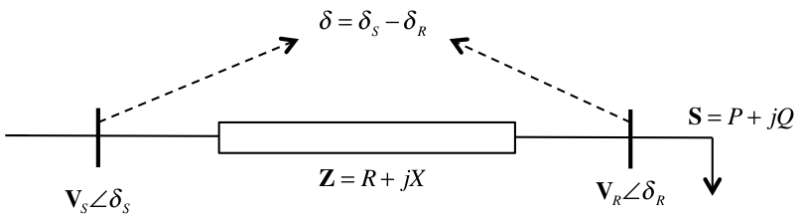

Figure 2-10: Voltage phase angle acquisition across a distribution line

The voltage phase angle between two points presents the shift in the voltage waveform between the sending- and receiving-ends of the line. The magnitude in this shift is subject to the amount of reactance between the two measuring locations. Evaluating the voltage phase angle difference between two measuring points can be used as a grid reliability indicator.

2.4.4 Steady-state stability

The voltage phase angle is used to determine the steady-state stability by assessment of the δ-P relation. Steady-state stability is visualised by means of tracking the operating point on a sinusoidal curve known as a power-transfer curve.

The phase angle is displayed in respect to the active power transferred to indicate the state in network operation. The power transferred over the line:

$$P_{transfer} = \frac{V_1 V_2}{X} \sin(\delta) \tag{2.39}$$

The transferred power, $P_{transfer}$, can be normalised as a per unit value in respect to the maximum transferable power, P_{max}:

$$P_{transfer} = p_{transfer,pu} \times P_{\max} \tag{2.40}$$

P_{max} is at 1.0 per unit. The normalised power-transfer curve is shown in Figure 2-11.

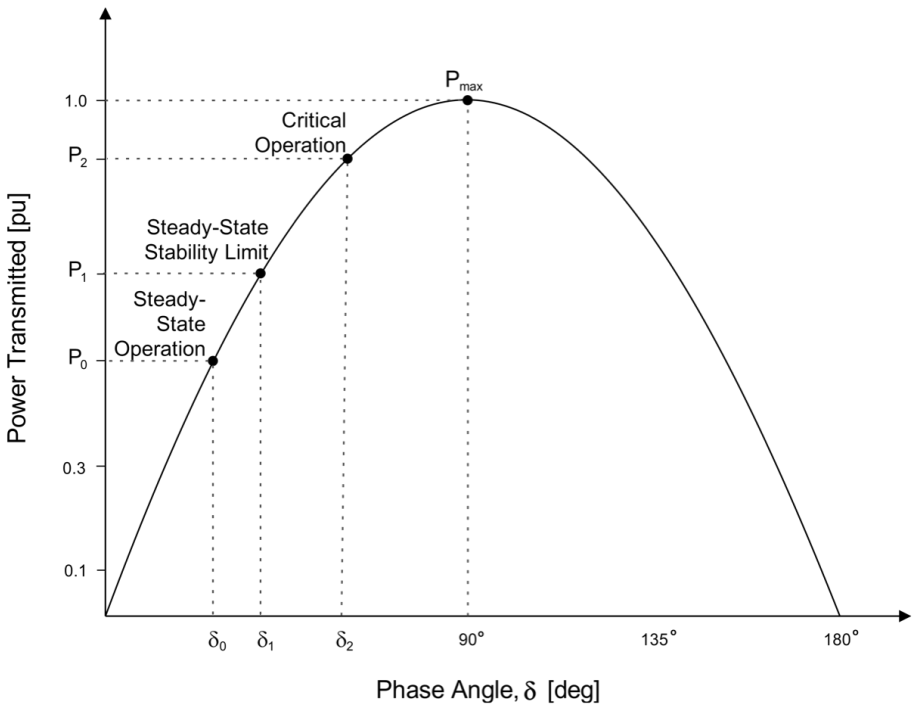

Figure 2-11: A power-transfer curve to evaluate steady-state stability [9]

The state of stability is indicated by the location of the phase angle. Given a steady-state operation, P_0, a sudden increase in the phase angle could cause operation to exceed the steady-state stability limit P_1. This can induce unstable operation since possible power swings and transient conditions may occur [9].

Visual tracking of the operating point on the power-transfer curve can enable system operators to monitor the state of stability and anticipate possible discrepancies.

2.4.4.1 Operation on a power-transfer curve

The power-transfer curve is a widely used platform to monitor and diagnose transient and multi-machine stability by using techniques such as the equal-area criterion [13].

When only considering the power-angle relation of the power-transfer curve, the steady-state stability can be affected in three different manners:

a) Impedance change between the two points.

b) An addition/reduction in active power capacity.

c) An increase/decrease in active power loading.

The point of operation is presented on the power-transfer curve by the δ-P relation, while the magnitude of the curve is determined by the maximum transferable power, P_{max}.

An increase/decrease in active power loading would change the position of the operating point, while an addition/reduction in power capacity will change the magnitude of the curve. Both these contingencies can cause the network to operate closer to steady-state instability.

P_{max} represents the theoretical steady-state stability limit as network operation will collapse beyond this point. In reality however, unstable conditions can occur at a much smaller phase angle. For example δ=30° would constitute a difference in the instantaneous voltage across the line of:

$$\begin{aligned} v_{sag}(t) &= v_1(t) - v_2(t) \\ v_{sag}(t) &= 1\cos(\omega t + 0°) - 1\cos(\omega t - 30°) \\ v_{sag} &= 0.13\text{per unit} \end{aligned} \tag{2.41}$$

which can cause serious damage during switchgear operations such as circuit breakers or bus transfer schemes opening and closing. This concept is presented in Figure 2-12.

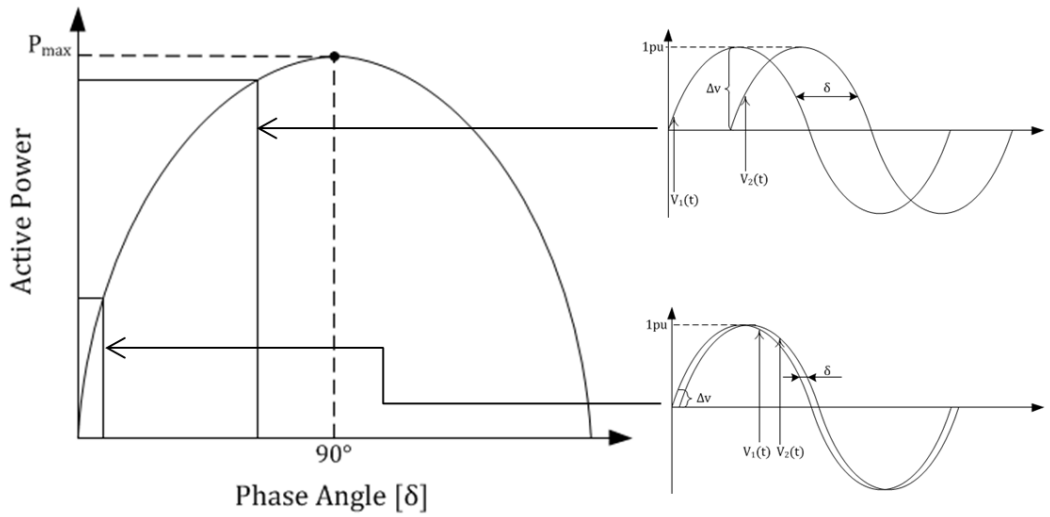

Figure 2-12: Potential difference increase with the phase angle

2.4.4.2 Monitoring steady-state stability on power-transfer curves

The steady-state operating point on a power-transfer curve can be visually tracked by two different means. It can be displayed as a single point that shifts across the curve as network operation suddenly changes or as a number of operating points reported over time.

The first option can be used as a near real-time tracking platform of steady-state stability, whilst the second option present a historical (day, week, year) perspective of operating conditions. These two tracking options are presented in Figure 2-13.

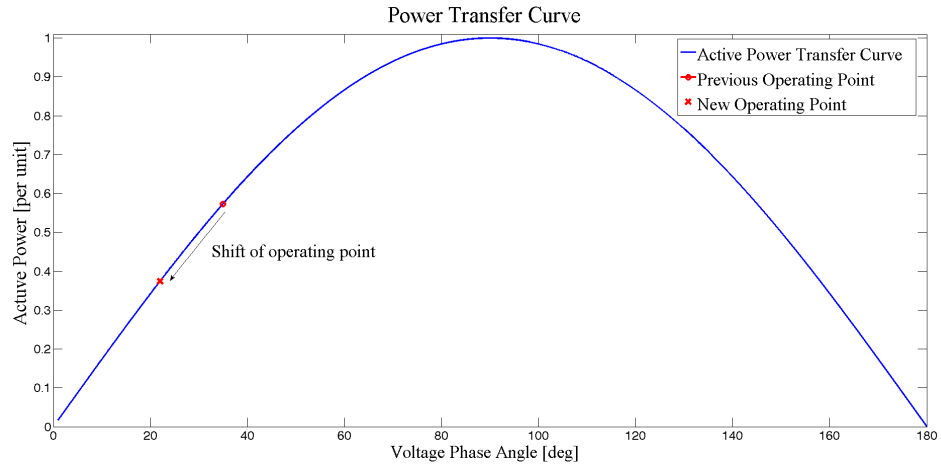

(a) Single point tracking that shifts as operation suddenly changes

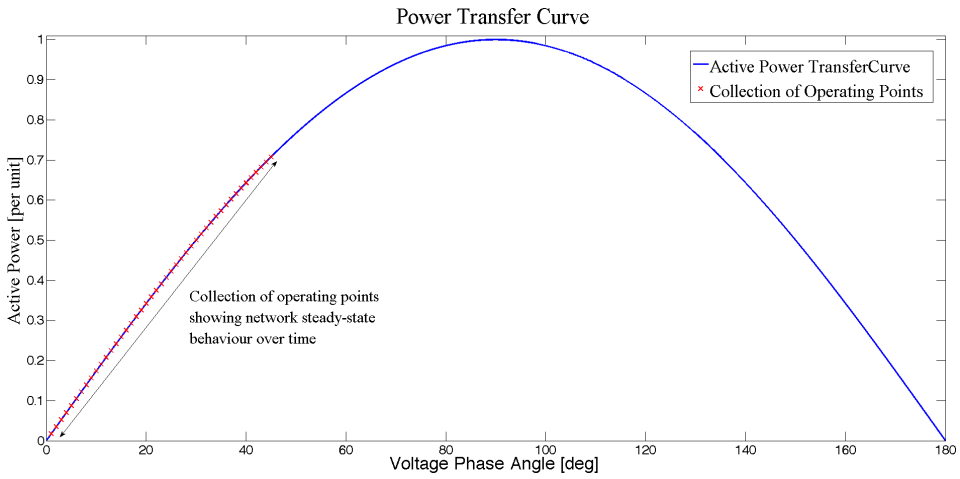

(b) Collection of operating points added over time

Figure 2-13: Different methods to visually track steady-state stability

A single point of operation display, shown in Figure 2-13(a), enables real-time assessment on the network steady-state by analysing the trend on which the operating point is shifted. This method can prove beneficial for instability mitigation and early detection applications [27].

The collective display of operation points over time, shown in Figure 2-13a, is an attractive application for post-mortem analysis. The system operator can assess how stability was affected and detect any outlier values over a specified period of time.

This is especially attractive for RPP integration behaviour diagnostics, where the impact on network steady-state can be evaluated over the plant's daily production period. Using the same variables along with the power angle, θ, an integrated RPP's impact on the voltage stability of the local network can also be evaluated.

2.4.5 Voltage stability

Voltage stability analysis is one of the most accepted means to evaluate network instability [9]. Voltage stability analysis on a P-V curve is a well-known concept. It visualises the state of voltage stability by depicting the point of operation to indicate the margin in active power before instability.

The active power stability margin can be quantified as the remaining load that a system can endure before the critical voltage level, located on the nose of the curve, is reached. The critical point, p_{nose}, which represents the maximum active power loading is calculated as [28]:

$$p_{nose} = \frac{1}{2}\left(\sqrt{1+\mathrm{LF}^2} - \mathrm{LF}\right) \tag{2.42}$$

where LF represents the load factor and is calculated as the tangent of the power angle, θ, equal to the ratio between the normalised reactive and active power loading:

$$\begin{aligned} \mathrm{LF} &= \tan(\theta) = \tan(\delta - \beta) \\ \mathrm{LF} &= \tfrac{q_{norm}}{p_{norm}} \end{aligned} \tag{2.43}$$

The variables p_{norm} and q_{norm} in (2.43) represents the active and reactive load consumption over a line, which are normalised in respect to the maximum transferable active power, P_{max} [28]:

$$\begin{aligned} p_{norm} &= \frac{P_{load}}{P_{\max}} = \frac{P_{load}}{\left(\frac{V_s V_R}{X}\right)} \\ q_{norm} &= \frac{Q_{load}}{P_{\max}} = \frac{Q_{load}}{\left(\frac{V_s V_R}{X}\right)} \end{aligned} \tag{2.44}$$

The expression for normalised values on the P-V curve is [28]:

$$\mathrm{v} = \sqrt{\frac{1}{2} - (p_{nose} \times \mathrm{LF}) \pm \sqrt{\frac{1}{4} - (p_{nose} \times \mathrm{LF}) - p_{nose}^2}} \tag{2.45}$$

The values within the square-root must be positive to have v as a real value [28]:

$$\frac{1}{2} - (p_{nose} \times \mathrm{LF}) - \sqrt{\frac{1}{4} - (p_{nose} \times \mathrm{LF}) - p_{nose}^2} \geq 0 \tag{2.46}$$

An example of the P-V curve is illustrated in Figure 2-14 below.

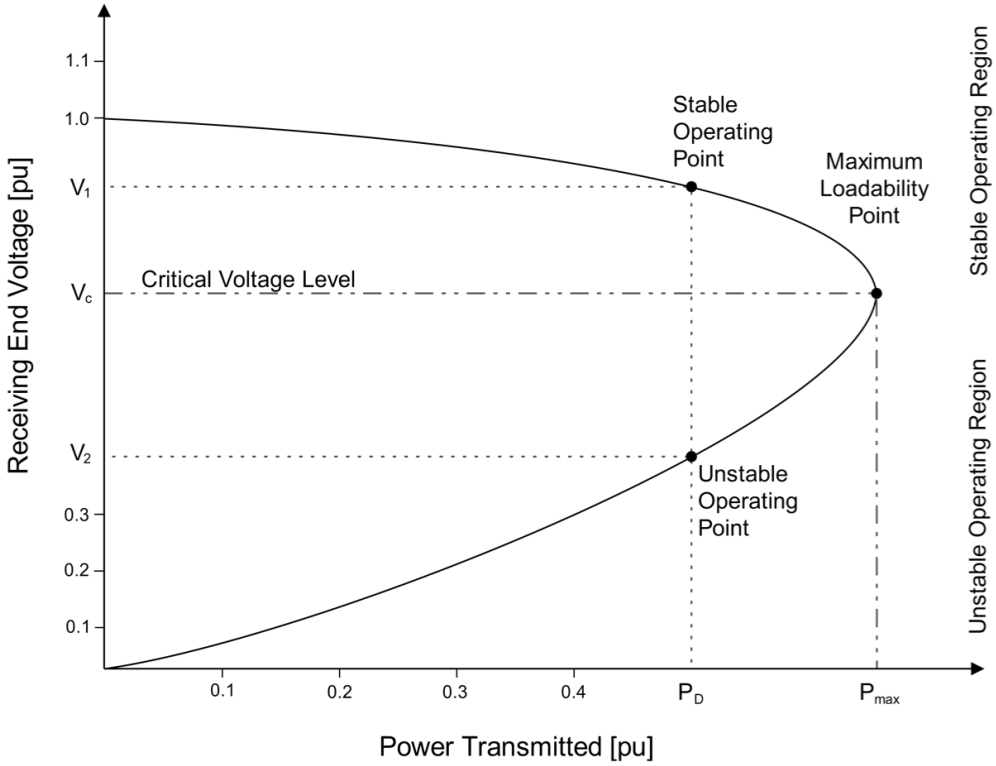

Figure 2-14: A typical P-V curve [9]

Voltage level relates to the active power loading. The VSM can be quantified on a P-V curve by referring to the active power stability margin. For a given operating point, such as the stable operating point on Figure 2-14, the active power stability margin is the remainder of active power loading before the operating point has reached maximum loadability for a given power factor [21].

The maximum loadability (critical) point on the P-V is approached during a network disturbance such as an increase in loading, insufficient reactive power transfer capabilities or limited supply capacity [28].

2.4.5.1 Characteristic behaviour of a P-V curve

On a P-V curve the point of operation can be visualised by the position of operation that relates the active power transferred to the voltage condition.

Voltage stability is quantified by calculating the position of active power consumption as a margin from the critical point of instability, located on the nose of the curve. For any given state of operation, both stable and unstable conditions exist. The upper halve of the curve in Figure 2-14 represents the stable region of operation, while the unstable region is portrayed by the bottom halve of the curve.

These two regions are separated by the critical voltage level where the nose of the P-V curve is located. The stable halve of the P-V curve is characterised by a negative relation between voltage and power. This indicates that as load consumption increase the voltage magnitude will decrease:

$$\text{Stable curve} = -\frac{dV}{dP} \tag{2.47}$$

The characteristic of the unstable half of the P-V curve has a positive relation between voltage and power, indicating that an increase in power consumption causes an increase in voltage:

$$\text{Unstable curve} = \frac{dV}{dP} \tag{2.48}$$

When a voltage disruption causes the voltage magnitude to decrease, the stable operating point is shifted down towards the nose of the curve, while the unstable operating point will be shifted down towards zero voltage.

A decrease in voltage will cause stable operation to momentarily operate at a higher active power consumption. This will be opposed by a decrease in current magnitude.

The voltage will subsequently increase in order to compensate for the decreased current, causing operation to stabilise and return back to its original position. The operating point may take some time to settle at its original location, depending on the "stiffness" of the network.

In the unstable region, a decrease in voltage magnitude on the unstable operating point would induce a downward shift on the P-V curve towards a lower active power consumption point. The current magnitude will increase to oppose the decreased active power.

This will result in voltage magnitude attempting to compensate for the increase in current by decreasing in turn. The operating point will subsequently continue to shift further away from its original position until zero voltage is reached.

The aim is to keep the operating point in the stable area to not fall over the nose into the unstable region.

2.4.5.2 P-V curves at different power factors

The critical operating point on P-V curves are subject to the respected power factor value. As the power factor change the P-V curve magnitude will increase or decrease accordingly. A set of characteristic P-V curves, each at a different power factor, are presented in Figure 2-15.

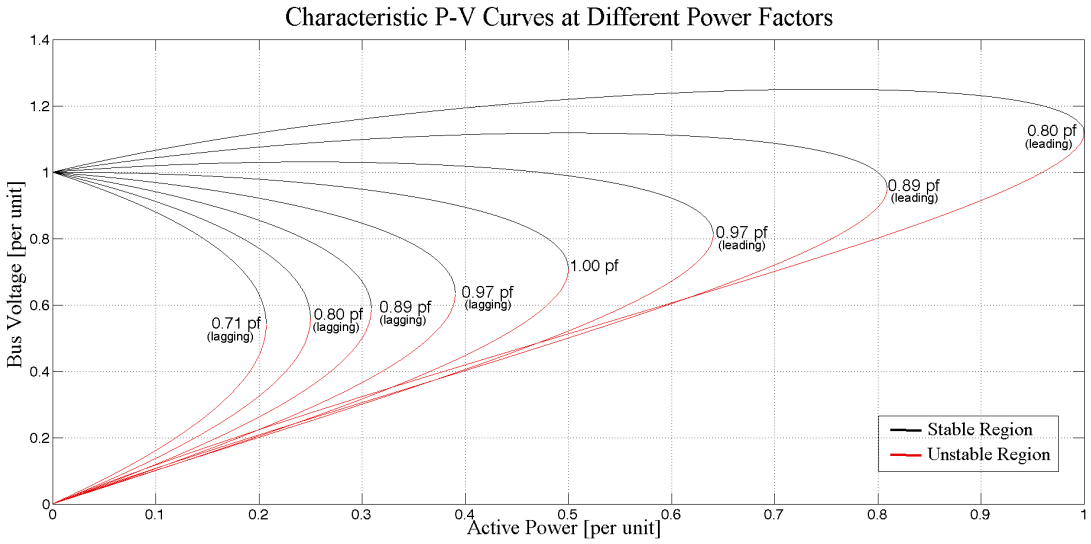

Figure 2-15: Characteristic P-V curves at different power factors

The magnitudes of the P-V curves are different for each specified power factor. Comparing the curves between the lagging and leading power factor values it can be seen that the curves comprising lagging power factors have smaller magnitudes than their leading power factor counterparts.

As the power factor moves from lagging to leading the critical voltage and power values of the P-V curves become higher. The stability margin is therefore improved as the power factor converge from lagging to leading since it increases the system's active power loadability [29].

2.4.5.3 Operational changes on the voltage stability margin

The VSM can be affected by contingencies such as changes in power factor, network loading variations, supply fault level changes or a loss in generation.

These changes can be quantified by the shift of the operating point and a change in the position of the locus, as illustrated in Figure 2-16.

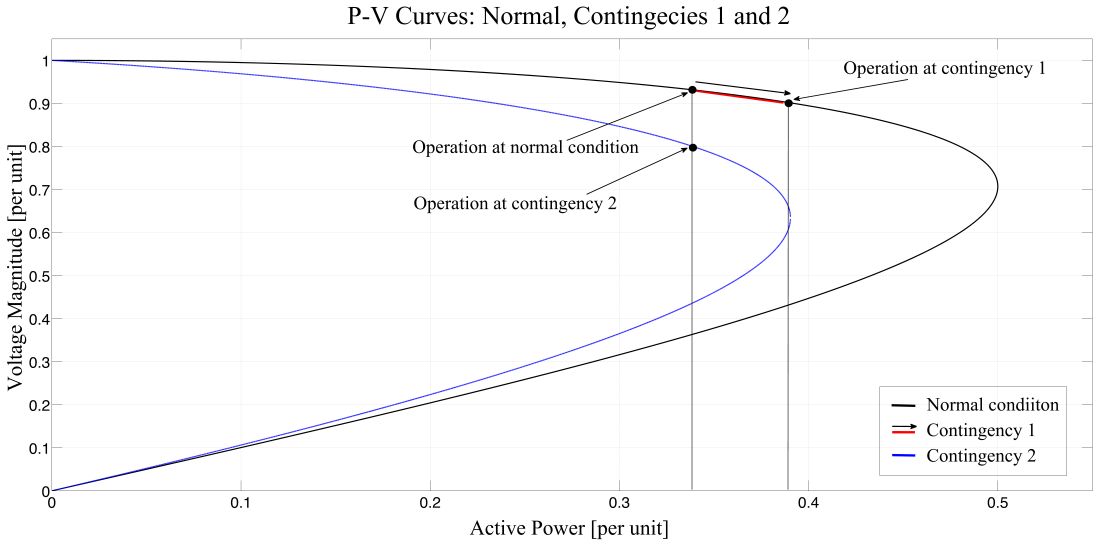

Figure 2-16: P-V curve analysis on the effect of different contingencies on the Voltage Stability Margin (VSM)

In the first contingency the P-V curve magnitude remains the same and the point of operation is shifted. This shift is representative of effects such as a voltage sag on a constant load or an increase in active power loading.

The P-V curve magnitude is decreased in the second condition and the operating point remains constant. This contingency can be caused by an altered power factor or an increase in the available active power.

Monitoring of voltage stability on the P-V curve would provide a support platform that can visualise these operations. This can provide the required information to implement mitigation techniques so that stability can be maintained.

To understand the basis on how micro-synchrophasors can be used to visually track these stability indicators, the fundamental principles surrounding synchrophasors are reviewed in the next section.

2.5 Synchrophasor principles

Synchronised phasor recordings, known as synchrophasors, are time-synchronised measurements that are conventionally recorded by PMUs at different locations in transmission systems. Implementing the same absolute time reference, such as UTC, enables the phasor measurements to be comparable. Time synchronisation can be achieved by GPS time-stamping. Synchrophasors are considered to be one of the most important power system measurement technologies developed in the last 50 years [11].

2.5.1 Synchrophasor principle of operation

Consider two sinusoidal waveforms where (2.49) presents the fundamental waveform and (2.50) presents a sinusoidal waveform with a phase angle offset from the fundamental waveform of ϕ:

$$x_0(t) = X_{m_0} cos\left(2\pi f_0 t\right) \tag{2.49}$$

$$x(t) = X_m cos(2\pi f t + \phi) \tag{2.50}$$

Representations of a synchrophasor measurement on these waveforms referenced to UTC is illustrated in Figure 2-17 [12]. Given a 1 pulse per second (PPS) sampling rate, the synchrophasor angle will be 0° during the cosine waveform maximum and -90° at the waveform's zero crossing during positive inclination. Should these samplings occur at the same sampling time, $t = 0$, the synchrophasor will show that the waveform angles are 90° out of phase, with the RMS value of the sinusoid denoting the synchrophasor magnitude.

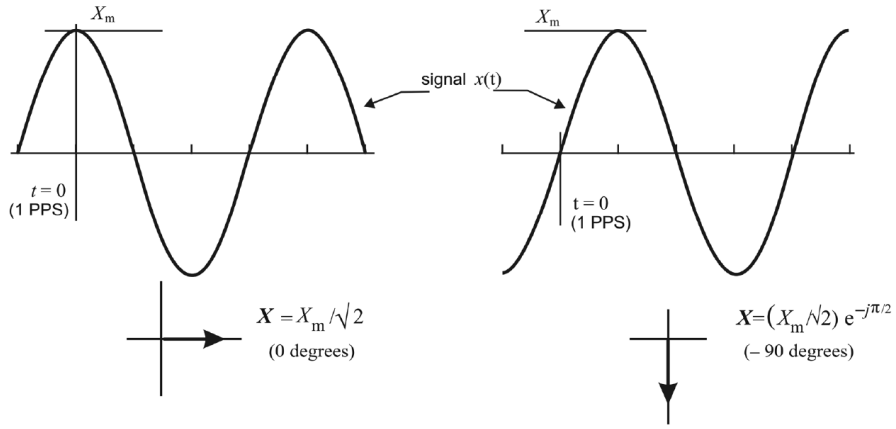

Figure 2-17: Synchrophasor representation convention [12]

The amplitude X_m and frequency f of a measured sinusoidal signal are time-dependant variables; an expression for the difference between the measured and nominal frequencies can be written as a function of time.

$$g = f - f_0 \tag{2.51}$$

The value of g will fluctuate perpetually with time since the instantaneous value of f is a time-dependant value, $f(t)$. Integrating $g(t)$ as a function of time will supply a finite value of the difference between the nominal frequency and actual system frequency:

$$\int (g)dt = \int (f - f_0)\, dt \tag{2.52}$$

Substituting (2.52) into (2.50) provides:

$$x(t) = X_m(t)\cos\left(2\pi\left(f_0 t + \int g(t)dt\right) + \phi\right) \tag{2.53}$$

From (2.53) The exponential synchrophasor form is given in Equation (2.54) as

$$\boldsymbol{X} = Xe^{j2\pi\int(g)dt+\phi} \tag{2.54}$$

The offset angle will increase uniformly at a rate of g, due to the deviation in nominal and system frequencies. This notion is visualised in Figure 2-18 [12]:

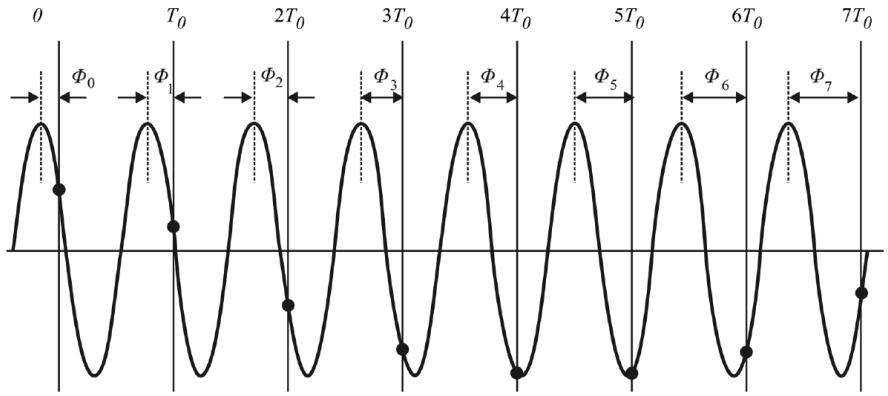

Figure 2-18: Phase angle offset incrementation [12]

Observations are made constant intervals $t = 0$, $T_0, ; 2T_0$, $3T_0, ; ...$, nT_0 where T_0 is the nominal system period. The corresponding phasor representations of the observation instances above are denoted [12]:

$$\begin{aligned}\mathbf{X}(T_0) &= \{\mathbf{X}_0, \mathbf{X}_1, \mathbf{X}_2, ..., \mathbf{X}_n\} \\ &\{n | n \in \mathbb{N}\}\end{aligned} \tag{2.55}$$

The synchrophasor offset phase angles will alternate at a rate of $2g(t)T_0$. Should the values ϕ_0, ϕ_1, ϕ_2, ..., ϕ_n be plotted over time, an increase would be observed. The angles will increase up on to 180° after which they would start at -180° again increasing to 180°. Synchrophasor convention dictates that phase angles are reported between -180°$\leq \phi \leq$180° rather than 0°$\leq \phi \leq$360°, which is demonstrated in Figure 2-19 [12].

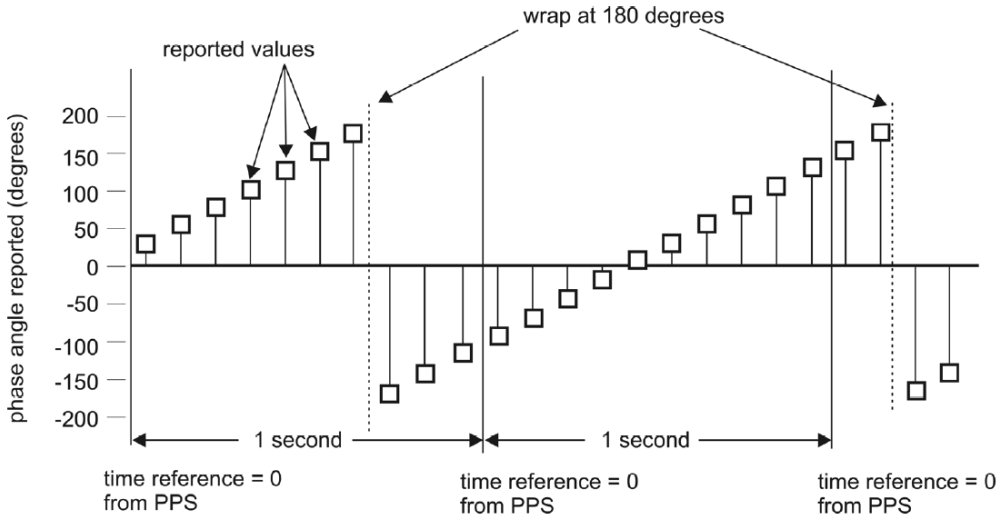

Figure 2-19: Synchrophasor angles due to off-nominal system frequency [12]

2.5.2 Synchrophasor measurement criteria

The IEEE Standard for Synchrophasor Measurements for Power Systems (IEEE Std. C37.118.1-2011) dictates that synchronised phasor measurements must adhere to various sampling criteria for the measurements to qualify as synchrophasors.

GPS time-stamping is the preferred method for time synchronisation in synchrophasors due to favourable accuracy that complies with synchrophasor timing error compliance levels and its tolerance against frequency errors.

Synchrophasors need to report measurements where criteria such as the Frequency Error (FE), Rate of Change of Frequency (ROCOF) and Total Vector Error (TVE) comply within the limits stipulated in the standard [12].

2.5.2.1 Frequency Error(FE)

The IEEE C37.118.2-2011 standard specifies that synchrophasors should report system frequencies for every synchronised phasor measurement. All synchrophasors need to comply with the frequency measurement error criteria of 0.05 Hz for a 50 Hz power system. The FE is estimated as [12]:

$$FE = |f_{true} - f_{measured}| \tag{2.56}$$

If the FE exceeds the compliance criteria, the phasor measurements can become asynchronous with other phasor recordings. This will induce an error between the measured and true phasor values causing inaccurate results to be reported.

2.5.2.2 Rate of Change of Frequency (ROCOF)

The ROCOF is an indicant that reports the fluctuation of system frequency in relation to nominal frequency, $f_0 = 50$ Hz, over a period of time. Frequency of a sinusoid is directly proportional to the change of phase angle as represented in Equation (2.57):

$$f(t) = \frac{1}{2\pi}\frac{d\phi(t)}{dt} \tag{2.57}$$

The ROCOF is defined by differentiating frequency over time:

$$ROCOF(t) = \frac{df(t)}{dt} \tag{2.58}$$

In the case where the cosine function is given as $\phi(t) = 2\pi(f_0 t + \gamma(t)/2\pi)$ the equation for frequency as a function of time is simplified to:

$$f(t) = f_0 + g(t) \tag{2.59}$$

ROCOF can then be calculated by means of differentiating the frequency deviation over time:

$$ROCOF(t) = \frac{dg(t)}{dt} \tag{2.60}$$

The frequency of a synchrophasor can either be reported as the instantaneous frequency *f(t)* or as the deviation from nominal frequency *g(t)*. During steady-steady network operation *g(t)* can be given as a finite frequency value *g* [12].

The ROCOF error (RFE) entails the error in detecting the change in frequency of a power system. The RFE is expressed in (2.61) below [12]:

$$RFE = |[\frac{df}{dt}]_{true} - [\frac{df}{dt}]_{measured}| \tag{2.61}$$

The IEEE Std. C37.118.1-2011 stipulates that synchrophasor recordings should comply within a RFE criteria of 0.01 Hz/s.

2.5.2.3 Total Vector Error (TVE)

TVE is the standard performance criterion for synchrophasor measurements. It is the magnitude of measurement error normalised to the theoretical correct phasor value. The purpose of the TVE is to provide an indication of the deviation from the theoretical calculated (correct) phasor value. TVE is calculated from the difference between theoretical and measured magnitude and phase angle values [11]:

$$TVE(n) = \sqrt{\frac{\left(\hat{X}_r(n) - X_r(n)\right)^2 + \left(\hat{X}_i(n) - X_i(n)\right)^2}{(X_r(n))^2 + (X_i(n))^2}} \tag{2.62}$$

with,

$\hat{X}_r(n)$	Real conjugate of the measured phasor
$\hat{X}_i(n)$	Imaginary conjugate of the measured phasor
$X_r(n)$	Real conjugate of the theoretical exact phasor
$X_i(n)$	Imaginary conjugate of the theoretical exact phasor
(n)	Instances of time

For synchrophasors to retain acceptable vector measurements the IEEE C37.118.1-2011 standard set a maximum TVE of 1% [12].

The error for the maximum compliance criteria listed by IEEE C37.118.1-2011 Standard for Synchrophasor Measurements for Power Systems [12] are summarised in Table 2-1:

Table 2-1: Synchrophasor phase angle errors caused by measurement errors

	Maximum Criteria	**Error in Phase Angle**
Time Error	$1\mu s$	0.018°
Frequency Error	0.005 Hz	0.036°
ROCOF Error	0.01 Hz/s	0.072°/s
Total Vector Error	1 %	0.57°

The criteria listed above are applicable to all synchronised phasor measurements. The synchrophasor requirements stipulated by the IEEE C37.118.1-2011 standards has been refined for micro-synchrophasors in [19] and is reviewed later in this chapter.

2.5.3 Uncertainty in measurement

When instruments measure voltages and currents the reliability behind the data reported needs to be assessed in order to evaluate the uncertainty of those measurements.

Uncertainty in measurement gives indication of the measurement error of a physical quantity [30]. This concept became relevant to metrology when a need to evaluate the correctness of measured results developed in the fields of science and engineering.

Without an indication of uncertainty, the measured results cannot be compared against other values, since the level of accuracy of the data is unknown. The uncertainty in measurement therefore signifies how well the measurement represents the true value of the particular quantity that has been measured.

Evaluation of the uncertainty in measurement is usually performed in a statistical manner where parameters such as standard deviation and average values to a series are used to provide a quantifiable value [31].

From a broad perspective, the uncertainty in measurement is evaluated to asses on applications such as [31]:

- Compliance with regulations and standard.
- Quality assurance of a product.
- Calibrations and performance evaluations.
- Research and applied development.

Any measurement consists of inaccuracies that result in an error in the measurement. From a metrological point of view, an error can be divided in two components:

a) ***Random error*** - Represents any error caused by an unpredictable or stochastic effect. These errors are usually present in an environment where the input parameters, such as voltage and current levels, cannot be controlled. Random errors can be reduced by increasing the number of measurements taken [31].

b) ***Systematic error*** - Represents the known errors that can either be avoided, such as rounding off decimal numbers, or compensated by means of applying a correction factor, for example the value of the internal impedance of a voltmeter can be taken into consideration (compensated) during the processing of results [31].

The following practical recommendations are given when evaluating the uncertainty in measurement [31]:

- The uncertainty in measurement should be determined using statistical analysis.
- The mathematical model used for calculations must report the uncertainty at the degree meaningful in evaluating the accuracy in measurement.
- To eliminate any outlier values, the evaluated data series must have as many observations as possible (quantitative data to provide qualitative results).
- It can be useful to conduct calculated predictions so that it can be determined whether a measurement system as expected.
- When evaluating for compliance to a measurement standard, the instrument is tested is usually tested against a well-calibrated device that is used as benchmark.
- If the results need to be converted to the relevant unit, rounding should only take place on the final result in order to maintain the closest answer.

2.5.4 Root causes of phasor measurement errors

2.5.4.1 Error in instrument transformers

Instrument transformers are designed to facilitate the measurements of high currents and voltages in a power system. Current transformers (CTs) and potential transformers (PTs), also commonly known as voltage transformers (VTs), are used to step-down the currents and voltages to measurable values. This is done by using specific transformer ratios to convert the values to new values that are suitable for the recording instruments.

Instrument transformers also provide safety to the engineer, as the primary and the secondary windings are galvanically isolated.

The use of CTs and PTs are shown in Figure 2-20.

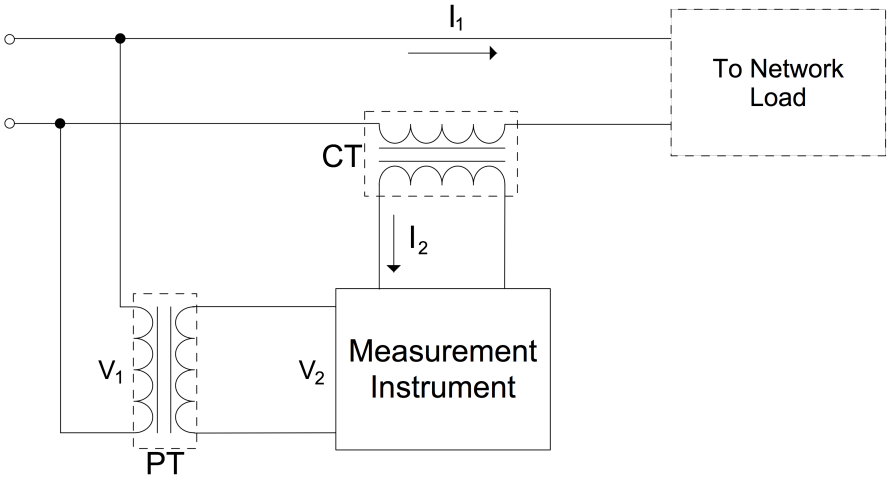

Figure 2-20: Application of instrument transformers for electric measurements

Similar to power transformers, instrument transformers are subject to losses. These losses such as winding losses and leakage flux would result in a non-ideal transformer ratio. Instrument transformers will therefore comprise a level of inaccuracy that causes an error in measurements.

Considering idealised PTs and CTs, the measured single-phase active power is quantified as:

$$P = V_1 I_1 \cos(\theta) = a_{PT} a_{CT} V_2 I_2 \cos(\theta) \tag{2.63}$$

where

V_1 and I_1 Primary side (HV) voltage and current.
V_2 and I_2 Secondary side voltage and current.
$a_{PT} = \frac{V_1}{V_2}$ Rated PT transformer ratio
$a_{CT} = \frac{I_1}{I_2}$ Rated CT transformer ratio.

Magnitude Displacement

The error in voltage and current magnitudes can be quantified through the following expressions [32].

$$\begin{aligned} \varepsilon_{PT} &= \frac{a_{PT}V_2 - V_1}{V_1} \\ \varepsilon_{CT} &= \frac{a_{CT}I_2 - I_1}{I_1} \end{aligned} \tag{2.64}$$

Where ε_{PT} represents the PT voltage magnitude error and ε_{CT} the CT current magnitude error. The effect of these error ratios are illustrated on a phasor diagram in Figure 2-21

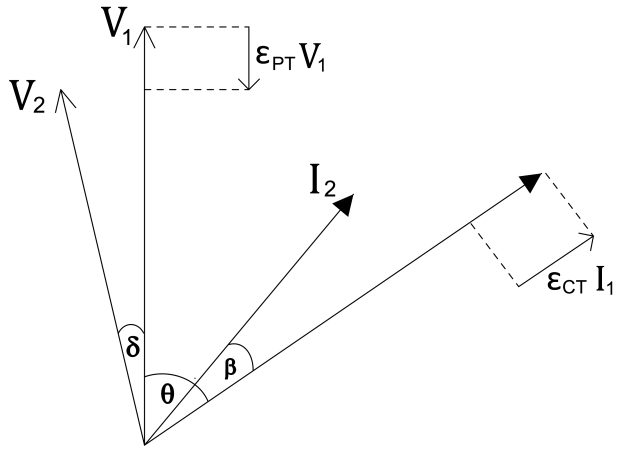

Figure 2-21: Phasor diagram with voltage and current magnitude errors [32]

Instrument transformers also comprise angular displacements due to the magnetisation of the core. These displacements will cause the secondary sides of the PTs and CTs to erroneously add an angular quantity to the measured signals. The PT angular displacement, δ'_{PT}, is defined as [32]:

$$\delta'_{PT} = \arg\left(\frac{V'_2}{V_1}\right) \tag{2.65}$$

While the CT angular displacement, β'_{CT}, is given by:

$$\beta'_{CT} = \frac{I_m \cos(\delta + \beta)}{I_1} \tag{2.66}$$

Taking these error ratios in account the ideally measured active power value in (2.63) is rewritten in its true form below:

$$P' = a_{PT}a_{CT}(1\varepsilon_{PT})(1\varepsilon_{CT})V_2 I_2 \cos\left(\theta - \left(\delta'_{PT} - \beta'_{CT}\right)\right) \tag{2.67}$$

The transformation error in instrument transformers increase when PTs and CTs measure values that exceed their rating plate magnitudes, since the PTs and CTs will be subjected to levels of magnetisations for which it was not designed for [32]. Different specifications in accuracy classes exist.

In general, PTs and CTs used in metering applications comprise a higher accuracy stan-

dard than those used in protection circuits where less stringent requirements on the exact value are needed for the goal to identify anomalies in the primary circuit.

The performance of a CT and PT lastly depends on the frequency of the signal to be measured. Accuracy specifications are done at the fundamental frequency. At harmonic frequencies, the error in amplitude can increase, but notably in phase angle. Synchrophasors pertaining to this study, are measured at 50 Hz.

2.5.4.2 Accuracy in phasor estimator algorithms

Different phasor estimation algorithms exist for the signal processing in PMUs [33]. Such estimators can be static or dynamic. Should phasor variations between observation intervals be small enough to be considered negligible the estimator is regarded as static.

Otherwise, if the phasor variations between observation intervals are considered significant enough to be taken into account the phasor estimation is dynamic [34].

Static Phasor Estimator

Most phasor measurement applications incorporate a static phasor estimation algorithm. The windowed observation based Discrete Time Fourier Transform (DTFT) is the conventional estimator algorithm for synchrophasors.

A static phasor estimator, such as the DTFT, neglects intrinsic amplitude and phase fluctuations, ε_a and ε_p, in the phasor waveform equation shown in (2.68) at a specific system frequency with a predefined reference sampling time [33].

$$p_r[n] = \frac{A}{\sqrt{2}}\left(1+\varepsilon_{a_r}[n]\right)e^{\mathrm{j}}\left(\varepsilon_{p_r}[n]+\phi_r\right) \tag{2.68}$$

where A is the waveform amplitude, ϕ is the initial phase angle and n the number of observational intervals. The DTFT of the r$^{\text{th}}$ observation interval is given as [34]:

$$\begin{aligned} S_{w_r} &= \frac{\sqrt{2}}{N}\left[\sum_{n=\frac{N-1}{2}}^{\frac{N-1}{2}} s_r[n]\,w[n]\,e^{-\mathrm{j}\frac{2\pi}{N}\lambda n}\right] \\ &= X_{w_r}(\lambda)+E_{h_r}(\lambda)+E_{n_r}(\lambda) \end{aligned} \tag{2.69}$$

with

$$X_{w_r}(\lambda) = p_{c_r}W(\lambda+v)+p^*_{c_r}W(\lambda+v) \tag{2.70}$$

and the DTFT of the specified window function w[n] given by:

$$W(\lambda) = \frac{1}{N}\left[\sum_{n=-\frac{N-1}{2}}^{\frac{N-1}{2}} w[n]\,e^{-\mathrm{j}\frac{2\pi}{N}\lambda n}\right] \tag{2.71}$$

where λ is the frequency variable for the considered observation integer N and v the fundamental frequency of N constituting a specified frequency deviation [35].

The static phasor estimator has been shown to comply with the accuracy requirements of the Standard IEEE C37.118.1-2011 [34] and is the conventional estimation algorithm for PMUs recording synchrophasors at transmission level. Such estimators have the added benefit not being susceptible to harmonics and system noise during recordings.

Modern distribution networks are subjected to much more variations and instabilities due to more complexity found in the network such as sources of renewable energy with dynamic output profiles. Synchrophasors in such a network will benefit from an estimator that includes inter-observation variations for improved measurement accuracy.

Dynamic Phasor Estimator

In observations where the waveform phasor rapidly varies during the observational intervals, it will be beneficial to take amplitude and phase fluctuations into account, making the phasor estimator dynamic in principle.

An auspicious dynamic phasor estimation algorithm used is the Interpolated Dynamic Discrete Fourier Transform (IpD^{2}FT) [34]. The IpD^{2}FT, defined from the static DTFT in (2.69) for the r^{th} observational interval is expressed as [35]:

$$S_{w_r}(\lambda) \cong X_{w_r}(\lambda) \cong \sum_{k=0}^{k} \left[p_{r,k} W_k(\lambda - v) + p_{r,k}^* W_k\left(W_k(\lambda - v) + p_{r,k}^* + v \right) \right] \tag{2.72}$$

where the phasor p_r and its conjugate p_r^* have the inter-observation fluctuations, ε_a and ε_p, taken into account, with $W_k(\lambda)$:

$$W(\lambda)_k = \left(\mathrm{j} \frac{N}{2\pi} \right)^k \left(\frac{d^k W(\lambda)}{d\lambda^k} \right) \tag{2.73}$$

Accuracy studies on various phasor estimators [33]–[35] have shown that both static and dynamic algorithms are satisfactory with compliance of the accuracy criteria in the IEEE C37.118.1-2011. Comparing the static DTFT estimator with its dynamic IpD^{2}FT counterpart a lot of similarities can be seen.

The predominant difference between these estimators is that the dynamic IpD^{2}FT algorithm accommodates waveform fluctuations, while the static estimator is less susceptible to harmonics and noise interferences.

Even if the dynamic estimator is arguably more suitable for a DG integrated power system due to associated variations, no estimator is the clear favourite in overall phasor processing accuracy [35].

2.5.4.3 Time synchronisation inaccuracy

The time uncertainty in GPS time-stamping contributes towards the error in phasor measurements [35], [36]. This is inevitable since an error in time synchronisation will always be present. The significance of this error is dependant on the magnitude and phase angle of the signal, as well as the total time inaccuracy [36].

Assume two PMUs are used to measure the same signal. Under ideal conditions the difference in phasor magnitude and phase angular recordings has to be zero.

If a difference in time-stamping is present then one of the PMUs did not sample at the exact same point in time, which would cause a difference in measured values. This is shown in Figure 2-22.

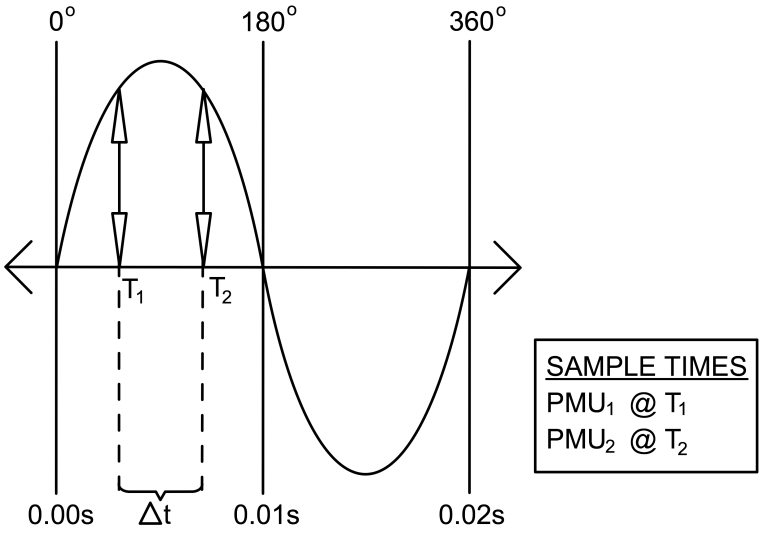

Figure 2-22: PMU samples with time synchronisation error of Δt

A time stamping difference, Δt, then exists. This causes the synchrophasor data to have a phase angle error of $\Delta\phi$, given as

$$\Delta\phi = \frac{\Delta t}{0.02s} \times 360^{\circ}$$

At distribution voltage level the phase angles are much smaller than measured in transmission systems. The micro-synchrophasor (discussed in the next section) must have a considerable smaller time uncertainties to ensure measurements are accurate in the order of millidegrees [19].

2.5.4.4 Applying synchrophasors for stability supervision

Power system stability have traditionally been estimated by mathematical models using passive load flow studies. These state estimation techniques require complex arithmetics

that included iterative calculations to obtain an estimation of the grid conditions.

The inability of such applications to monitor increasingly dynamic profiles have caused conventional steady-state estimators to become impractical to use [37]. A distribution network with a high level of renewable energy penetration will have a significant share in power generation being subject to stochastic changes.

Even with the daily output power profiles of a PV plant being relatively predictable, such predictions can be unreliable due to disturbances that can occur at any given time. The state estimator would therefore be unreliable for networks with integrated RPPs. Synchrophasor recordings introduce the ability of situational supervision between any two locations on a network by means of providing operating visualisation, as shown in Figure 2-23.

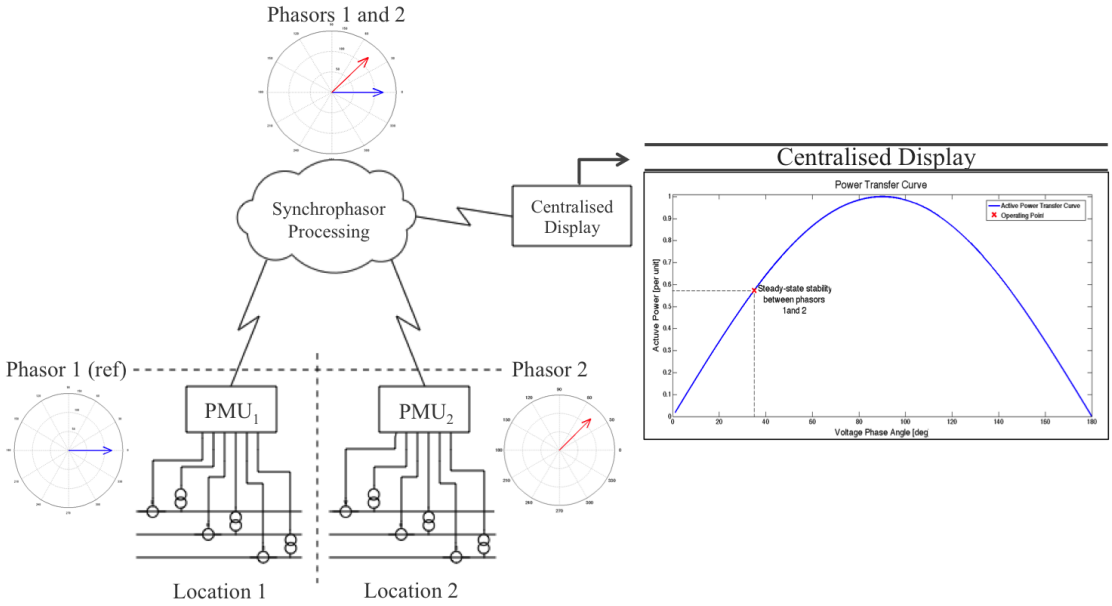

Figure 2-23: Collecting and sampling synchrophasors for visual analysis

The voltage phase angle interaction between two locations monitored with instruments using synchrophasor technology can be displayed in a control room as a support structure in decision making over scheduling loads, switching lines and setting voltage levels.

Sufficient synchrophasor recorders can enable system operators to continuously monitor the state of the network on a widespread scale without the need of complex, and possibly inaccurate state estimation.

2.6 The micro-synchrophasor

The infrastructure of distribution systems are currently subject to developments such as the downstream addition of new consumers as well as the integration of renewable energy

sources. These developments caused concern over the reliability of distribution network operation. It spurred on the need for synchrophasor-based monitoring in distribution networks.

The intent is to provide the same level of visibility that conventional synchrophasors introduced to transmission systems [10]. The term and concept of the micro-synchrophasor was first used in [19]. It refers to high-resolution synchrophasor recordings in the order of μ-seconds.

2.6.1 Micro-synchrophasor application in distribution networks

An opportunity to use the synchrophasor, now termed the micro-synchrophasor was therefore perceived. The spectrum of possible distribution network applications for micro-synchrophasor measurements include a wide range of possibilities [10]:

- State estimation enhancements
- Post-mortem studies
- Grid synchronisation
- Voltage stability
- Distribution line parameter measurements
- Steady-state and transient stability limit monitoring
- Inter-area oscillation

Effectiveness of these applications rely on the sampling resolution, accuracy and the time-stamp uncertainty in measurements. Other factors influencing the reliability in recordings include aspects such as signal latency, data transfer continuity and device communication speed.

The dynamic profiles of renewable energy generation in distribution systems can have sudden changes at angular variances considerably smaller than in transmission systems. The high resolution measurement capabilities that enable micro-synchrophasor recordings to detect small phase angles would therefore be well suited for renewable energy monitoring applications.

The goal of micro-synchrophasor recordings at a PV plant and at another point in the distribution system is to qualify and quantify the interaction between the distribution system and the PV plant. This concept is illustrated in Figure 2-24:

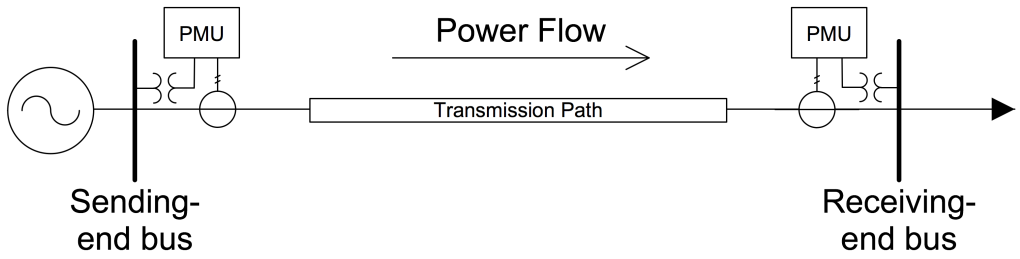

Figure 2-24: Phasor measurements to enable micro-synchrophasor supervision on RPP integration

The demonstrated implementation of micro-synchrophasors in Figure 2-24 would provide visualisation on the state of distribution system stability. Steady-state and voltage instability margins induced by dynamic behaviour of RPPs, such as PV power plants, can subsequently be monitored by micro-synchrophasor data.

2.6.2 Metrological requirements of micro-synchrophasors

The significant difference of micro-synchrophasors to the traditional synchrophasors is dictated by the requirement to measure substantial smaller angular values, while also adhering to the IEEE standard C37.118.1-2011 for synchrophasor measurements.

Not only should micro-synchrophasors adhere to the synchrophasor criteria in the IEEE standard C37.118.1-2011, but it should have the ability to do so within an uncertainty in angular measurements in the order of millidegrees [35]. Sampling capability requirements for micro-synchrophasor recordings have been proposed by [19].

The proposed sampling requirements for synchronised phasor measurements to qualify as micro-synchrophasors are adapted from [19] to a 50 Hz nominal frequency system and are used as baseline requirements together with the IEEE standard C37.118.1-2011 sampling criteria. These adapted requirements are presented on a logarithmic time scale in Figure 2-25.

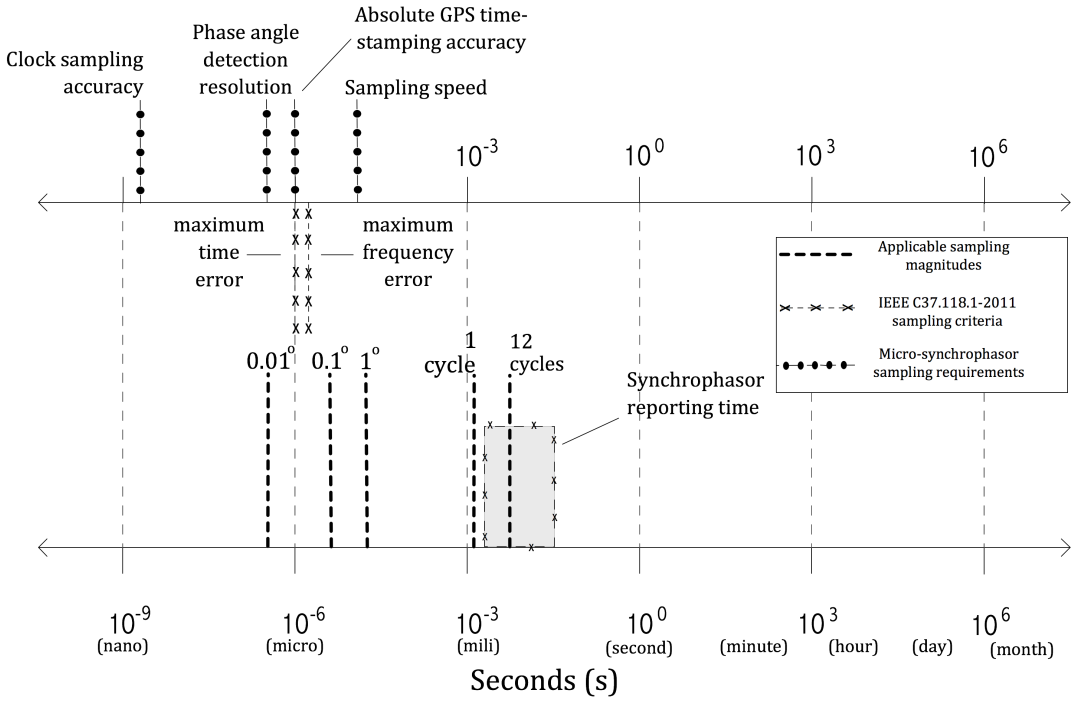

Figure 2-25: Proposed micro-synchrophasor sampling requirements [19]

The angular sampling magnitudes shown in Figure 2-25 are included as reference to illustrate the associated required sampling time to be able to record such values. A single cycle (360°) of the fundamental system frequency has a duration of 20 ms, indicating that a phase shift of 1° occurs within 55.6 μs.

Given the fact that distribution voltage levels also include LV level networks (< 1000 V), with relative low impedances the phase angle variations may be tenths of a degree.

For micro-synchrophasor recordings to detect a phase angle change of 0.1° in a 50 Hz system, the instrument needs a sampling speed of:

$$\text{Sampling speed} = \frac{0.1°}{360°} \times 20 \text{ ms} = 5.6\,\mu s \text{ per sample} \tag{2.74}$$

This indicates that the sampling resolution for micro-synchrophasor recordings need to be in the order of μ-seconds, making it appreciable where the term "micro"-synchrophasors originates.

According to the IEEE C7.118.1-2011 criteria, the maximum permissible time error in measurements may not exceed 1 μs [12].

This requirement is also applicable to micro-synchrophasors, which would make the required accuracy in micro-synchrophasors measurement very stringent. The main reason for this is the angular differences between micro-synchrophasors can be as small as 0.01°.

Moreover, these phase angle could also change rapidly due to the dynamic character of distribution systems with renewable energy sources. A PV plant, for example, does not have mechanical inertia, which enables a faster change in output levels that can abruptly change the phase angle.

The metrological micro-synchrophasor sampling requirements, presented in Figure 2-25, are based on the micro-phasor measurement unit (μPMU) requirements introduced in [19].

It is proposed that the micro-synchrophasor angular resolution must be sufficient to detect phase angle differences between 1.0° and 0.01° [19], which would require a sampling resolution up to 0.56 μs in a 50 Hz system. The recorded micro-synchrophasors must still adhere to the 1% TVE criteria in order to ensure that the data have been measured accurately.

2.7 Photovoltaic energy

The sun is the Earth's most abundant source of energy, inherently making power generation from PV cells one of the profound green-energy sustainable solutions today. On a cloudless day the incident irradiance can range between 1000 kWh/m^2 to 2000 kWh/m^2 [38].

During inception of photovoltaic technology, PV arrays were almost exclusively used in spaceships and satellites, primarily due to its high production costs. Over the last decade however, the production costs of PV cells has decreased such that it became commercially available.

Today PV arrays vary from residential rooftop installations in LV networks up to commercial PV power plants operated by IPPs [39]. The South African energy market has seen PV power generation taking a significant share, with an increasing penetration expected as emphasis on a global front is continued to be placed on sustainable energy sources.

2.7.1 Photovoltaic energy characteristics

Figure 2-26 presents a characteristic I-V curve of a PV cell. The I-V curve demonstrates the basic PV parameters under which a PV arrays are rated [39].

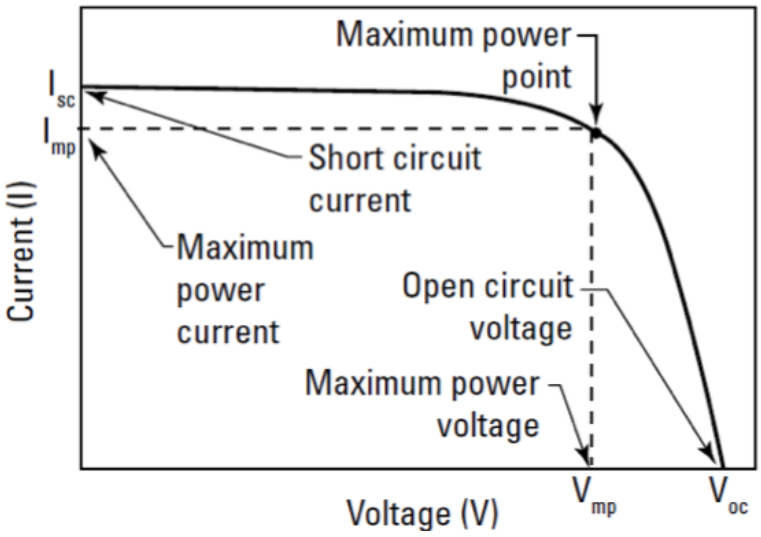

Figure 2-26: I-V curve of a PV cell illustrating it characteristics [39]

Short-circuit current (I_{sc}):

Is the current value achieved when essentially no power is generated. It can be defined as the measured current when the voltage equals to 0.

Open-circuit voltage (V_{oc}):

Represents the maximum voltage at which the current is equal to 0, i.e. the voltage during open circuit conditions.

Maximum power current (I_{mp}):

Represents the current value at which maximum power is generated.

Maximum power current (V_{mp}):

Represents the voltage value at which maximum power is generated.

Maximum power point (MPP):

It is the ideal point on the I-V curve where generated power is at a maximum. The maximum power generated occurs at the point of an I-V curve where the optimal current-voltage relationship is found.

PV cell efficiency(η):

PV cell efficiency is an indication of the total amount of irradiance power (W/m^2) converted to electric power. It is expressed as a ratio of maximum power over irradiance power [40]:

$$\eta = \frac{V_{mp} \times I_{mp}}{I(t) \times Area} = \frac{P_{MPP}}{P_{in}} \tag{2.75}$$

2.7.2 Influences of varying ambient conditions

Stochastic ambient conditions induce variations in PV generation, which cause power output disturbances. The variant ambient conditions specifically influence the voltage and current profiles of PV arrays.

These characteristics can be quantified by means of investigating the changes due to varying temperature and irradiance on I-V curves, as shown in Figure 2-27a and b:

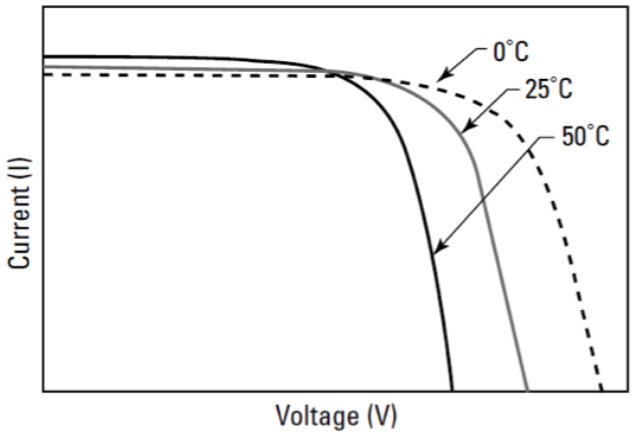

(a) Varying temperature

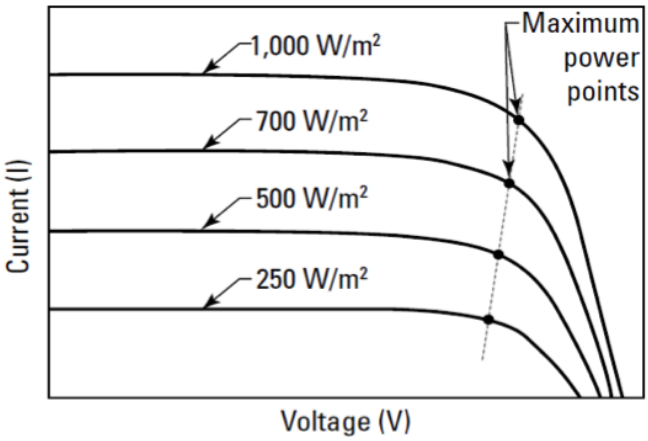

(b) Varying irradiance

Figure 2-27: Influences of varying ambient conditions on PV power [40]

Variance in Temperature

A common misconception exists that electrical energy generated by PV power plants is higher in heated conditions. The changing I-V curve in Figure 2-27a in at varying temperature during constant irradiance illustrates an inverse correlation between cell temperature and generated voltage [40].

As temperature increase, generated voltage decrease. A source of renewable energy will be exposed to temperature changes during the day as function of the hour of the day and

the wind speed.

It is expected to be a relative slow change that should not impact voltage stability of the network as tap changers, for example, will be able to mitigate changes effectively.

Variance in Irradiance

Current and voltage are proportional to the level of irradiance. The increments in current however are the most significant and is considered as the main contributor to the correlation in increased power generation.

The increments in voltage levels variate in small quantities and is regarded to remain constant [40]. Summarising voltage and current characteristics during varying ambient conditions:

- **Voltage:** Decreases as cell temperature increase. Remains constant during irradiance changes.

- **Current:** Increases as irradiance levels increase. Remains constant during varying cell temperature.

2.8 Considerations on the integration of distributed generation

2.8.1 How renewable energy impact network integration

Network integration of renewable energy sources comprise different behaviour characteristics compared to conventional fossil fuel power plants. The following changes to the power system are being introduced by RPPs, specifically by sources such as PV power which is directly converted to electrical energy by power electronics [38]:

a) Decentralised power generation distributed all over the distribution system whilst the traditional sources normally injects into a transmission system.

b) Instantaneous phase angle shifts are possible due to the lack of mechanical inertia.

c) RPPs generate only when the energy source is available, i.e. PV generation is during daytime.

d) The output levels can be stochastic due to varying ambient conditions.

The infrastructure of distribution networks was not designed for generation applications. However, the acquisition of renewable energy sources is in principle beneficial to the grid. Not only from an environmentally sustainable perspective, but also from a power supply

point of view.

During stable ambient conditions the RPP output power only changes gradually. Variations in the production levels will be too slow for the RPP to affect network reliability. These conditions subsequently enable RPPs to perform as they were attended to do.

Extra power capacity would be added to the grid and the voltage across distribution lines will be less susceptible due to the integration of an RPP.

When considering generation during varying conditions, an abrupt change in the output power could disturb the system. If the RPP is large enough it can cause detrimental effects such as power swings in transient conditions. This will evidently induce unstable voltage conditions, which may lead to a system collapse [38].

To date, the impact of RPPs on distribution networks have not been quantified [41]. RPPs affect networks differently, making it important to study each case separately be quantifying its impacts on the grid [38].

2.8.2 Network integration points

To research the impact of renewable energy integration on distribution networks, the locatations of the recording instruments must be determined. Naturally, the first connection point where the RPP is synchronised to the network would be the primary location to monitor its output.

The location to best monitor dynamic interaction the RPP has with the network is at the upstream distribution station where the RPP ties into the network.

These two locations are described below.

2.8.2.1 Point of Connection (PoC)

The point that initially connects the outputs of the PV arrays so that it may integrate with the grid is defined in this study as the Point of Connection (PoC). At the PoC the renewable power plant is synchronised with the network. The output voltage levels are stepped up with power transformers to match the nominal voltage level of the distribution network at the PoC.

The frequency and phase relation is synchronised with the distribution system. It serves as reference for the PV power plant operation.

Conventionally, the PoC feeds through a connecting line to the Point of Common Coupling (PCC) of the distribution system as the RPP can be located some distance away.

2.8.2.2 Point of Common Coupling (PCC)

The referral point where the output power of the PV power plant connects with the first utility bus is known as the Point of Common Coupling (PCC). The PCC represents the connection at a distribution station in the distribution network where other incoming lines and downstream feeders interconnects.

The network operator has to manage QoS at the PCC to ensure that other parts of the network and clients are not adversely affected due to the RPP injecting energy at this point. PQ monitoring at this point can be used to assess the QoS.

At planning level the QoS at the PCC is used by the NSP to identify the QoS levels that will require intervention to prevent that QoS do not degrade beyond the compatibility levels set by then NRS 048 part 2-2007 for the voltage level applicable.

The means to monitor interaction of the RPP between the PoC and PCC is presented in Figure 2-28 below.

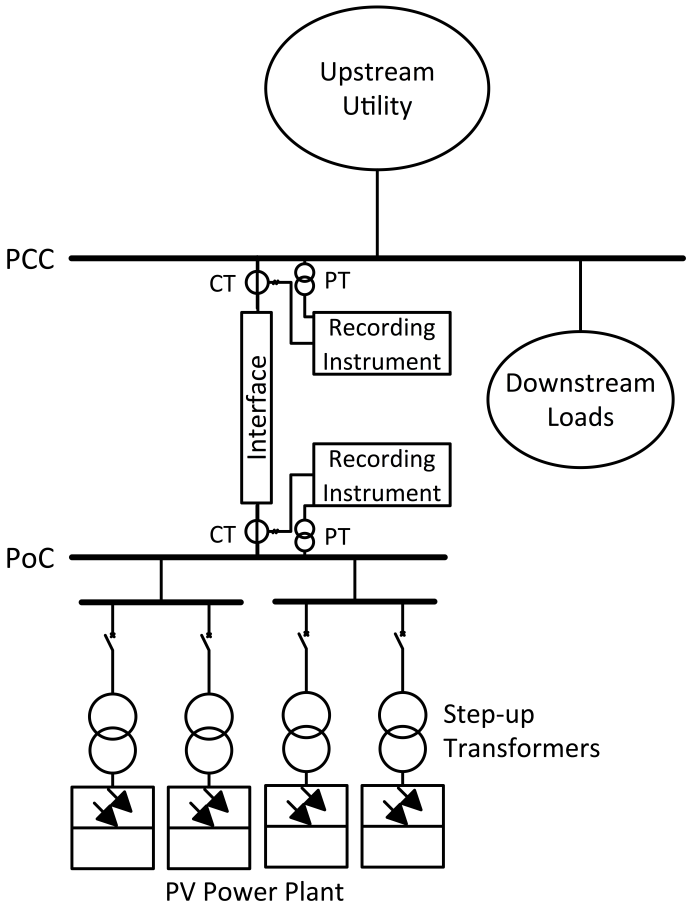

Figure 2-28: Conventional means to monitor DG supply at the PCC

2.8.3 Grid code compliance

Private investors (IPPs) owning RPPs sell electrical energy to the utility, who previously was the only role-player in power generation. With the addition of multiple IPPs strict requirements for any non-utility form of integrated generation were introduced.

The grid compliance codes for interconnecting renewable power plants (RPP) with the South African distribution grid have been issued by the RSA Grid Code Secretariat and is approved by the National Energy Regulator of South Africa (NERSA) [42].

RPP grid code compliance levels are set out by NERSA, the acting legislative body, in order to specify the minimum technical grid interconnection requirements to which every RPP must abide. The requirements apply to all the predominant renewable energy sources, namely [42]:

a) Photovoltaic (PV)

b) Concentrated Solar Power (CSP)

c) Hydro Power

d) Landfill gas

e) Biomass

f) Biogas

g) Wind turbines

2.8.3.1 Renewable Power Plant (RPP) Size Categories

Grid interconnection requirements are dependant on the RPP size, since grid penetration impacts will differ according to the amount of power injected onto the local network. Three categories have been defined according to the apparent power capacity.

a) Category A: 0 - 1 MVA

   Category A size usually integrates with LV networks. The NRS097-2 compliance levels of LV RPP dictates that any grid-connected RPP with a capacity greater than 4.6 kVA must be a balanced three-phase power source. RPP category A is redistributed in to three sub-categories [42]:
   A_1: 0 - 13.8 kVA
   A_2: 13.8 kVA - 100 kVA
   A_3: 100 kVA - 1 MVA

b) Category B: 1 - 20 MVA

Category B RPPs are usually connected at MV levels. In the South African energy market grid-connected RPPs greater than 1 MVA are commercially operated by IPPs and monitored by the system operator.

c) Category C: 20+ MVA

Similar to category B , the category C RPPs are commercial operated grid-connected power plants and are operated by IPPs. The majority of category C RPPs resides at the higher-end distribution system voltage levels in South Africa.

2.8.3.2 Voltage compliance

A RPP integrating with the local network must withstand any voltage deviation at the point of connection (PoC) under normal and abnormal operating conditions and will not impair voltage stability of the local network.

(**A**) Voltage Requirements During Normal Operating Conditions

Table 2-2 denotes the range of nominal system voltage to which all categories must abide to at the PoC.

Table 2-2: Voltage regulation compliance criteria for RPPs.

Category	Voltage Magnitude Range
A.	-15% < A < +10%
B.	-10% < B < +10%
C.	-10% < C < +10%

The voltage regulation compliance levels for RPPs at the PoC listed in Table 2-2 have been specified in accordance with the National Regulatory Standards (NRS) for Quality of Supply (NRS 048:2-2011) criteria.

These requirements are applicable during normal network operation. A different set of voltage criteria is relevant to RPPs during abnormal operating conditions, as described below.

(**B**) Voltage Requirements During Abnormal Network Operation

The following requirements and guidelines are compulsory for RPPs connecting with the National Integrating Power System (NIPS):

- The integrating RPP must remain connected to the PoC during a voltage phase shift of up to 40° without compromising its output.
- A maximum settling duration of 5 seconds is allowed for the RPP to revert to normal operation after a phase shift disturbance.

- The RPP shall remain connected to the PoC during a voltage interruption where the voltage magnitude falls to 0 for up to 0.15 seconds.
- Overvoltages up to 120% nominal voltage magnitude for at least 2 seconds may occur before the RPP can disconnect.

RPP categories A_1 and A_2 must comply with the voltage ride-through criteria, demonstrated in Figure 2-29.

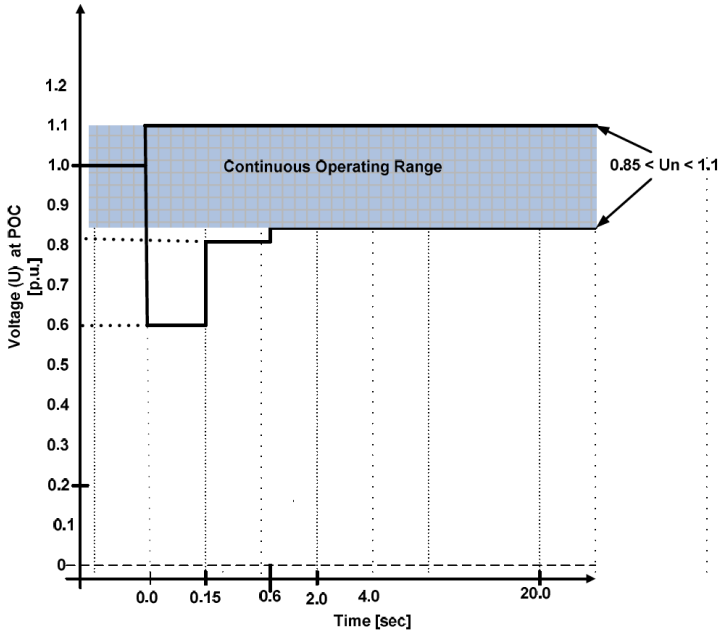

Figure 2-29: RPP categories A1 and A2 voltage ride-through criteria [42].

Voltage ride-through requirements specified for RPP of categories A3, B and C are shown in Figure 2-30 and includes symmetrical and asymmetrical faults that are accountable for all phases.

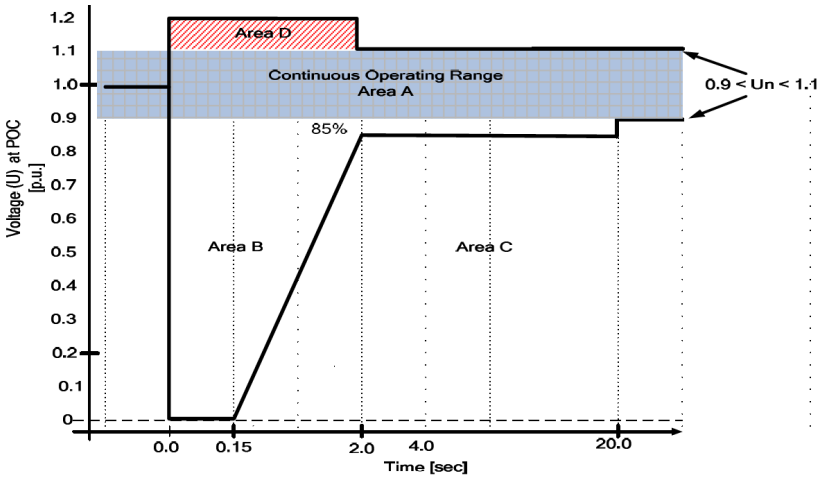

Figure 2-30: RPP categories A3, B and C voltage ride-through criteria [42].

2.8.3.3 Frequency compliance

The interconnected RPP must remain connected to the NIPS during normal operation and during a rate of change of frequency of 1.5 Hz/s. For stability purposes, the RPP may not arbitrary disconnect from the network, unless during a frequency disturbance for which specified disconnecting time frames are listed.

a) Normal Frequency Operation Requirements

- Frequency of the RPP will constantly range between 49 Hz - 50.2 Hz.
- Provided the system frequency is within the allowable operating range, the RPP will stay interconnected during a frequency rate of change of up to 1.5 Hz/s.

During the case where nominal system frequency exceeds 50.5 Hz, the RPP needs to reduce active power to compensate for the frequency change, as indicated in Figure 2-31:

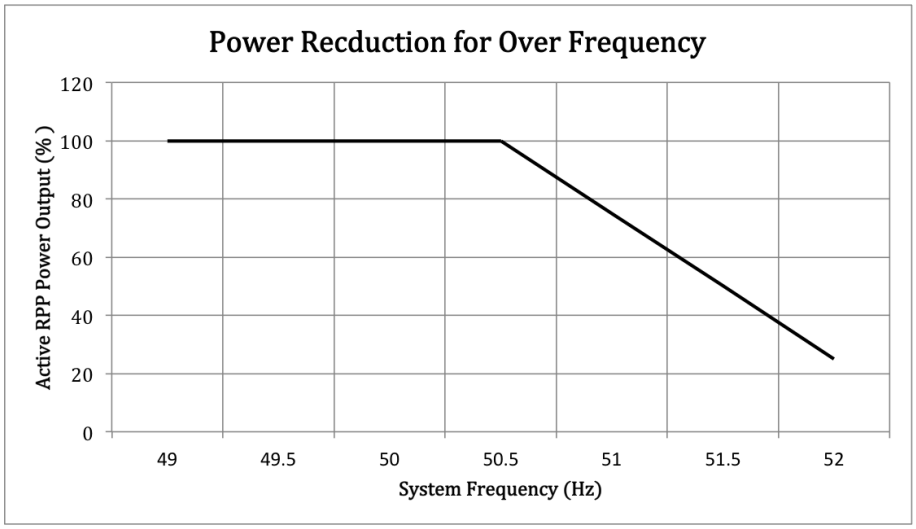

Figure 2-31: RPP active output power reduction in response to over-frequency [42].

b) Requirements During Frequency Disturbance

RPPs must be designed so that they are capable of disconnecting with the local network when the minimum operating range of the RPP system frequency does not comply with the given criteria [42].

- When system frequency is greater than 52 Hz, for a duration longer than 4 seconds, the RPP must disconnect from the network.
- The RPP must disconnect from the PoC when system frequency is less than 47 Hz for longer than 200ms.

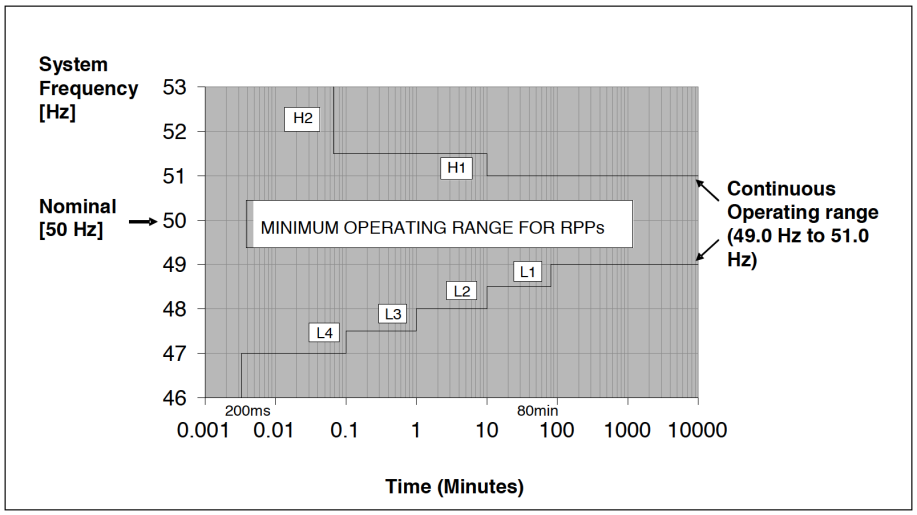

Figure 2-32: Cumulative disconnect time ranges and frequency criteria over the life range of the RPP [42].

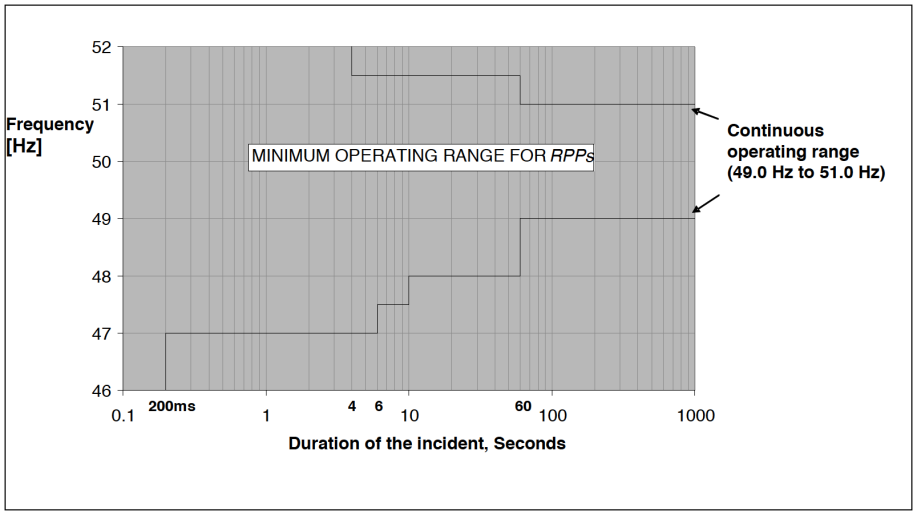

Figure 2-33: Disconnect criteria for system frequency disturbance events [42].

The cumulative disconnect time ranges and frequency criteria over the life range of the RPP is given in Figure 2-32, while the disconnect criteria for frequency disturbance events are demonstrated in Figure 2-33, represented above.

2.9 Conclusion

In this chapter the relevant aspects entailing the application of micro-synchrophasors to monitor a PV power plant integrated onto a distribution network have been presented. The fundamentals of phasors in a power system were used to analyse the features of synchrophasor measurements.

Fundamental principles for synchrophasor measurements have been discussed, including the means on how synchronised measurements are initiated to obtain voltage phase

angle measurements. Aspects pertaining to the root causes for synchrophasor measurement errors were investigated, with an evaluation surrounding the measurement criteria stipulated by the IEEE C37.118.1-2011 Standard for Synchrophasor Measurements [12] following afterwards.

The micro-synchrophasor, presented in Section 2.6, was evaluated by firstly identifying the fundamental difference between micro-synchrophasors and conventional synchrophasors. During this evaluation the motive and grounds to the acclaimed term "micro"-synchrophasor were presented.

The proposed metrological capabilities for micro-synchrophasors stated that sampling resolutions in the order of μ-seconds are required to measure angular variations of 0.01°. These proposed requirements were indicated on a logarithmic time scale.

Typical applications for micro-synchrophasor measurements in distribution networks have been listed, with network stability supervision emphasised. Network stability supervision is required to assess the impact of stochastic output profiles associated with RPPs.

The goal of micro-synchrophasor application on PV power plant integration is to extract small signal stability information to enable a better understanding of the dynamic phenomena when sources of renewable energy are located all over the distribution system.

The mechanism by which a PV plant can cause network instability was investigated. Varying temperature and irradiance levels were investigated how they affect variation the output of PV generation.

The PCC and PoC in the network where measurement of micro-synchrophasors should be done to diagnose integration impacts, was motivated. RPP integration is subject to grid compliance criteria that has been issued by NERSA in [42] and is listed in the final section of this chapter.

Conclusively, Chapter 2 elaborated on the various aspects how micro-synchrophasor application can be utilised to monitor stability of a distribution network with integrated PV plants. It is clear that micro-synchrophasors can bring the sophistication in analysis and control of distribution networks envisaged by the smart grid vision.

Chapter 3:
The Metrology of the Micro-Synchrophasor

3.1 Introduction

The concept of applying synchrophasor measurements at distribution voltage levels as micro-synchrophasors is novel. To date, a few published studies reported the validity of micro-synchrophasors [19], [10]. As such, metrological tests need to be conducted to determine whether the recording instruments that will be used during the field studies are capable of measuring micro-synchrophasors.

The instruments that have been used are IEC 6100-4-30 Class A ed. 3 certified PQ analysers comprising embedded synchronised phasor recording capabilities. As these instruments are representative of the latest advances possible in commercial measuring instrumentation, it was used to validate the practicality for engineers to consider the micro-synchrophasor at all.

This chapter tested and evaluated the metrological capabilities of the recording instruments and their compliance to the proposed micro-synchrophasor requirements [19]. Tests were conducted using two micro-synchrophasor recorders, time-stamped by different GPS units. The recorders measured the phase angle differences between two separate 50 Hz signals. The phase angles were systematically decreased during the measurements to determine the absolute accuracy of the recorders. Results were compared to the proposed metrological requirements for micro-synchrophasors [19].

After the accuracy tests, the certainty in phase angle measurements between two micro-synchrophasors were evaluated. This was conducted by applying two micro-synchrophasor recorders on an identical 50 Hz signal. The error in recorded angular differences was assessed to account for the level of certainty in measurement. Evaluations on the absolute accuracy in phase angle measurements, as well as the level of certainty in measurement between micro-synchrophasor recordings, served as verification of the metrological performance of the instruments to be used in field studies.

A final test, serving as supplementary verification, was conducted by calculating the impedance of a LV distribution cable. The line impedance measured by a high precision

EN 60909-0 loop impedance meter was used as benchmark for verification. The values were measured as accurately as possible due to the calibration status and performance of the specific impedance meter used. This test also provided validation on the practicality of micro-synchrophasor recordings in distribution networks.

3.2 Micro-Synchrophasor Verification with CMC 256plus™

Micro-synchrophasors require high-precision recordings of phase angles between two phasors. These recordings must also occur at a sufficient resolution that will enable detection of small angular changes at an acceptable certainty.

It is important that the recording instruments meet these requirements to verify their capabilities of conducting micro-synchrophasor measurements. The technical specifications and features of the IEC 61000-4-30, ed. 3 Class A PQ instruments used are listed in Appendix A.

3.2.1 Accuracy Tests with Small Phase Angle Shifts

The absolute accuracy of two micro-synchrophasor recorders was tested using waveforms generated by an Omicron CMC 256plus™ high precision signal generator. Each micro-synchrophasor recorder with its own GPS unit was subjected to three-phase 110 V, 5 A waveforms at 50 Hz.

Measurements were executed by keeping the phase of one of the voltage waveforms as reference while the second voltage waveform was phase shifted at pre-considered and fixed intervals. These tests aimed to verify if the recorders' synchronised phasor recording abilities are within the requirement for micro-synchrophasors [19].

Since the purpose of these tests are to establish credibility at small angular level measurements, the phase angle values have been substantially decreased. However, the ability to emulate micro-degree phase angles were limited by the lowest phase angle increment (0.010°) that the CMC 256plus™ could generate. Three different test cases were evaluated.

a) The 1st test comprised a phase angle difference between the two voltage waveforms of 5.00° that was decreased by 5 intervals of 1.00° down to 1.00°.

b) During the 2nd test a 1.00° phase angle difference was used and decreased down to 0.10° at intervals of 0.10°.

c) The 3rd test started with a phase angle difference of 0.10° and decreased down to 0.01° (the smallest phase angle quantity the CMC 256plus™ signal generator could produce) by 0.01° decrements.

Using the generated signal of the CMC 256plus™ as benchmark, the accuracy of the recorders to measure small voltage phase angles was determined. Results of the measurements were compared to the micro-synchrophasor angular requirements [19] to verify the instruments' to measure small phase angles.

Table 3-1 lists the test conditions. Each interval in phase angle was repetitively recorded in order to fully capture the steady-state condition of the measurement setup. A 100 phasor values for each interval were recorded by the instruments to allow the results to be statistically evaluated.

Table 3-1: Test conditions

	Reference phase angle	**Phase angle shifts towards reference waveform**	**Number of shifts**	**Total recorded phasors**
Test 1	5.00°	1.00°	5	500
Test 2	1.00°	0.10°	10	1000
Test 3	0.10°	0.01°	10	1000

A representation of the test setup used to conduct micro-synchrophasor uncertainty of measurement verification through small phase angle shifts is shown in Figure 3-1.

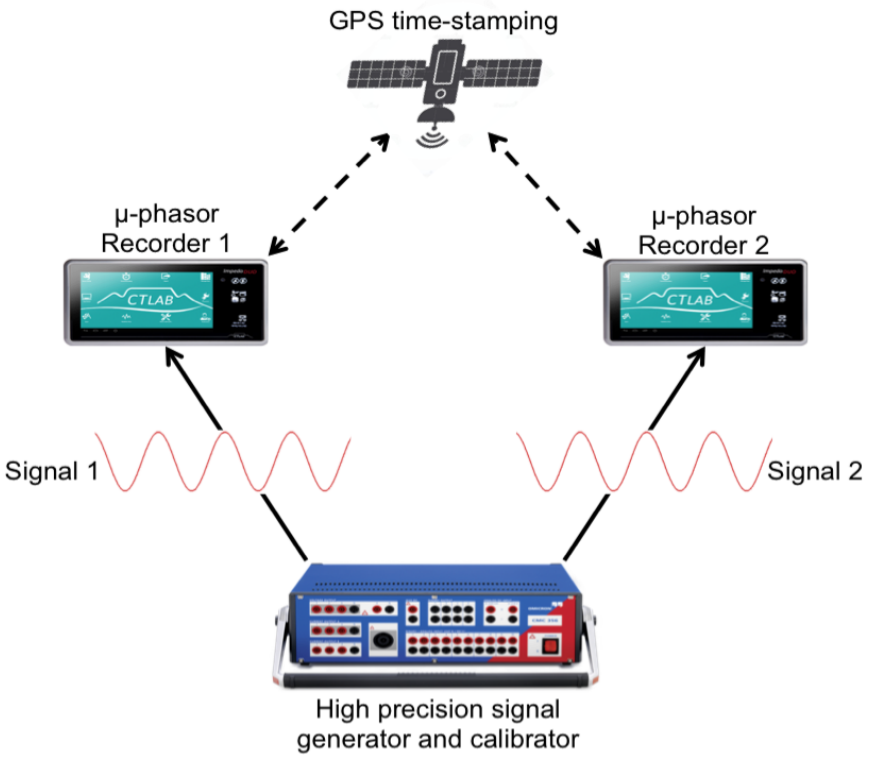

Figure 3-1: A high precision signal generator is used for the micro-synchrophasor phase angle measurements

The waveforms were generated on two separate embedded channels of the CMC 256plus™ high precision signal generator. Phase angle magnitudes were marshalled in the Test Universe ® interface.

The statistical analysis of the recorded data consisted of calculating the mean phase angle deviation from the generated value, the standard deviation of that difference based on the total number of phasors recorded for each test, the mode (modus) of the phase angle difference value and the frequency distribution of phase angle differences.

The listed symbols below represent the statistical parameters used:

$\overline{x}$ Mean value
σ_x Standard deviation
M_0 Mode value
fx Frequency distribution

3.2.1.1 Test 1

The micro-synchrophasor requirements [19] states that a phase angle value of at least 1.00° must be detectable by recorders used. Figure 3-2 illustrates the micro-synchrophasor recordings from 5.00° down to 1.00° at 1.00° phase shifts.

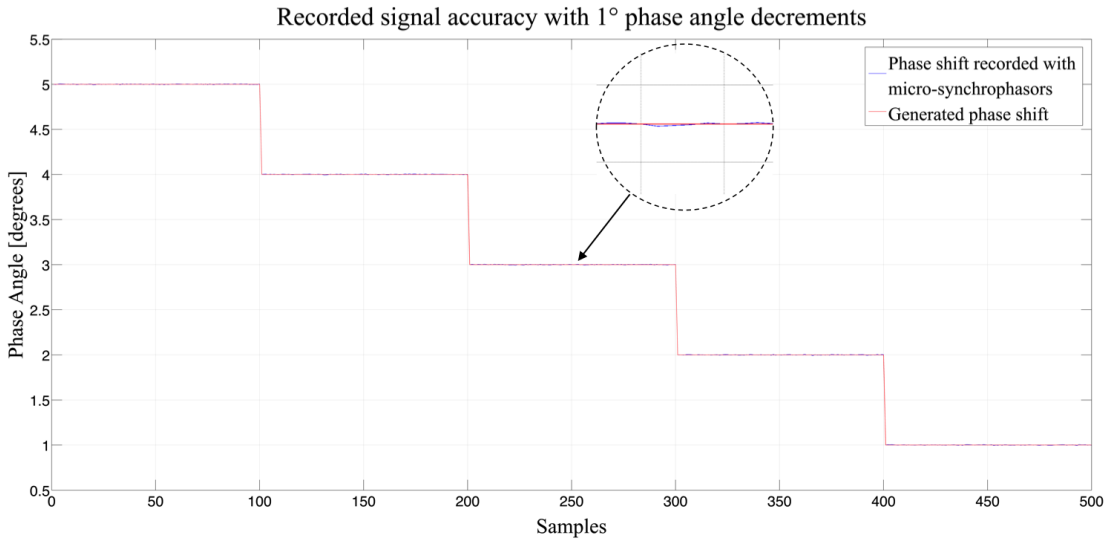

Figure 3-2: Recorded phase angle difference (blue) compared to the generated phase angle difference (red)

The difference between the generated phase angle difference and recorded phase angle difference are almost indistinguishable, which gives indication of high-precision clock accuracies between the recorders. For a 1.00° phase angle shift to be detected in a 50 Hz system the recordings required a sampling resolution of 55.6 μs or better.

The micro-synchrophasors were measured at an average TVE of 0.05%, validating that the minimum requirement for micro-synchrophasor recordings has been met. The statistical results for each phase shift are listed in Table 3-2.

Table 3-2: Statistical results for test case 1

Test 1			
Phase angle difference	**Mean recorded phase angle [$\overline{x}$]**	**Standard deviation [σ_x]**	**Recorded mode value [M_0]**
5.00°	5.0005°	0.0023°	5.0019°
4.00°	4.0010°	0.0022°	3.9958°
3.00°	3.0005°	0.0025°	2.9977°
2.00°	2.0004°	0.0027°	1.9969°
1.00°	1.0005°	0.0022°	1.0021°

Results are presented up to four decimals in order to determine the accuracy of the recorded phase differences.

The mean value of all the phase angle differences recorded was calculated as 0.00058°. The standard deviation during these phase shifts ranged between 0.0022° and 0.0027°.

Mode values (most frequent recorded) of angular difference for each increment were correlated to the actual phase shift value by a deviation by a range of 0.105% to 0.038%.

3.2.1.2 Test 2

Detection of a 0.10° phase angle shift would require a sampling resolution of:

$$\begin{aligned} \text{Sampling resolution} &= \frac{0.10^\circ}{360^\circ} \times 0.02\ s \\ \text{Sampling resolution} &= 5.56\ \mu s \end{aligned} \tag{3.1}$$

Such angular shifts are expected to occur at LV (consumer) level operation. The measured phase angle magnitudes in this test are well within the spectrum of the metrological micro-synchrophasor requirements to measure angles between 1.00° and 0.01°.

Figure 3-3 illustrates the phase angle differences recorded for test 2.

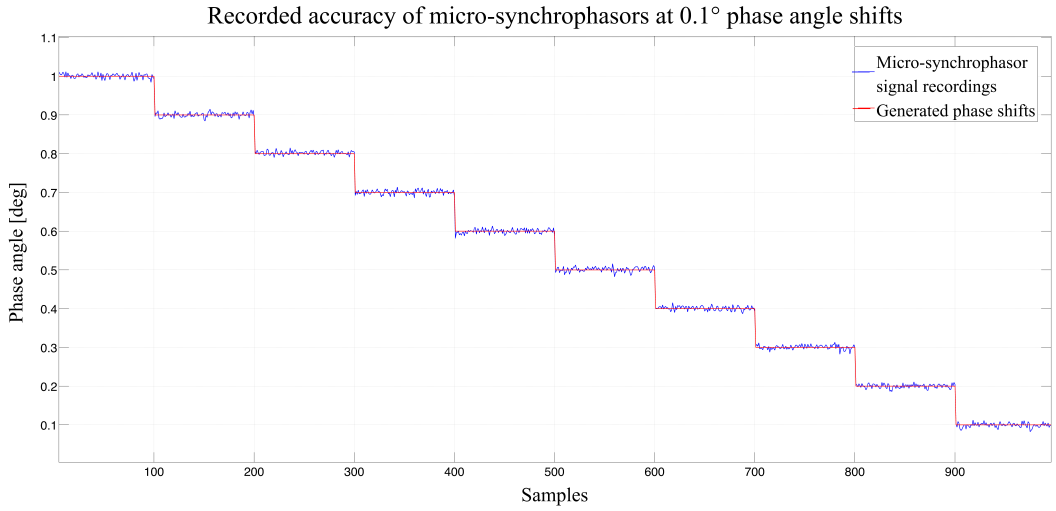

Figure 3-3: Recorded phase angle difference (blue) compared to the generated phase angle difference (red)

It can be seen that a variation of the phase angle differences is present. It appears evenly distributed across the generated angular values and resulted in an average difference of 0.00073° to the generated signal. On average the recorded micro-synchrophasors comprised a TVE of 0.7%. The statistical results for Test 2 are given in Table 3-3.

Table 3-3: Statistical results for test case 2

Test 2			
Generated phase angle	**Mean recorded phase angle [$\overline{x}$]**	**Standard deviation [σ_x]**	**Recorded mode value [M_0]**
1.0°	1.0005°	0.0022°	1.0021°
0.9°	0.9007°	0.0021°	0.9100°
0.8°	0.8010°	0.0024°	0.7988°
0.7°	0.7012°	0.0022°	0.6971°
0.6°	0.6007°	0.0025°	0.5950°
0.5°	0.4991°	0.0025°	0.5020°
0.4°	0.4010°	0.0023°	0.4018°
0.3°	0.2996°	0.0020°	0.3009°
0.2°	0.1995°	0.0021°	0.1890°
0.1°	0.0994°	0.0022°	0.0861°

The standard deviation varies in the same range as Test 1, this case between 0.0020° and 0.0025°. Due to the notable oscillations noted in Figure 3-3 the recorded mode values deviates by a higher percentile for this test range. This can expected since angular magnitudes were recorded at a tenth of the previous test values.

3.2.1.3 Test 3

In this 3rd test the phase angle was decreased from 0.10° to 0.01°, which is the smallest value the CMC 256plus™ can generate. A 0.01° phase shift at 50 Hz will occur within:

$$\begin{aligned} \text{Samplingresolution} &= \frac{0.10°}{360°} \times 0.02\ s \\ \text{Samplingresolution} &= 0.556\ \mu s \end{aligned} \tag{3.2}$$

Should data sampling be slower than 0.556 μs, phase shift of 0.01° would not be detected. This evidently necessitate high resolution recordings.

Measuring down to a 0.01° phase angle difference has tested the instruments' metrological capabilities for the most stringent angular requirements for the micro-synchrophasor, since it is proposed that μPMUs should detect angular differences between 1.00° and 0.01° [19].

Figure 3-4 displays the recorded results of test 3.

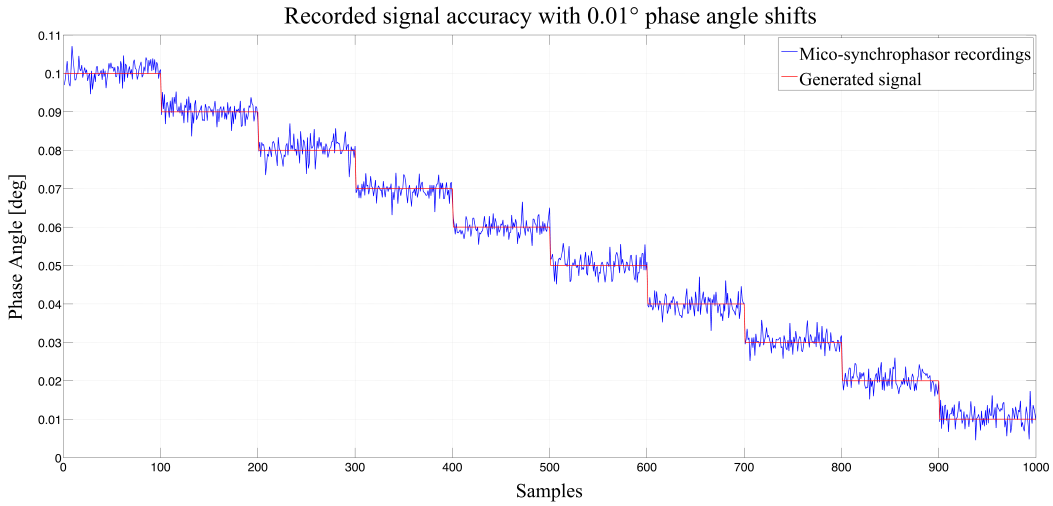

Figure 3-4: Recorded phase angle difference (blue) compared to the generated phase angle difference (red)

The recorded oscillations shown in Figure 3-4 are prominent compared to Test 2. The reason for this is due to the phase angles in Test 3 being a tenth of a degree. This caused the oscillations to be more notable than in Test 2, but when comparing Test 2 and 3 it can be seen that the recordings oscillated at the same angular levels.

A TVE of 0.3% has been calculated with a 0.00033° average difference from the generated phase angle values. The statistical results for Test 3 are presented in Table 3-4.

Table 3-4: Statistical results for test case 3

Test 3			
Generated phase angle	**Mean recorded phase angle [$\overline{x}$]**	**Standard deviation [σ_x]**	**Recorded mode value [M_0]**
0.09°	0.0902°	0.0022°	0.0885°
0.08°	0.0802°	0.0023°	0.0770°
0.07°	0.0697°	0.0026°	0.0671°
0.06°	0.0599°	0.0023°	0.0586°
0.05°	0.0502°	0.0020°	0.0484°
0.04°	0.0398°	0.0025°	0.0431°
0.03°	0.0303°	0.0023°	0.0326°
0.02°	0.0203°	0.0021°	0.0232°
0.01°	0.0109°	0.0022°	0.0085°

A standard deviation range between 0.0021°- 0.0025° is calculated, which presents a consistent standard deviation range between all three tests. The mode values are affected most at this level where the recorded oscillations caused deviations up to 0.03°, which may negatively influence the certainty of measurement at these levels.

The recording instruments were able to accurately detect all phase angle values between 1.0° and 0.01°. The TVE for all measurements was less than 1%, which also represents compliance to the IEEE Std. C37.118.1-2011 criteria for synchrophasor measurements.

3.2.2 Micro-Synchrophasor Verification: Certainty in Measurement

The accuracy tests in the previous section demonstrated that the synchrophasor recorders intended for this research have met the proposed micro-synchrophasor requirements for angular detection [19].

The following test evaluates the level of certainty in the micro-synchrophasor measurements. A single 110 V, 5 A 50 Hz signal was simultaneously recorded by two synchrophasor recorders, each with its own GPS unit.

When two instruments are measuring the same voltage waveform the instruments should ideally report a 0° phase angle difference. Any recorded angular difference would represent the error in phase angle measurements.

Such errors will essentially be caused by a synchronous time-stamp inaccuracy between the two instruments, which would provide indication to the level of uncertainty in measurement.

The test setup for the certainty in micro-synchrophasor measurements is presented in Figure 3-5.

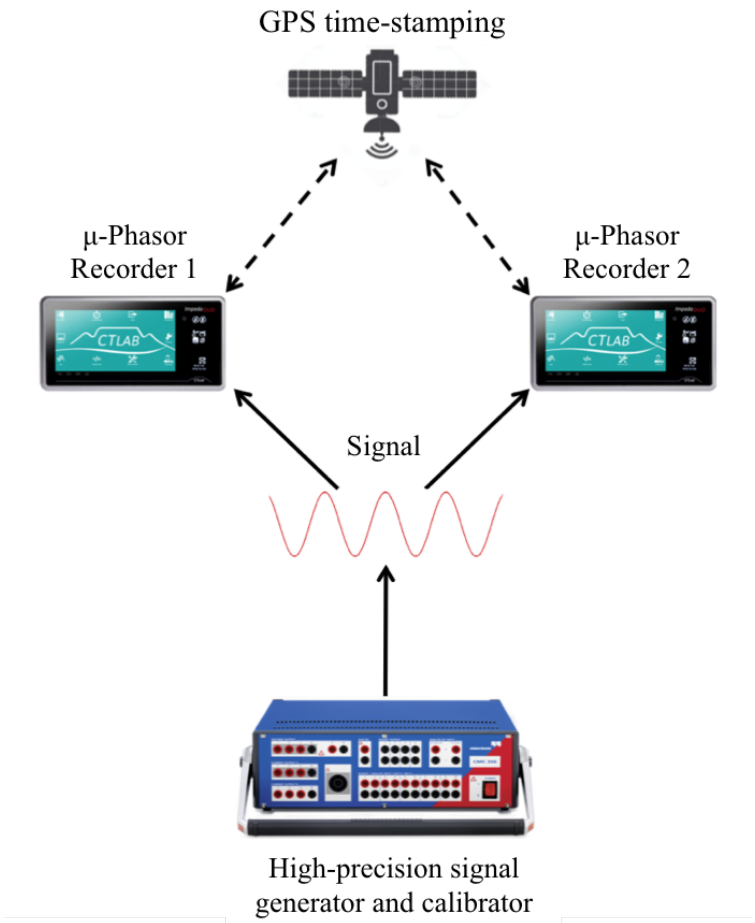

Figure 3-5: Setup used to quantify the certainty in measurement

As discussed in Chapter 2, no measurements are exact, since all measured information are subject to a level of uncertainty.

The concept of certainty in measurement presents a means to characterise the quality of the measured information. By using statistical analysis the level of which uncertainty impairs the quality of the measured data can be determined [31].

Figure 3-6 below presents the phase angle dispersion from an ideal 0° difference between the two instruments.

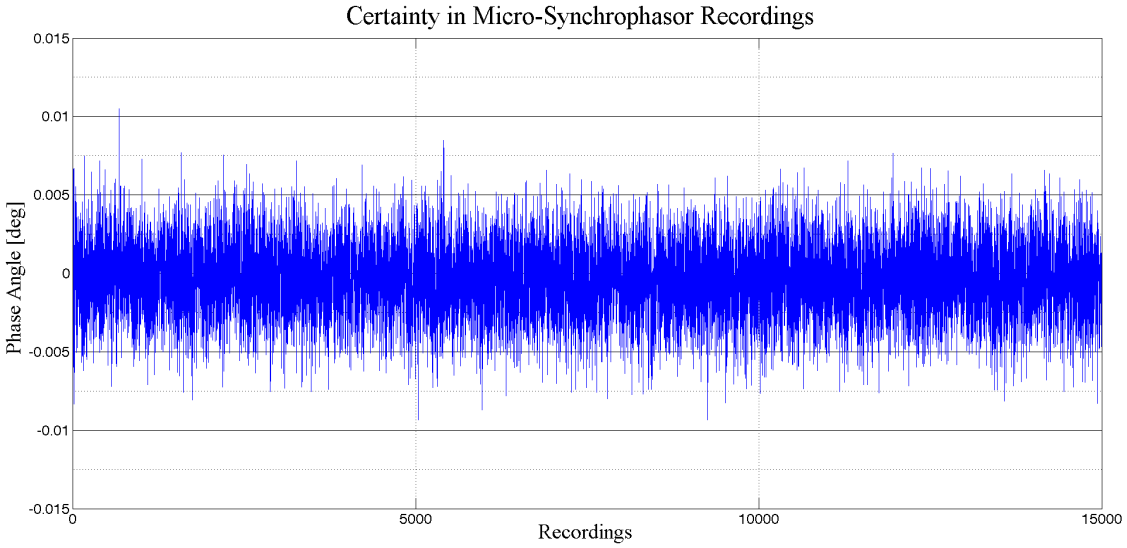

Figure 3-6: Certainty in phase angle measurements: deviation from 0°

As stated earlier, the ideal value should be 0°. A total of 15 000 micro-synchrophasors were recorded for this test. The recorded profile in Figure 3-6 presents a narrowband dispersion from 0°, which ranges between -0.005° and 0.005°.

A histogram of the results is displayed in Figure 3-7 to present the spread of the recorded phase angle differences.

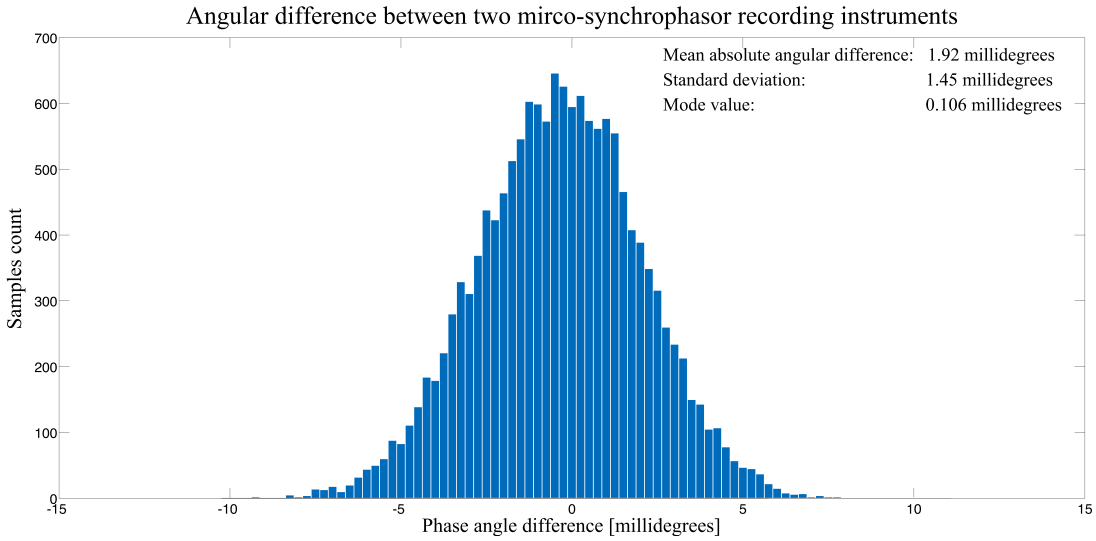

Figure 3-7: Histogram showing spread of measured phase angles

It is seen that the histogram has a normally distributed spread around 0°. A cumulative count of the recorded phase angle values categorised in intervals of 0.002° is shown in Table 3-5

Table 3-5: Cumulative count of the measured phase angle values

Distribution	Count	Cumulative Count	Percent [%]	Cumulative Percent[%]
-0.010 to -0.008	9	9	0.06	0.06
-0.008 to -0.006	130	139	0.87	0.93
-0.006 to -0.004	832.	971.	5.57	6.50
-0.004 to -0.002	2 689.	3 660.	17.99	24.48
-0.002 to 0.000	4 634.	8 294.	31.00	55.48
0.000 to 0.002	4 254.	12 548.	28.46	83.94
0.002 to 0.004	1 918.	14 466.	12.83	96.77
0.004 to 0.006	444.	14 910.	2.97	99.74
0.006 to 0.008	37.	14 947.	0.25	99.98
0.008 to 0.01	1.	14 948.	0.007	99.99
0.010 and Over	1.	14 949.	0.007	100

To evaluate the level of certainty in measurement, these recorded phase angle differences were statistically analysed with the results listed in Table 3-6:

Table 3-6: Statistical results of the micro-synchrophasor resolution tests

Parameter	Value
Center point of spread	0.00038°
Mean Absolute Angular Difference ($\|\overline{x}\|$)	0.00192°
Standard Deviation (σ_x)	0.00145°
Mode Value (M_0)	0.00011°
Frequency Distribution (f_x)	0.00516°

The statistical results indicate that the error in angular measurements has a normal spread around 0.00038°. This demonstrated a time-stamping asynchronism dispersion between the recorders of 21.11 ns.

An absolute mean phase angle difference of 0.00192° from 0° was calculated, which represents a time stamping uncertainty of 106.67 ns between the instruments. This complies within the maximum time error of 1 μs for synchrophasor measurements.

The standard deviation from 0° was calculated to be 0.00145°, with the most frequent angular difference recorded was 0.000106°.

These metrological results verified that the IEC 61000-4-30, ed. 3 Class A PQ instruments are be capable of micro-synchrophasor recordings, which can be implemented in distribution networks.

3.3 Micro-Synchrophasor Performance Verification with Impedance Measurements

Application of a reference impedance to practically verify the metrological performance of the micro-synchrophasor recorders have been performed. The intent was to demonstrate the viability of small angular detection capabilities of micro-synchrophasor recordings.

Measurements were conducted on a 0.485 km Aluminium (Aℓ) cross-linked polyethylene (XLPE) insulated 4×150 mm^2 distribution cable in a LV test network. The impedance was calculated from the synchronised voltage and current phasor recordings by means of using the two-port line current equation that has been derived in Chapter 2.

$$\boldsymbol{I}_R = \frac{\boldsymbol{V}_S - \boldsymbol{V}_R}{\boldsymbol{Z}} \tag{3.3}$$

By rearranging (3.3) and substituting the recorded data values into the parameters, the line impedance can be calculated:

$$\boldsymbol{Z} = \frac{\boldsymbol{V}_S - \boldsymbol{V}_R}{\boldsymbol{I}_R} \tag{3.4}$$

The resultant impedance values were verified afterwards by means of iterative recordings with an EN 60909-0 certified loop impedance measurement instrument. Micro-synchrophasor recordings were specifically made under LV conditions to generate small voltage phase angles across the line.

These tests, serving as supplementary verification, also provide validation on the practicality to use micro-synchrophasor measurements in distribution networks.

3.3.1 Laboratory Test Network

The LV line impedance measurements with micro-synchrophasor recorders were conducted at the University Ghent, Kortrijk campus on a distribution cable in a LV test network [24]. This test network emulates the conditions of a fully controllable residential network and is illustrated in Figure 3-8.

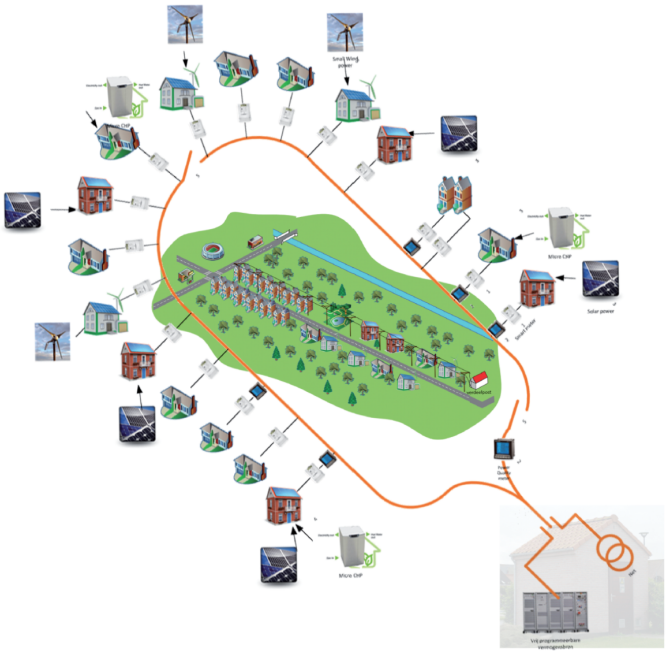

Figure 3-8: The LV test network (μ-grid) [24]

The entire length of 485 m of the main distribution cable was used for this test. Exact voltage levels from the residential transformer could be injected using an output voltage controller.

3.3.2 Micro-synchrophasor measurements

Measurements were conducted at both ends of the line, which was located at the output side of the distribution transformer and at the last feeder in the network.

Figure 3-9 indicates the concept of implementing micro-synchrophasor recorders at both ends of the distribution cable to measure time coherent data over the line.

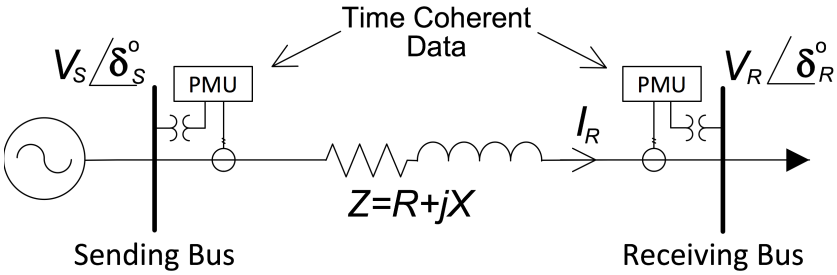

Figure 3-9: Measurements conducted over the length of the distribution line

During network operation the line impedance values are influenced by factors such as temperature, mutual inductance, cable loading and load type. For this reason, the certified loop impedance tester was used to measure the impedance value and to compare it with the micro-synchrophasor calculated line impedance.

Total of 10 000 synchrophasors were recorded to statistically evaluate the metrological performance of the recorders.

3.3.2.1 Voltage Recordings

The average recorded values of the three-phase sending ($\mathbf{V}_S$) and receiving ($\mathbf{V}_R$) end voltage phasors recorded are presented on a phasor diagram in Figure 3-10 to demonstrate the small phase angle difference was obtained in this experiment as expected from real-life micro-synchrophasors.

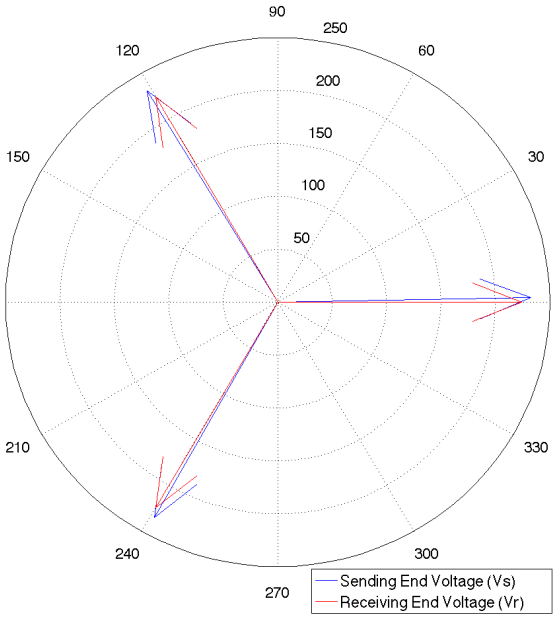

Figure 3-10: Three-phase sending and receiving end voltage phasors

The three-phase voltage phasors represent are perfectly symmetrical with phase shift between the sending- and receiving end due to the cable. On average over all of the synchrophasor recordings, the voltage rms values for each phasor at the sending and receiving end were 233.15 V and 232.26 V respectively.

The three-phase voltage recordings were converted to symmetrical components so a singular representation of the voltages could be obtained as shown in (3.5):

$$\begin{bmatrix} \mathbf{V}_0 \\ \mathbf{V}_1 \\ \mathbf{V}_2 \end{bmatrix} = \frac{1}{3}\begin{bmatrix} 1 & 1 & 1 \\ 1 & \mathbf{a} & \mathbf{a}^{-1} \\ 1 & \mathbf{a}^{-1} & \mathbf{a} \end{bmatrix}\begin{bmatrix} \mathbf{V}_A \\ \mathbf{V}_B \\ \mathbf{V}_C \end{bmatrix} \tag{3.5}$$

Where the symbol a denotes a complex number:

$$a = 1\angle 120^\circ = -\frac{1}{2} + \mathrm{j}\frac{\sqrt{3}}{2} \tag{3.6}$$

$\mathbf{V}_0$, $\mathbf{V}_1$ and $\mathbf{V}_2$ represent the zero, positive and negative voltage sequence components. Figure 3-11 illustrates the variance of the positive sequence voltages at the sending and receiving end obtained from 10 000 micro-synchrophasors.

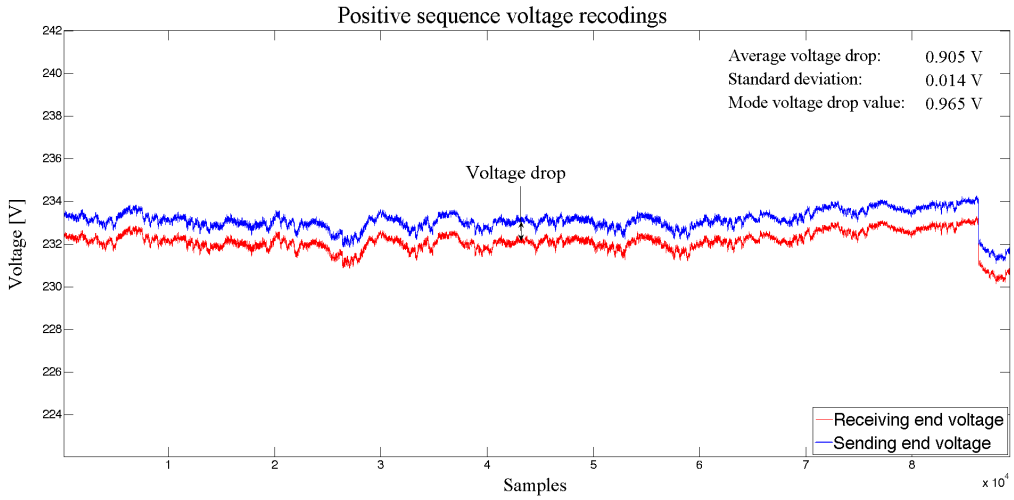

Figure 3-11: Positive sequence voltages at sending and receiving end

An average voltage drop of 0.905 V with a standard deviation of 0.014 V between $\mathbf{V}_S$ and $\mathbf{V}_R$ was recorded. The variance in the voltage phase angle across the line is presented in Figure 3-12.

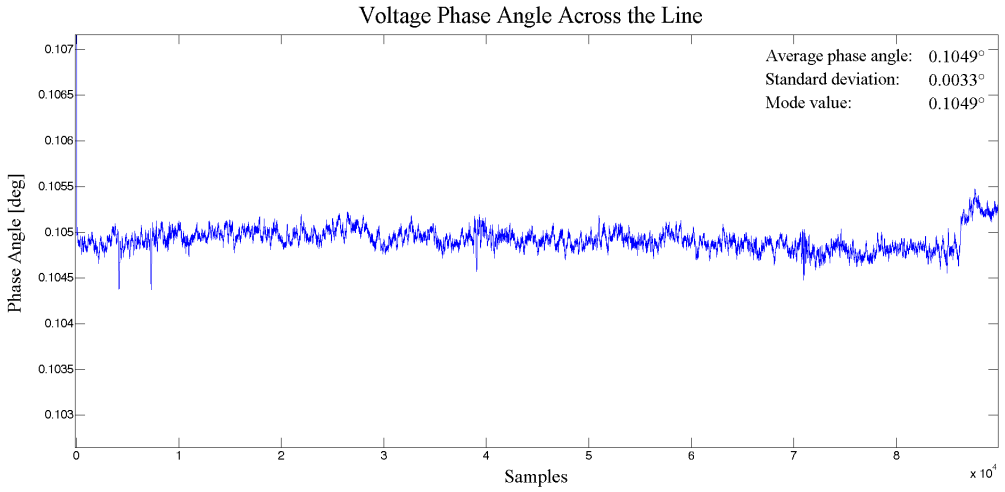

Figure 3-12: Recorded voltage phase angle over the line

An average phase angle across the line of 0.1049° was recorded with a standard deviation of 0.0033°. Since small angular values are recorded, it was important to avoid any rounding of decimal values. By representing the average recorded voltage magnitudes and phase angles as the nominal values, $\mathbf{V}_S$ and $\mathbf{V}_R$ are given as:

$$\boldsymbol{V}_S = 233.166\angle 0.1049^\circ \ V$$
$$\boldsymbol{V}_R = 232.261\angle 0.0000^\circ \ V$$

3.3.2.2 Current Recordings

According to the two-port network model, the sending and receiving end currents has to be equal, as shown in Figure 3-13.

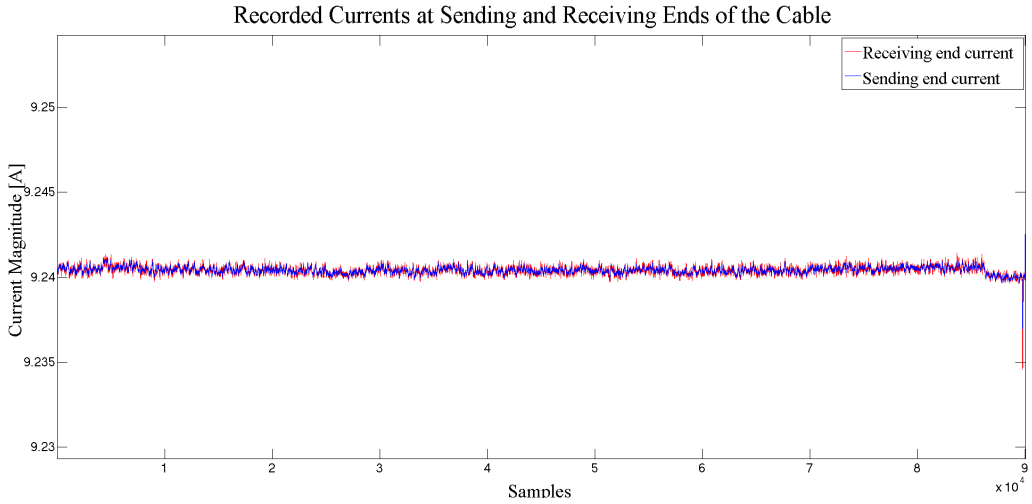

Figure 3-13: Recorded line current magnitude profiles

The sending and receiving end current magnitudes have an average value of 9.244 A. No detectable phase angle difference between the sending and receiving end current phasor occurred as shown in Figure 3-14 below.

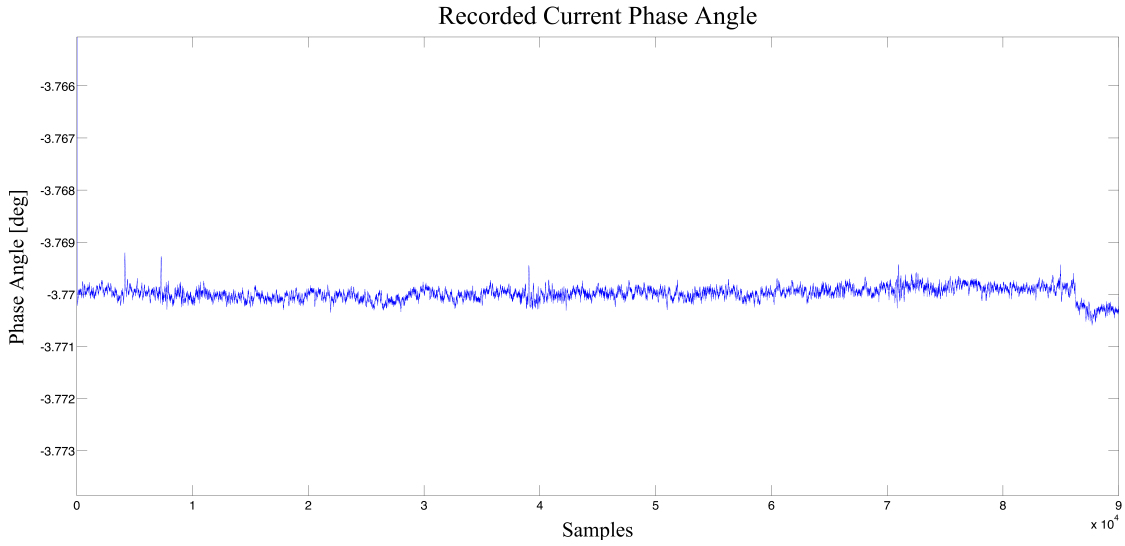

Figure 3-14: Recorded current phase angle profile

The current phase angles were measured on average as -3.769°. The negative phase angle indicates that the current lags the voltage by -3.769°.

$$\boldsymbol{I} = 9.244\angle -3.769^{\circ}\ A$$

3.3.2.3 Line Impedance based on Micro-Synchrophasor Recordings

The line impedance was calculated using micro-synchrophasor recordings in the equation (3.4). The line impedance of the distribution cable is shown in Figure 3-15.

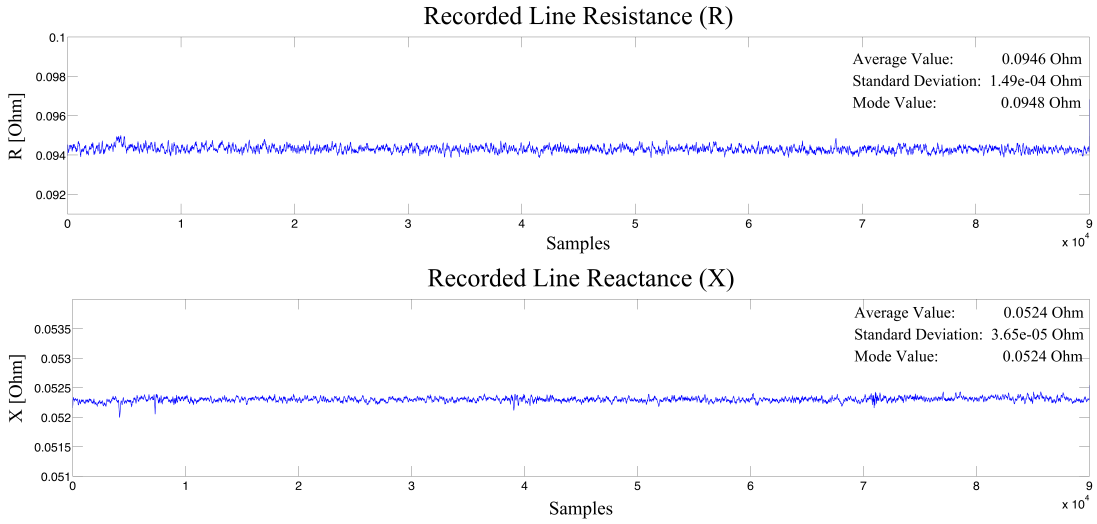

Figure 3-15: Line parameter resistance (top) and reactance (bottom) recording profiles

The average recorded resistance is $R_{\text{avg}} = 94.71$ mΩ and average reactance, $X_{\text{avg}} = 52.44$ mΩ. Mode values were calculated as $R_{\text{mode}} = 94.69$ mΩ and X_{mode} 52.40 mΩ, which correlate well with the average impedance parameters. The average calculated values represented a nominal line impedance of:

$$\boldsymbol{Z} = R + X_L = 94.71 + j52.44 \ m\Omega$$

The characteristic line impedance per kilometer (km) was subsequently calculated as:

$$z_\ell = 195.28 + j108.13 \ m\Omega/km$$

3.3.2.4 Line Impedance measured with Certified Impedance Tester

The line impedance recorded by the EN 60909-0 certified loop impedance tester are used as benchmark. These values were obtained by means of conducting line-to-line and line-to-neutral loop impedance measurements.The line-to-line impedances, denoted Z_{12}, Z_{23} and Z_{31} are presented as the sum of the lines over which the measurements are conducted:

$$\begin{aligned} Z_{12} &= Z_1 + Z_2 \\ Z_{23} &= Z_2 + Z_3 \\ Z_{31} &= Z_3 + Z_1 \end{aligned} \tag{3.7}$$

The line impedances are subsequently obtained through the impedance matrix, shown in (3.8):

$$\begin{bmatrix} Z_1 \\ Z_2 \\ Z_3 \end{bmatrix} = \begin{bmatrix} Z_{12} & -Z_{23} & Z_{31} \\ Z_{12} & Z_{23} & -Z_{31} \\ -Z_{12} & Z_{23} & Z_{31} \end{bmatrix} \tag{3.8}$$

On a similar basis, the line impedances can be calculated through phase-to-neutral line impedance measurements:

$$\begin{bmatrix} Z_1 \\ Z_2 \\ Z_3 \end{bmatrix} = \begin{bmatrix} Z_{1N} & -Z_{2N} & Z_{3N} \\ Z_{1N} & Z_{2N} & -Z_{3N} \\ -Z_{1N} & Z_{2N} & Z_{3N} \end{bmatrix} \tag{3.9}$$

Comparison of the line impedances obtained from line-to-line and line-to-neutral measurements are presented in Table 3-7.

Table 3-7: Distribution cable online calculated impedance from loop measurements

	Line-to-Line Measured Values	**Line-to-Neutral Measured Values**
Line Impedance	**Value (mΩ)**	**Value (mΩ)**
$\mathbf{Z}_a$	96.27 + j53.36	96.44 + j53.38
$\mathbf{Z}_b$	96.32 + j53.29	96.17 + j53.36
$\mathbf{Z}_c$	96.25 + j53.37	96.29 + j53.42
Average Impedance	96.28 + j53.34	96.30 + j53.39
Standard Deviation	0.036 + j 0.045	0.135 + j0.0310

The intent of using both line-to-line and line-to-neutral measurements was to determine the line impedances with the highest certainty in measurement. Based on the standard deviations, it can be seen that the line-to-line impedances provided a higher certainty in measurement.

The average line impedance value from all loop measurement results were calculated as:

$$Z_{ref} = 96.29 + j53.36 \ m\Omega$$

By dividing the cable line impedance with the cable length of 0.485 km the average line parameters for the test duration are given below.

$$z_\ell = 198.54 + 110.02 \ m\Omega/km$$

3.3.2.5 Verifying the Micro-Synchrophasor Line Impedance Measurements

The average line impedance calculated with micro-synchrophasor data was compared to the value measured with the certified loop impedance meter. This provided a practical verification on the micro-synchrophasor recorders' metrological accuracy.

The average line impedance calculated by micro-synchrophasor recordings:

$$\boldsymbol{Z} = R + X_L = 94.71 + j52.44 \ m\Omega$$

The line impedance measured by the loop impedance tester:

$$\boldsymbol{Z}_{ref} = 96.29 + j53.36 \ m\Omega$$

These line impedances have a difference of 1.58 + j0.95 mΩ. The line impedances are compared in phasor format below:

Table 3-8: Comparison of results obtained by micro-synchrophasors and impedance tester

Line impedance calculated with micro-synchrophasor [mΩ]	**Line impedance measured with 6090-0 impedance analyser [mΩ]**
108.26∠28.98°	110.08∠29.00°

A difference of 1.82∠0.02° mΩ was found. The micro-synchrophasor calculated impedances were within 1.65% of the measured values. In Appendix B, the detail and calibration information of the EN 6090-0 loop impedance tester is reported.

3.4 Conclusion

Metrological capabilities of micro-synchrophasor recordings conducted with the IEC 61000-4-30 Class A ed. 3 PQ instruments were verified by means of conducting tests on the accuracy and uncertainty in measurement. Two micro-synchrophasors recording instruments, each with its own GPS unit, were used to measure 50 Hz signals generated by an Omicron CMC 256plus™ high precision signal generator.

Phase angle shifts from 5° down to 0.01° between the two signals were recorded to verify the accuracy of the micro-synchrophasor instruments. Results were compared afterwards with the proposed requirements in [19] to verify the recorders to be capable of micro-synchrophasor level measurements.

Statistical analysis showed that the results satisfied these requirements, since each angular recording was in a close proximity to the generated values and complied with the 1% TVE criteria for synchrophasor measurements [12].

To verify the certainty in micro-synchrophasor measurements the recorders simultaneously measured an identical 120 V, 5 A 50 Hz signal. Ideally, the micro-synchrophasors would report a zero phase angle difference between the recordings. Any reported deviation from a 0° phase angle difference illustrated the error in the micro-synchrophasor measurements.

Using a histogram, the results represented a normal spread around 0.00038°, which verified the micro-synchrophasor recordings to have a normalised error in synchronous time sampling of 19.83 ns. A mean absolute angular difference of 0.00192° between the measurements was calculated, signifying a 0.107 μs time uncertainty. It is worth noting that no other instrument is known to have reported a better resolution at this time.

The second verification study was conducted in a LV test network to substantiate the instruments' practical metrological capabilities. Tests were performed by measuring a known impedance of a 485 m LV distribution cable. A series of micro-synchrophasor recordings were conducted such that the average line impedance could be statistically calculated.

The results were compared to impedances measured by a high precision EN 6090-0 certified loop impedance meter. Comparison presented a phasor deviation of $1.82\angle 0.02°$ (1.65%). This provided verification on the practical metrological capabilities for micro-synchrophasor measurements.

The tests done in this chapter subsequently verified the IEC 61000-4-30 Class A ed. 3 PQ instruments to comprise sufficient metrological accuracies for micro-synchrophasor level recordings. The practical verification also facilitated validation on the viability of micro-synchrophasor phase angle detection capabilities for field studies in distribution networks.

Chapter 4:
Stability Impacts of Renewable Power Plants on Distribution Networks

4.1 Introduction

Traditionally, distribution networks required limited monitoring as network stability could be fully contained at transmission level. However, the addition of distributed sources, mostly in the form of renewable energy, has increased the complexity of distribution network operation. This introduced similar concerns over distribution network stability than what was known in transmission systems.

Synchrophasor technology is well developed to supervise and control the stability of transmission systems. This made the prospect of applying synchrophasors for distribution network monitoring attractive. Micro-synchrophasors are anticipated to present similar supervision capabilities over distribution systems.

Prior to the field application of micro-synchrophasors, a conceptual study on the stability impacts of RPPs on sub-transmission networks have been investigated in this chapter.

In the first section the theoretical concepts over the impact on steady-state and voltage stability due to an additional power source were evaluated. The effects were studied on power-transfer and P-V curves to present the opportunity of stability visualisation in distribution systems.

The following section presented a simulation study done in Matlab Simulink® where a modelled 75 MW PV power plant was integrated into a sub-transmission network. The chapter is concluded by the analysis of a published real-life case study [43] on the stability impacts of widespread PV integration, which also substantiated the results of the simulation study.

4.2 Impact of a distributed energy source on stability

Distributed sources of renewable can pose both detrimental and beneficial effects to a distribution system. Overvoltage, transients and unpredictability of output power are known concerns of renewable energy sources.

Beneficial effects such as increased system loading capabilities, undervoltage mitigation and improved network security by reducing downstream load stresses can also be attributed by renewable energy sources [38], [29]. The impact on steady-state and voltage stability of due to an integrated distributed source have been investigated.

These effects are quantified on power-transfer and P-V curves to illustrate the concept and features of visual stability tracking on a distribution system with integrated distributed sources of renewable energy.

Consider a conventional bus with a single utility power source:

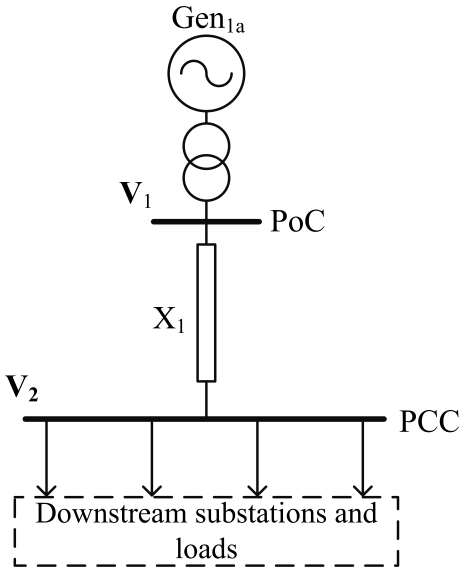

Figure 4-1: An network bus (PCC) with a single incoming supply

The maximum active power that can be transferred from the PoC to the PCC is:

$$P_{max} = \frac{V_1 V_2}{X_1} \tag{4.1}$$

With the maximum active power capacity at the PCC given as:

$$P_{PCC} = V_2 I \cos(\theta) \tag{4.2}$$

An additional secondary source of energy such as a PV plant can be added, shown in (Figure 4-2), it will increase the power that can be transferred to the PCC.

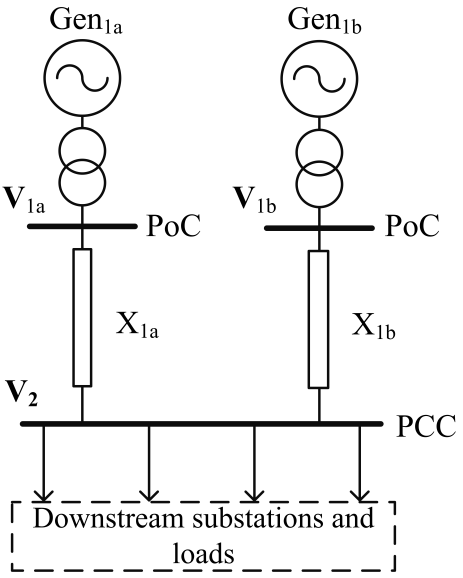

Figure 4-2: Additional generation supply added to the PCC bus

When the renewable energy source comes into production and injects power in a fairly constant manner into the PCC, the system is stabilised and results in extra available load capacity. If it is assumed that the renewable source, Gen_{1b}, has the same generation capacity and impedance as Gen1a, then the following conditions are valid:

$$V_{1a} \parallel V_{1b}$$
$$\therefore V_1 = V_{1a} = V_{1b}$$

$$X_{1a} \parallel X_{1b}$$
$$\therefore X_1 = \left(\frac{1}{X_{1a}} + \frac{1}{X_{1b}}\right)^{-1} = \frac{X_1}{2}$$

$$I = I_{PCC} = I_{1a} + I_{1b} = 2 \times I$$

The maximum power that can be transferred is now :

$$P_{max(new)} = 2 \times \frac{V_1 V_2}{X_1} \tag{4.3}$$

The active power available to the PCC is now doubled:

$$P_{PCC(new)} = 2 \times V_2 I \cos(\theta) \tag{4.4}$$

The increased active power availability will subsequently increase the steady-state and voltage stability limits, as shown in Figures 4-3 and 4-4.

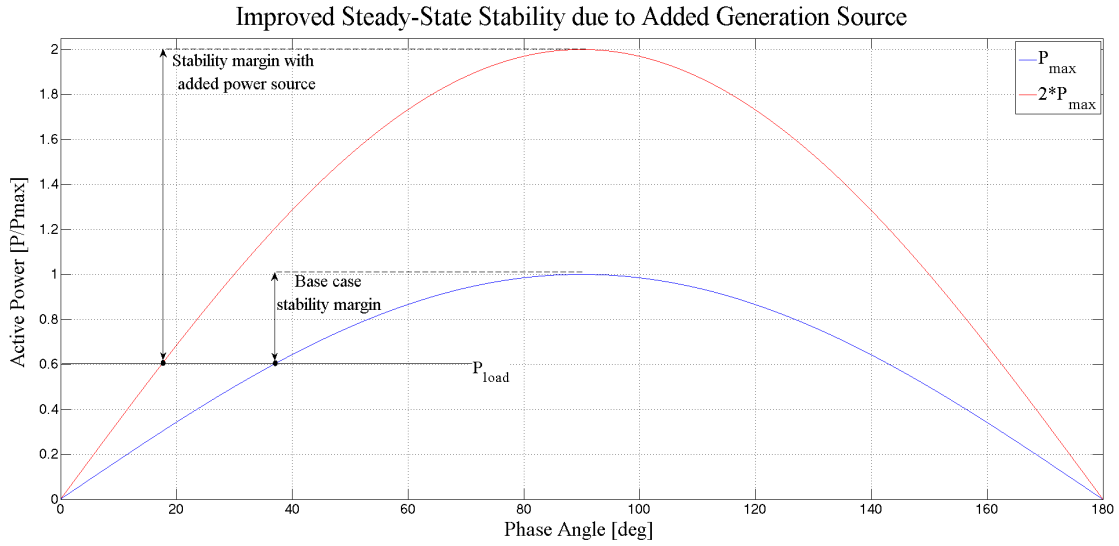

Figure 4-3: Improved steady-state stability

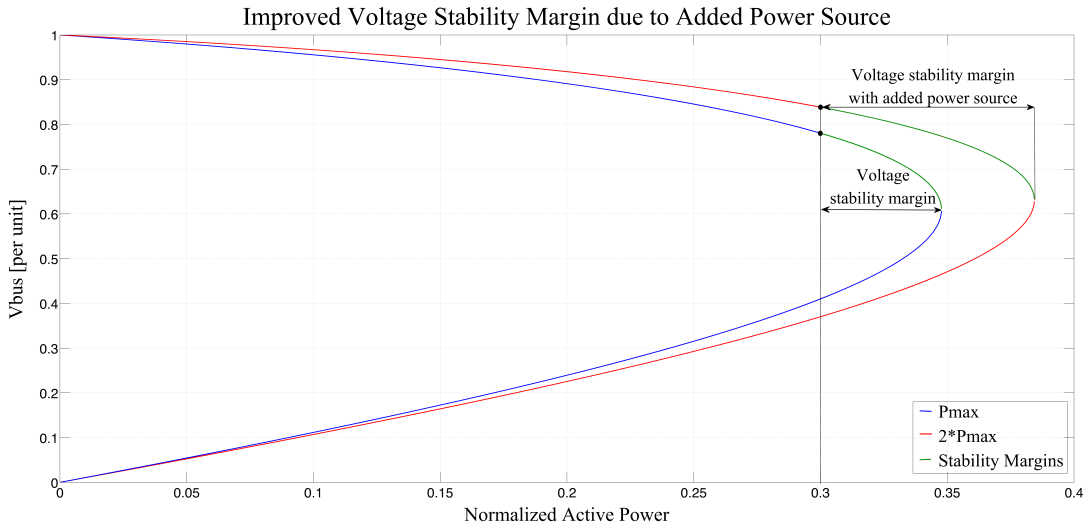

Figure 4-4: Improved voltage stability margin

The addition of a distributed renewable energy source has increased the maximum stability points, which improved the stability margins. However, renewable energy is variable in principle and unpredictable to some extent. If the generation output suddenly changed due to variable conditions these improved stability margins can become compromised.

4.3 Modelling and simulation analysis

4.3.1 Simulation model

A simulation study was conducted to analyse the predicted impact of a PV power plant integrated onto a local network. The system modelled in Simulink® comprised a 7-bus test system, derived from the IEEE 9 bus test network guidelines.

A 75 MW PV power plant consisting of 4 parallel plant sections (18.75 MW per section) was simulated to integrate with the network at 132 kV. The system parameters are configured for high power consumption by a constant RL-load. Further details surrounding the simulated PV power plant sub-level models are given in Appendix C.

Figure 4-5 presents the system as modelled in Simulink®.

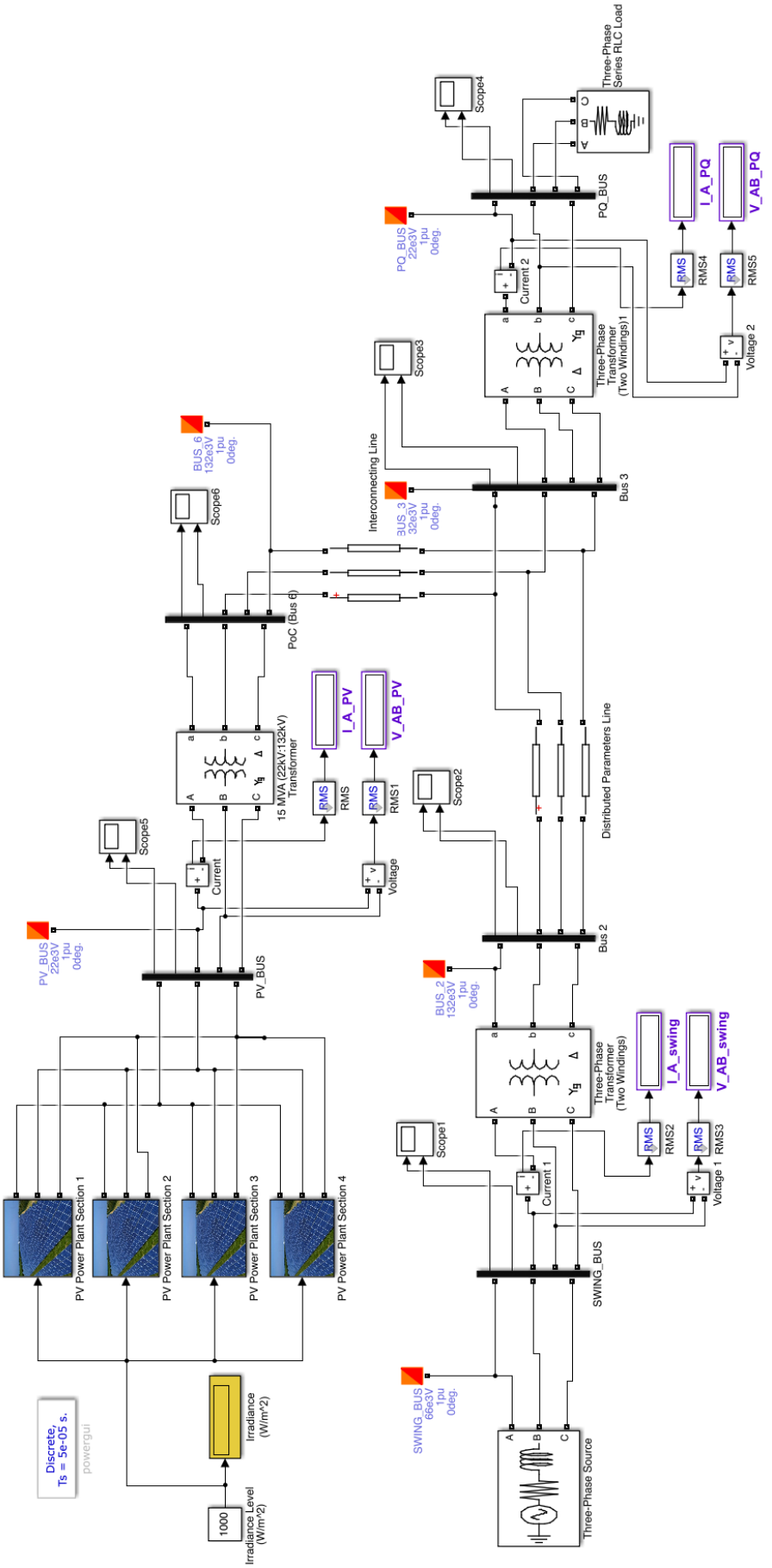

Figure 4-5: Simulink® model of a 75 MW PV plant integrated with a network

A load flow study with the Newton-Raphson algorithm of 500 iterations has been conducted to evaluate the effects of PV plant integration at the PCC. A balanced 3-phase RL-load downstream of the line is predominantly supplied by the utility generator (infinite bus). The PV plant is synchronised at the PCC.

The PV power plant is defined as a PV bus and the network load as a PQ bus for the load flow analysis. These parameters are listed in Table 4-1.

Table 4-1: Voltage and power parameters of the three bus types in the test system

Bus Type	**Component**	**Nominal Voltage**	**Rated Power**
Swing	Utility Generator	66 kV	250 MVA
PV	DG Source	22 kV	75 MW (unity PF)
PQ	RL-Load	22 kV	125 MVA (Balanced)

The PCC bus where the PV plant connects to the utility is located at Bus 3 of the model. The 75 MW PV power plant has been systematically simulated under increasing levels of irradiance until full power capacity was reached at 1000 W/m^2.

Solar irradiance, modelled as a numerical step value to the 4 paralleled sections of the PV plant, was the only variable used to change the output of the PV arrays. The other elements are kept constant at standard test conditions [40] during the course of the simulation:

Table 4-2: Values of test elements during simulations

Parameter	**Value**
Irradiance [W/m^2]	0-1000
PV cell temperature [°C]	25
Air Mass [A.M]	1.5

The PV module characteristics under STC are given as:

Table 4-3: Rated Kyocera® PV module characteristics under STC

Module Parameters	**Rating**
Maximum Power (P_{max})	205 W
Voltage at Maximum Power (V_{mp})	26.6 V
Current at Maximum Power (I_{mp})	7.71 A
Open-Circuit Voltage (V_{oc})	33.2 V
Short-Circuit Current (I_{sc})	8.36 A

A 100 km line connects the PV plant PoC with the PCC bus. An equivalent-pi transmission line model is used, with line capacitance neglected due to its short distance. The line parameters of the model are given in Table 4-4.

Table 4-4: Test model line parameters per phase

Line	Description	Length	Line Impedance		
			R (Ω/km)	L (H/km)	C (F/km)
1	Utility Supply Line	100 km	0.4 Ω/km	1.3 mH/km	7.47 nF/km
2	Interconnecting RPP Line	100 km	0.2 Ω/km	0.9 mH/km	1.2 nF/km

Three transformers were included in the Simulink® model. Two step-up transformers inject the PV power into the 132 kV line. One step-down transformer supply a network load located at the PQ bus. The transformer parameters of the simulated model are given in Table 4-5.

Table 4-5: Transformers parameters simulated in the test system

Transformer Bus	Voltage Rating	Rated Power	Transformer Impedance
Swing	6.6 kV/132 kV	300 MVA	8 %
PV	25 kV/132 kV	250 MVA	8 %
PQ	132 kV/22 kV	300 MVA	5 %

4.3.2 Simulation of steady-state stability

The steady-state interaction of the PV plant is observed when increasing irradiance levels in the simulation model. A base power value of 250 MVA is used, since it represents the rated power of the transformer at the PoC

The base voltage values are selected as the rated voltages at each bus. Table 4-6 presents the base values chosen at each bus:

Table 4-6: Base values used in the system simulations

Bus Number	Base Power	Base Voltage	Base Impedance
1 (Swing)	250 MVA	66 kV	17.43 Ω
2	250 MVA	132 kV	69.7 Ω
3 (PCC)	250 MVA	132 kV	69.7 Ω
4 (PQ)	250 MVA	25 kV	2.50 Ω
5 (PV)	250 MVA	22 kV	1.94 Ω
6	250 MVA	132 kV	69.7 Ω

The PV power plant can generate power up to 75 MW. The grid-tied PV array inverters are configured to maintain a power factor near unity. In respect to the base power of 250 MVA, the PV plant can inject under ideal ambient conditions (1000 W/m^2) a maximum of 0.3 p.u. power.

The goal was to evaluate the stability impact of increasing levels of PV production on the network. PV network integration was increased at 5% intervals by systematically raising the irradiance from 0 to 1000 W/m^2. At each increment the steady-state and voltage stability as function of PV generation has been evaluated.

The active power, voltage magnitude and phase angle between the reference (swing) bus and the PCC (bus 3) were evaluated during the simulations. Table 4-7 presents the results under steady-state conditions.

Table 4-7: Results of Bus 3: varying irradiance levels

Network Integration Level (%)	**Bus 3 Voltage (per unit)**	**Phase Angle ($\delta°$)**	**Steady State Active Power (P_{bus3}/P_{max})**
0	0.870	30.01	0.501
5	0.911	23.61	0.400
10	0.916	19.72	0.337
15	0.923	15.89	0.274
20	0.943	12.55	0.217
25	0.949	9.70	0.168
30	0.965	6.86	0.120

It is seen in Table 4-7 that the P_{bus3}/P_{max} relation is reduced as PV production increased. A reduction in the phase angle values between the swing bus and the PCC can also be seen as PV power injection increases. Figure 4-6 visualise the steady-state power transfer between the swing bus and the PCC.

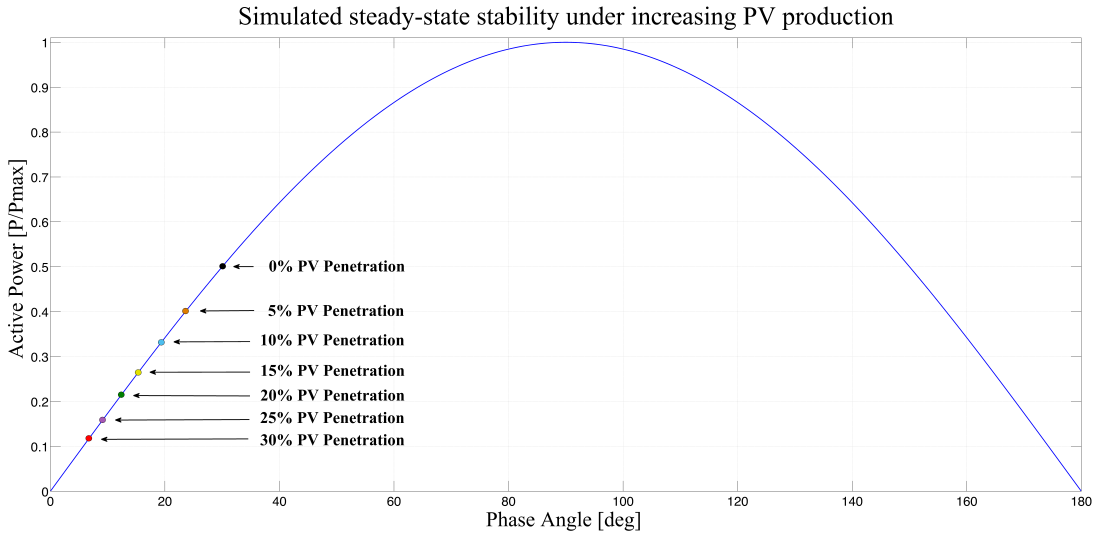

Figure 4-6: The reduction in phase angle between the PoC and the PCC due to PV generation

A decrease in the steady-state power supplied by the utility at the PCC is evident as PV power generation increases. Steady-state active power consumption at the PCC is at 50%

of the maximum transferable active power when no PV power is present.

During full PV production the steady-state power supplied by the utility at the PCC is reduced to 12%, indicting that the utility supplied 76% less energy to the PCC.

These results demonstrated that integration of a large-scale PV power plant can be considered as a reduction in the load demand, since the generation from the utility has been decreased. It is therefore postulated that, regardless of the location on the line, the stead-state stability was improved since loading are effectively reduced.

4.3.3 Simulation of voltage stability

Loading was kept fixed at 112.4 MVA and the power factor at 0.91. Improvement on voltage stability and active power margin due to additional generation available from the PV plant is demonstrated on the P-V curves in Figure 4-7.

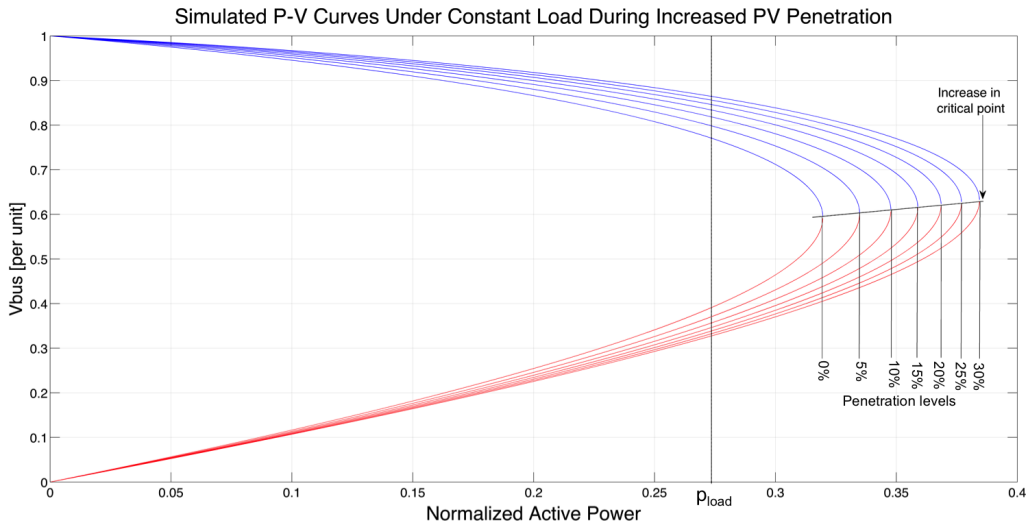

Figure 4-7: P-V curves depicting how the increasing PV generation improves voltage stability

As the PV plant injected more power, the critical point is increased, resulting in more stable voltage conditions. The active power stability margin improved by 6.49% as the PV plant increased from 0 - 75 MW. The simulation results are summarised in Table 4-8.

Table 4-8: Stability improvement results displayed in Figure 4-7

PV Integration (%)	PV Production (MW)	Power Factor	Critical Instability Point (curve nose)	Active Power Margin
0	0	0.910	0.3196	0.0470
5	12.5	0.925	0.3348	0.0622
10	25	0.938	0.3477	0.0751
15	37.5	0.947	0.3589	0.0863
20	50	0.955	0.3685	0.0959
25	62.5	0.961	0.3769	0.1043
30	75	0.967	0.3845	0.1119

It may prove difficult to simultaneously assess the voltage stability on several P-V curves since the critical point of each curve will differ. This can be addressed by generating a locus of the active power stability margin for each measurement.

This is demonstrated in Figure 4-8. The profile displays the active power stability margin as a function of the injected PV power. A 0% threshold indicates that no margin remains and the critical point of instability has been reached.

Such a graph is presented in Figure 4-8 and displays the active power stability margin as a function of the injected PV power. The 0% threshold indicates that no margin remains and the critical point of instability has been reached.

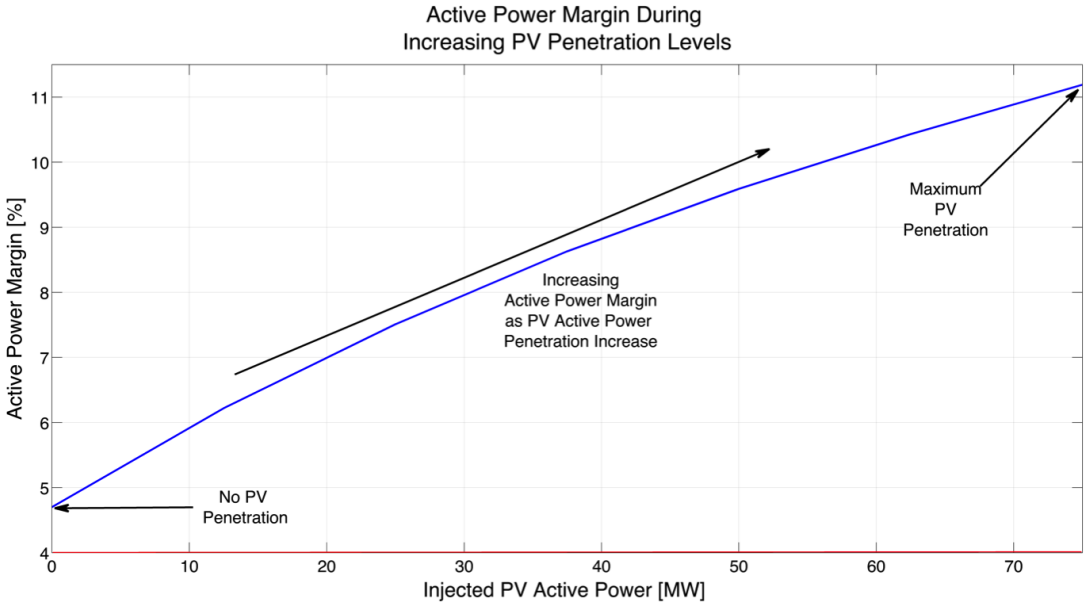

Figure 4-8: Active power margin locus as PV plant power production is increased

It is seen in Figure 4-8 that the active power stability margin improves nearly linearly with PV generation. In the case where continuous assessment is done, the active power margin locus can be displayed as a function over time.

This will particularly be useful in evaluating the voltage stability over a full (daily) production period of a PV power plant. Values on the profile could then be cross-referenced with the PV generating levels to analyse the impact of the PV plant.

4.4 Case study: the impact of large-scale PV generation on real-life power system

4.4.1 Case study overview

The results from the simulation demonstrating network stability being improved due to the integration of a PV power plant are facilitated by studying a reference case study on stability effects of large-scale PV plants integrating on a real-life power system.

In this case-study, stability impacts on the Bangladesh national grid due to widespread large-scale PV plant integration were published [43], [44].

4.4.2 Stability impacts on distribution network buses with large-scale PV integration

Three distribution network sections with large integrated PV power were studied. These sections contain parallel buses with equal PV capacity installed on each bus.

Cox region bus system
The first bus section under study has two parallel buses, shown in Figure 4-9.

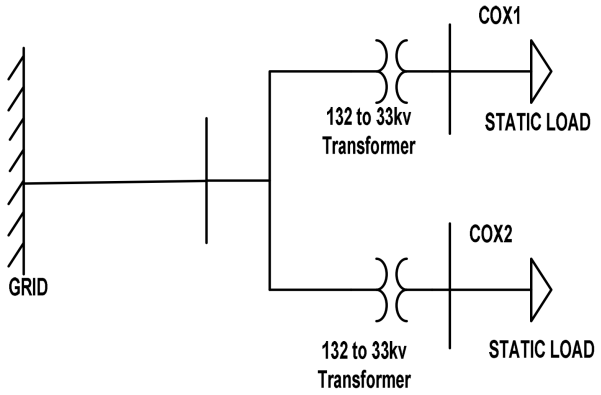

Figure 4-9: The Cox bus system [43]

Voltage stability at the Cox_1 and Cox_2 buses is improved with high levels of PV generation. PV generation were studied at 0%, 50% and 100% and are presented in Figure 4-10.

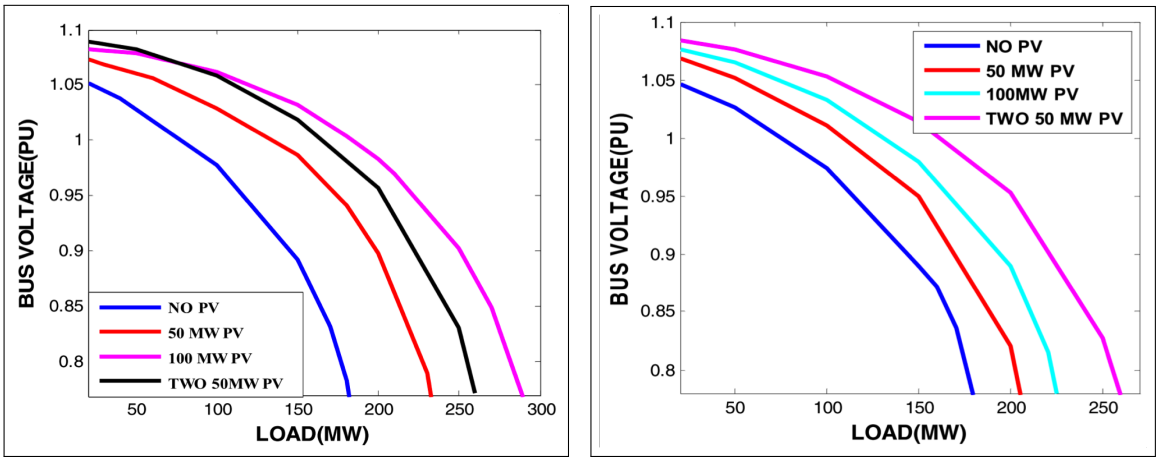

(a) P-V curve stable region of Cox_1 (b) P-V curve stable region of Cox_2

Figure 4-10: Effect of increased PV capacity on the load margin of Cox_1 and Cox_2 [43]

Comillan region bus system

The next study was done on a larger two-bus configuration with the same nominal voltage magnitude. The diagram for the Comillan bus configuration is presented below in Figure 4-11.

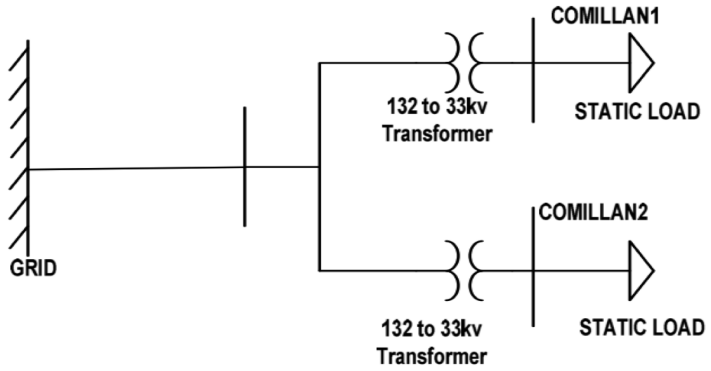

Figure 4-11: The Comillan bus system [43]

The voltage stability is also improved as PV generation increased. Results in Figure 4-12 demonstrates the stability margin on $Comillan_1$ and $Comillan_2$ are highest during PV production:

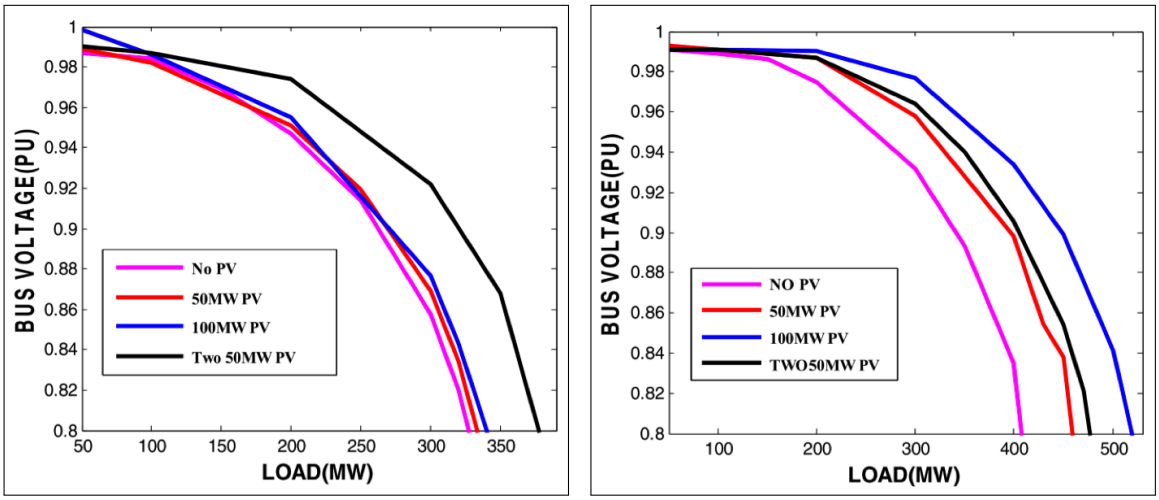

(a) P-V curve stable region of Comillan$_1$ (b) P-V curve stable region of Comillan$_2$

Figure 4-12: Effect of increased PV capacity on the load margin of Comillan$_1$ and Comillan$_2$ [43]

Jamalpur region bus system

The third observation was done on the Jamalpur bus system that has three parallel buses. Figure 4-13 presents the single line diagram.

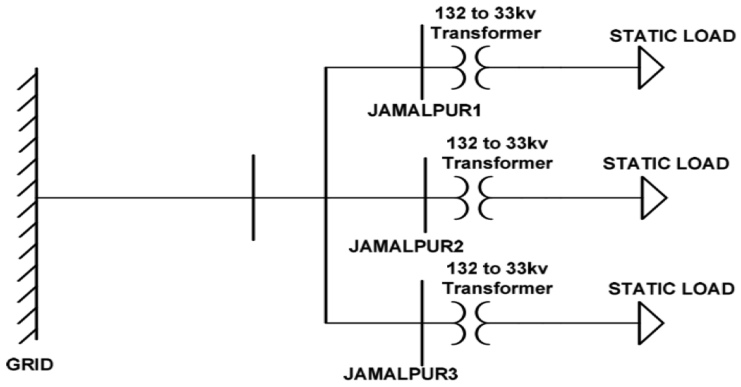

Figure 4-13: The Jamalpur bus system [43]

Jamalpur buses 2 and 3 contain undervoltage conditions, which put the downstream loads at risk for voltage collapse. Figure 4-14 demonstrates how PV integration resolved this issue.

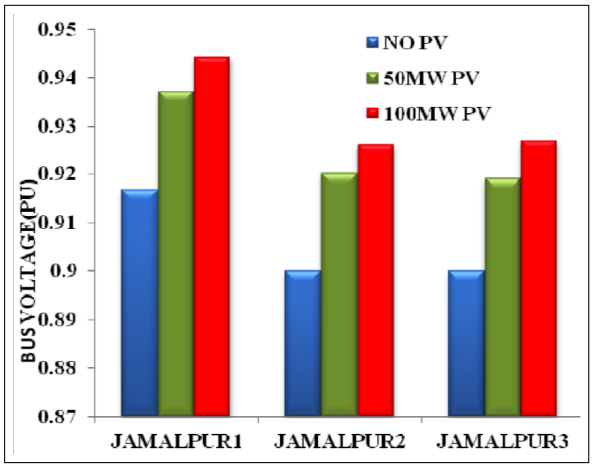

Figure 4-14: Improved effects on the Jamalpur buses with increasing PV power [43]

This case study demonstrated how large-scale PV plants voltage stability on the Bangladesh power system. An interesting study of the under-voltage problem at the Jamalpur buses were shown to be facilitated by the injection of PV power.

This presents a practical example on the means that overvoltage levels associated with PV integration can be managed to benefit network resiliency. The results substantiate the findings in the simulation study, where it was shown that the added active power generation improves network stability.

4.5 Conclusion

This chapter studied the conceptual impacts of a distributed renewable energy source on network steady-state and voltage stability. The impacts were investigated by means of a conceptual study, simulations and a reference case study to support results from the simulations.

The conceptual study investigated the impacts of an added RPP that have an equal generation capacity to the utility supply. Improvements of the RPP on steady-state and voltage stability were demonstrated on power-transfer and P-V curves to facilitate the concept of visual stability analysis.

A 75 MW PV power plant integrated with the utility at 132 kV was modelled and simulated in Simulink®. The system parameters were intentionally modelled to imitate similar conditions to the empirical field study presented in the next chapter.

The simulated PV generation was systematically increased to evaluate the impacts on steady-state and voltage stability at different integration levels. Results from the simulations were visually presented on power-transfer and P-V curves, which are the proposed platforms for visual stability analysis with micro-synchrophasors.

It was found that the voltage phase angle decreased in response to the PV generation increasing from 0 to 100%. This improved the steady-state δ-P relation. Similarly, voltage stability has also been improved since the injected PV production decreased the load demand on the utility generation. As a result, the simulations demonstrated that steady-state and voltage stabilities would be improved since the added PV power capacity reduces downstream load stresses.

The reference case study investigated to support the simulated results presented all three bus systems to benefit from improved voltage stability during maximum PV production. This case study showed that the integration of PV power plants improved voltage resiliency on the Bangladesh power system.

Results from this chapter, particularly pertaining to the simulation studies, indicated that large-scale PV integration comprise strong characteristics to improve stability and reduce the susceptibility of voltage instabilities. In the following chapter micro-synchrophasor field recordings are applied on a 75 MW PV power plant to investigate its interaction with the local grid.

Chapter 5:
Field Application of Micro-Synchrophasors

5.1 Introduction

This chapter analyse empirical field data of micro-synchrophasors recorded at a large-scale PV power plant integrated into a distribution network.

This chapter present the results of analysing micro-synchrophasors recorded at the PoC of a 75 MW PV power plant and the 132 kV upstream PCC. The PoC is connected to the PCC by a 100 km overhead 132 kV distribution line, as shown in the single-line diagram in Figure 5-1.

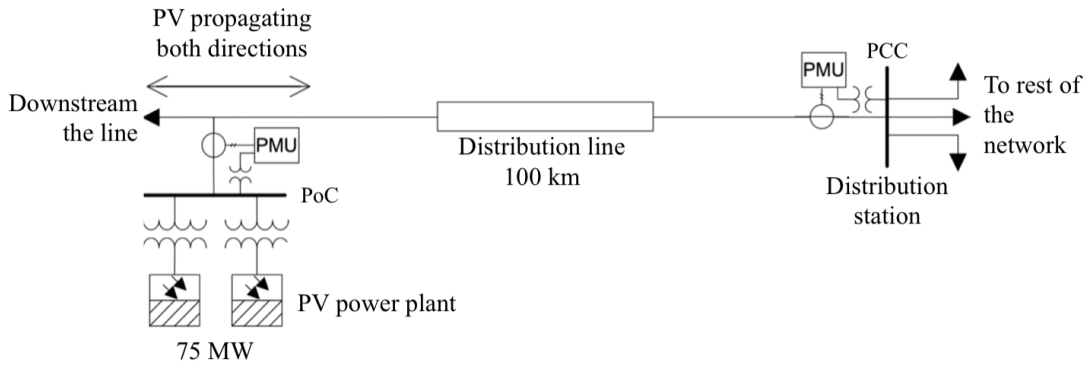

Figure 5-1: 75 MW PV plant integrated with a 132 kV distribution system

Analysis of micro-synchrophasor data is based on a 24-hour recording period, representing a typical daily PV production cycle.

The steady-state and voltage stability of this system is visualised on power-transfer and P-V curves. A proposal is made to chronologically track the locus of the VSM such that the stability behaviour over the full production cycle can be evaluated.

The output of the PV arrays are concentrated in to a 22 kV system, which injects energy into the 132 kV PoC by means of two parallel 50 MVA transformers. Micro-synchrophasor recordings are conducted at the PoC and PCC. The 100 km sub-transmission line supplies downstream loads from the regional distribution station (PCC).

This chapter aims to validate the usefulness of micro-synchrophasors to better understand the stability phenomena in sub-transmission networks with integrated RPPs (such as PV energy).

5.2 Steady-state analysis of micro-synchrophasor recordings

The voltage, current, power and phase angle profiles between the PoC and PCC are analysed to study the behaviour between the PV plant and sub-transmission network. A total of 86 400 micro-synchrophasors between the PoC and PCC was recorded.

Figure 5-2 presents the 3-phase voltage profiles recorded with micro-synchrophasors.

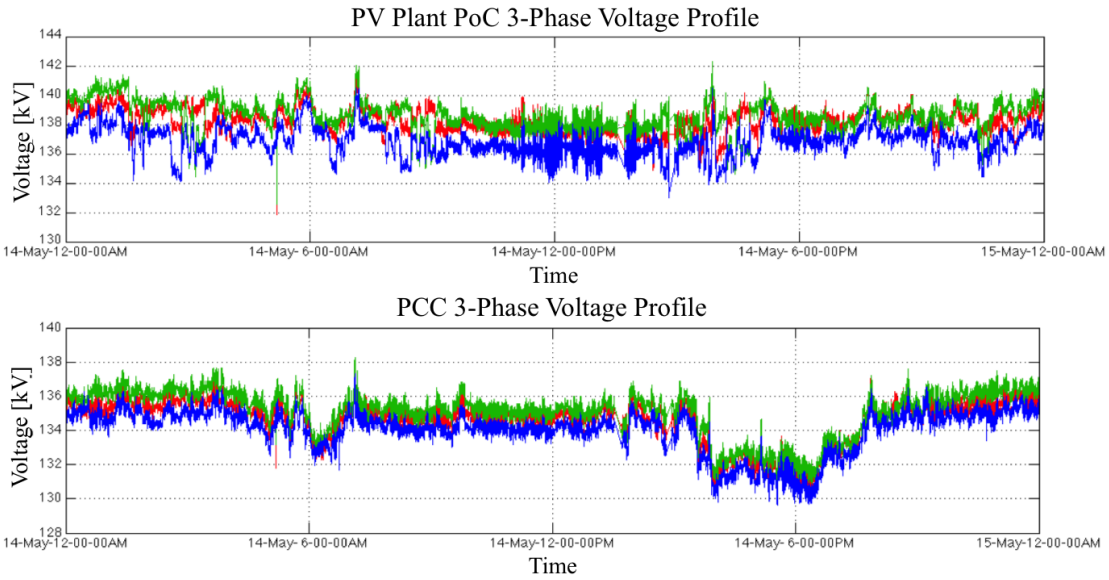

Figure 5-2: Micro-synchrophasor recorded three-phase voltage recordings at PoC and PCC

The three-phase voltage profiles are condensed by the over the given timespan. If the phase voltages are considered in the sequence domain, the positive sequence fundamental frequency voltages would enable a simplified comparison, as shown in Figure 5-3.

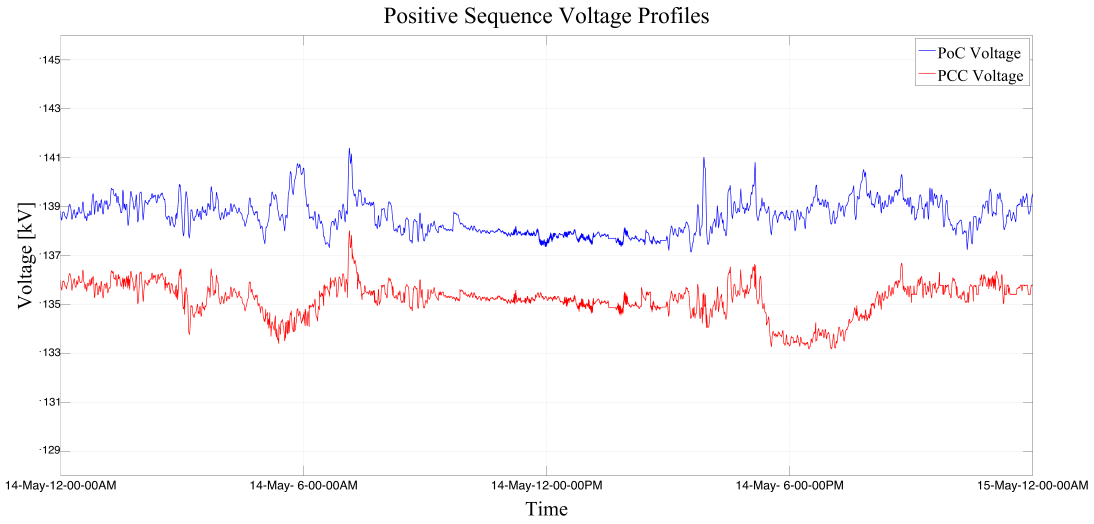

Figure 5-3: Trends of positive sequence voltages at PoC and PCC

The voltage profile of the PV power plant is specifically designed to compensate for a voltage drop over the rest of the interconnecting line leading up to the PCC.

The contribution of the PV plant's energy stabilises the voltage at the PCC during the day. When the PV plant is not producing energy the PCC voltage profile has a higher level of fluctuation.

A notable PCC voltage reduction during peak loading times is noted on the PCC. This shows that the PCC has a higher voltage susceptibility when the PV plant is not injecting energy.

The voltage profiles during PV production maintained a more constant levels, which are due to voltage volatility over the line being alleviated by an added voltage source closer to the downstream loads.

The synchrophasor currents at the PCC and at the PoC are shown in Figure 5-4. Current at the PCC recognises the contribution of the PV plant but also reflect the loads located downstream from the PoC.

The CTs at the PoC reflect all of the current from the PV plant into the PoC and the CTs at the PCC reflects only the current in the 132 kV line that terminate into the PCC.

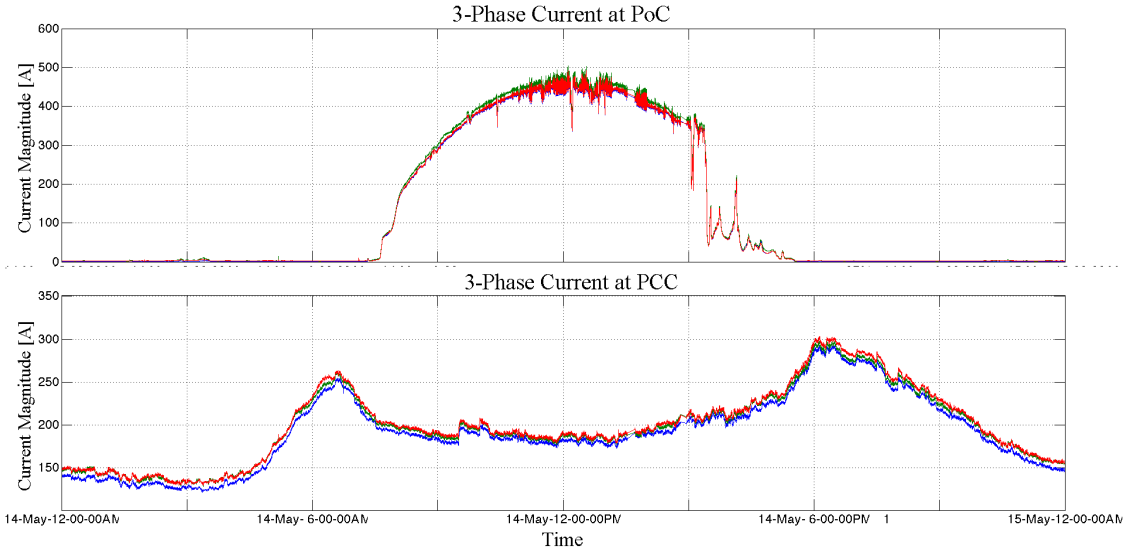

Figure 5-4: Three-phase current at the PV plant (PoC) and at the PCC

The positive sequence current of the PoC and PCC are compared in Figure 5-5.

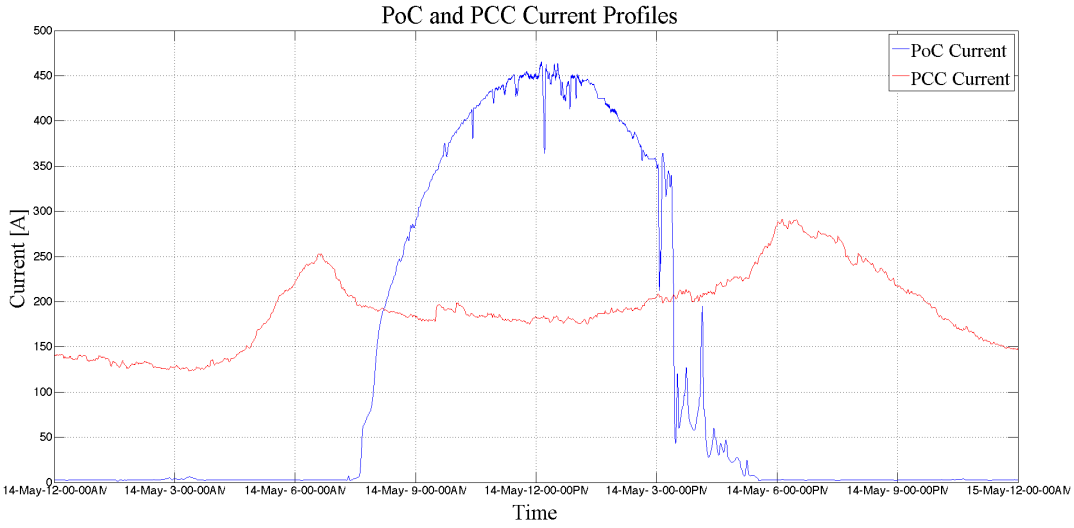

Figure 5-5: Positive sequence current at PoC and PCC

A significant part of the current produced by the PV plant is consumed downstream of the PoC based on the comparison of the absolute values of current at the PoC and the PCC.

Instantaneous changes in PV current are visible during the afternoon due to clouds, confirmed by the physical observation at the plant. Figure 5-6 shows the clouds congesting over the PV plant.

Figure 5-6: Clouds covering the PV power plant

When the supplied PV current is higher than the PCC load current, it is observed that the voltage profile at the PCC shown in Figure 5-3 is more stable. Without the contribution of the PV plant at 06:00 and 18:00, the voltage drop at the PCC during these peak hours is clearly visible. It demonstrates that the contribution of the PV plant is useful in terms of voltage support.

5.2.1 The relation between active power and phase angle

Micro-synchrophasors were used to compute the power at the PoC and PCC and the phase angle across the line (between the PoC and the PCC). The trend of the PV active power produced and the active power at the end of the 132 kV line into the PCC are compared against the voltage phase angle in Figure 5-7.

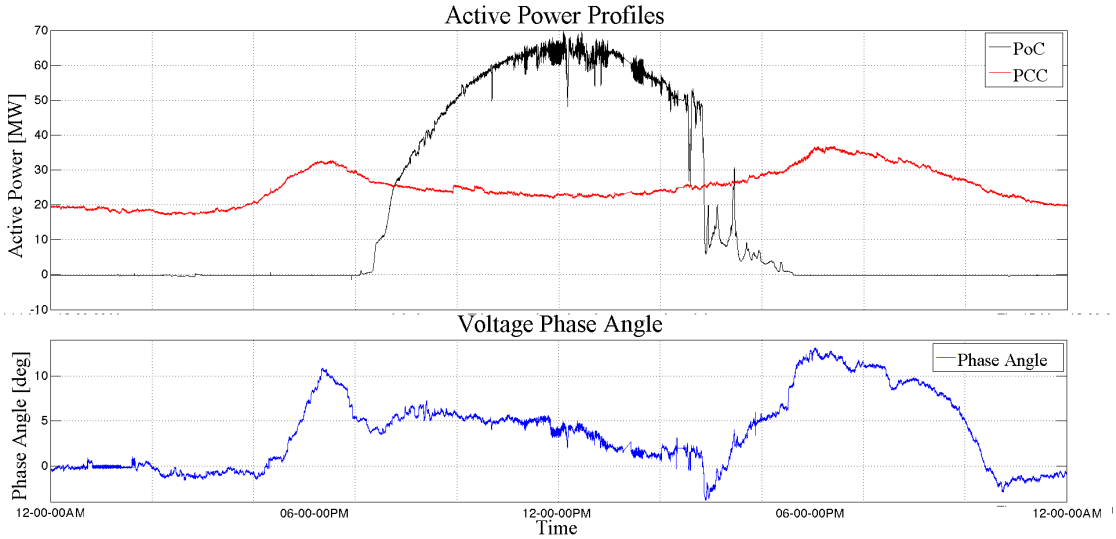

Figure 5-7: PV power generation and PCC consumption (above) compared with voltage phase angle (below)

The phase angle between the coherent voltage phasors across the line is well within the metrological performance of the synchrophasor recorders. Minor variations in this angle across the line are noted.

A clear correlation between the phase angle and the power at the PCC exists and between the phase angle and the production of the PV plant.

The impact of the afternoon cloud coverage at 15:20 caused a loss in PV power of 40 MW. This loss induced a sudden shift in the voltage phase angle.

The loss of 40 MW at 15:20 did not cause a significant change in the voltage magnitude at either the PoC or the PCC as the fault level of this network is sufficient to sustain the voltage.

The detectable phase angle change during this event is important in terms of the opportunity that micro-synchrophasors bring to the better understanding of integrated renewable energy sources in distribution networks.

If, for example, the fault level of the network is such that the sudden variation on PV production reflects on the voltage level to the extent that tap-changers start to compensate, only to re-adjust a while later when the clouds have moved over, then the additional stress to the tap-changer equipment is evident.

Later in this chapter, voltage stability is visually analysed using P-V curves. During that section the causes to changes in the P-V curve operating point are quantified, which showed that network operators can be empowered to appropriately manage voltage stability.

Causes of the changes in the operating points can be identified based on, for example, the phase angle difference between the PV plant and another point of observation.

Micro-synchrophasors are therefore demonstrated by the phase angle behaviour shown in Figure 5-7 to present the opportunity discussed above.

5.2.2 Field recorded resolution of the micro-synchrophasor

Phase angle variations over 10 minutes are presented in Figure 5-8 to demonstrate the resolution of the micro-synchrophasor.

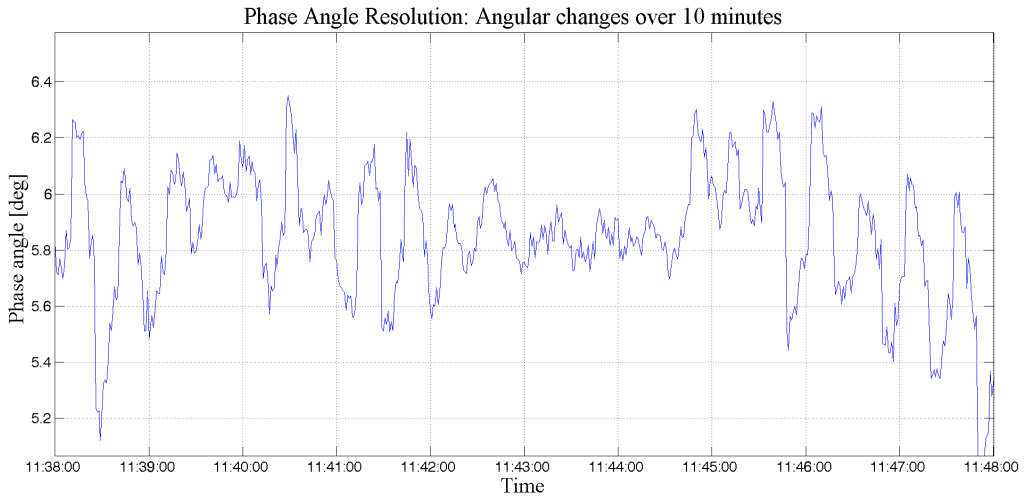

Figure 5-8: Phase angle variations over 10 minutes

To observe the level of the field recorded phase angle shifts that are detectable by the micro-synchrophasors small phase angle shifts over a 1 minute spread are observed in Figure 5-9.

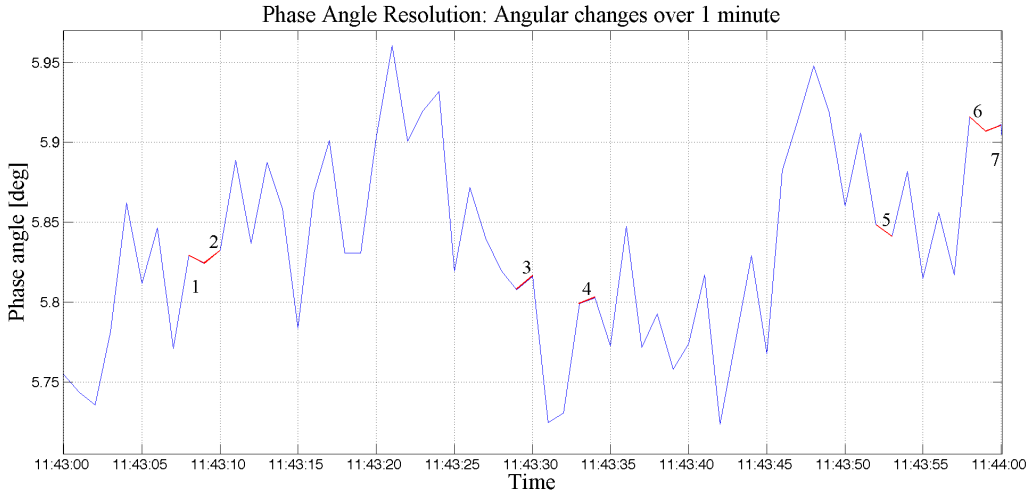

Figure 5-9: Small phase angle shifts observed over 1 minute

The observed angular shifts are listed in Table 5-1.

Table 5-1: Micro-synchrophasor resolution: small phase angle shifts recorded

Observation	**Phase shift value**
1	0.0051°
2	0.0082°
3	0.0080°
4	0.0037°
5	0.0072°
6	0.0091°
7	0.0043°

The resolution of the micro-synchrophasors enabled detection of field recorded phase angle shifts at millidegrees. In this case, the smallest angular shift of 0.0036° were measured, but several shifts as small as 0.0011° were detected over the 24-hour timespan.

Constant changes in the phase angle, particularly seen in Figure 5-8, are caused by the small signal variations between the PoC and PCC over the line. While such small angular variations at 132 kV may not be cause for concern, it still shows the detection capabilities of micro-synchrophasors recorded in a practical environment.

The recorded micro-synchrophasor resolutions are able to detect millidegree phase angle shifts demonstrated the viability of the micro-synchrophasor to monitor down to LV consumer level networks.

5.3 Voltage stability analysis with micro-synchrophasors

Steady-state stability is analysed by means of the power transfer curve, whereas voltage stability is analysed on P-V curves. The results of this analysis are used to validate the opportunity of applying micro-synchrophasors to improve existing approaches to these analyses.

5.3.1 Steady-state stability

The relation between power transferred from the PoC to the PCC as function of the phase angle between these points, is shown in Figure 5-10. Micro-synchrophasors were recorded at a rate of one sample per second over the 24-hour period for this analysis.

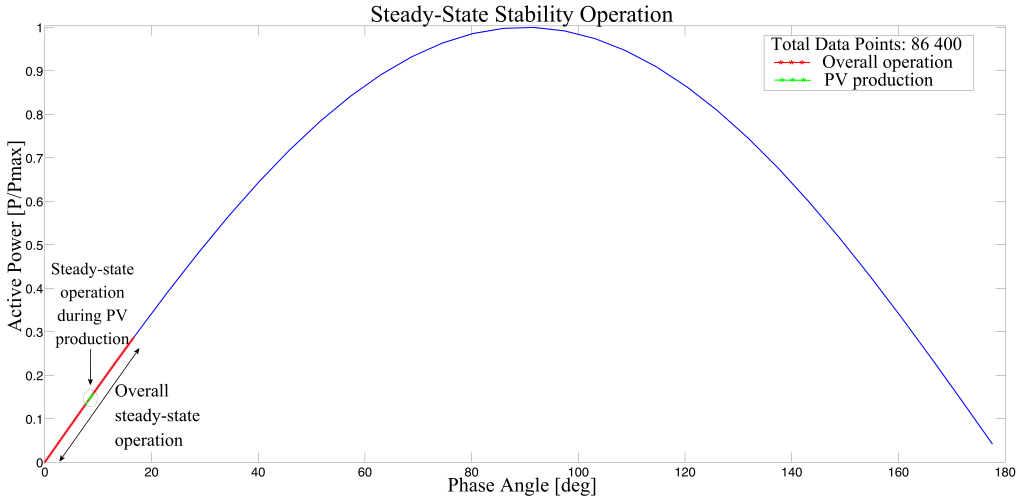

Figure 5-10: Steady-state power transfer between the PoC and PCC

The maximum point of transferred power occurred at P/P_{max} = 0.2608 per unit and a phase angle between the PoC and the PCC of 15.12°. This state of operation occurred during a time when no PV power was contributed to the distribution system, specifically at 18:38.

It is shown on the curve in Figure 5-10 what points of operation relate to the PV plant contributing, and when not. The phase angle ranges from 9.00° to 15.12° when the PV plant is not generating energy, while ranging between 3.51° and 6.88° during PV plant production.

It confirms that the network benefits by the contribution of the PV plant. A comparison of the phase angle and the per unit power transfer for different production levels of the PV plant is done in Table 5-2

Table 5-2: Steady-state stability results of the time intervals

	Interval	**PV plant production**	**Phase angle** [δ°]	**Operating Point** [P/P_{max}]
1	06:10:15	0%	12.15°	0.210
2	12:01:01	100%	5.03°	0.088
3	18:24:30	0%	15.88°	0.273

The peak PV production (12:01:01 PM) data sample occurs at a of 5.03° and normalised power transfer of 0.088 per unit. This δ-P relation is much smaller compared to the the higher power transfer and increase phase angles occurring when the PV plant is off.

The results demonstrated that the PV plant contributed to the resiliency of the steady-state stability of the distribution network.

These findings presented the contribution of micro-synchrophasors to better understand of the interaction between RPP generation and network performance.

5.3.2 Voltage Stability

Analysis on a P-V curve is one of the most accepted means to evaluate the voltage stability. Micro-synchrophasors can be used to construct PV curves as shown in Figure 5-11.

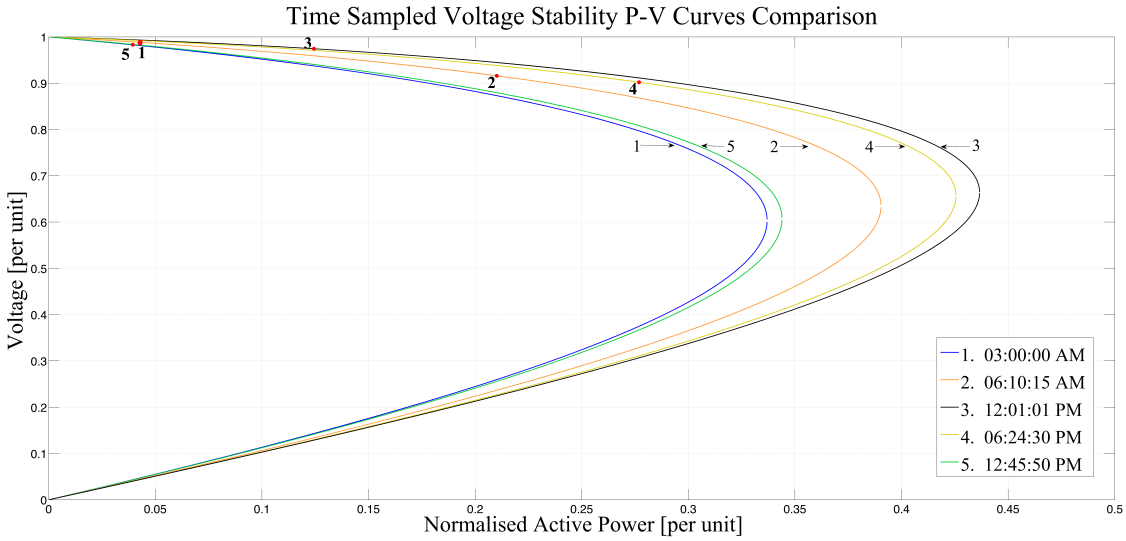

Figure 5-11: Visualisation of voltage stability at different instances in time

Observe the point of operation indicated on each curve. It visualises the VSM by the distance between this point and the critical point, located on the nose of the curve.

- Points 1 and 2 shows the largest VSM, since it occurred during very low loading conditions. The PV plant was out of production at these times.
- Points 2 and 4 shows a large reduction in the VSM, although well within the stable area of this distribution system.
- Point 3 illustrate the attribution of the PV plant as the VSM is much better than points 2 and 4 with the same amount of power handled in total by the distribution system.

The above P-V curves would not be possible without synchrophasor measurements. This shows the usefulness of micro-synchrophasors in distribution networks with sources of renewable energy integrated.

The VSM of the five P-V curves in Figure 5-11 are listed in Table 5-3.

Table 5-3: Calculated voltage stability margins of the field data samples

	Interval	**Voltage Stability Margin (VSM) [per unit]**
1	03:00:00 AM	0.2975
2	06:10:15 AM	0.1802
3	12:01:01 PM	0.3122
4	06:24:30 PM	0.1486
5	10:45:50 PM	0.3130

Each micro-synchrophasor from the 24-hour recordings can be used to construct a new P-V curve. A P-V curve per second, or even worse, 50 P-V curves per second, has the

potential for information overloading without any useful substance for the network operator. This would inevitably render the concept of constant visual tracking on P-V curves ineffective.

A profile that tracks the VSM over time can be more useful for visual appreciation of voltage stability. This type of profile is shown in Figure 5-12, based on synchrophasors recorded over 24-hours.

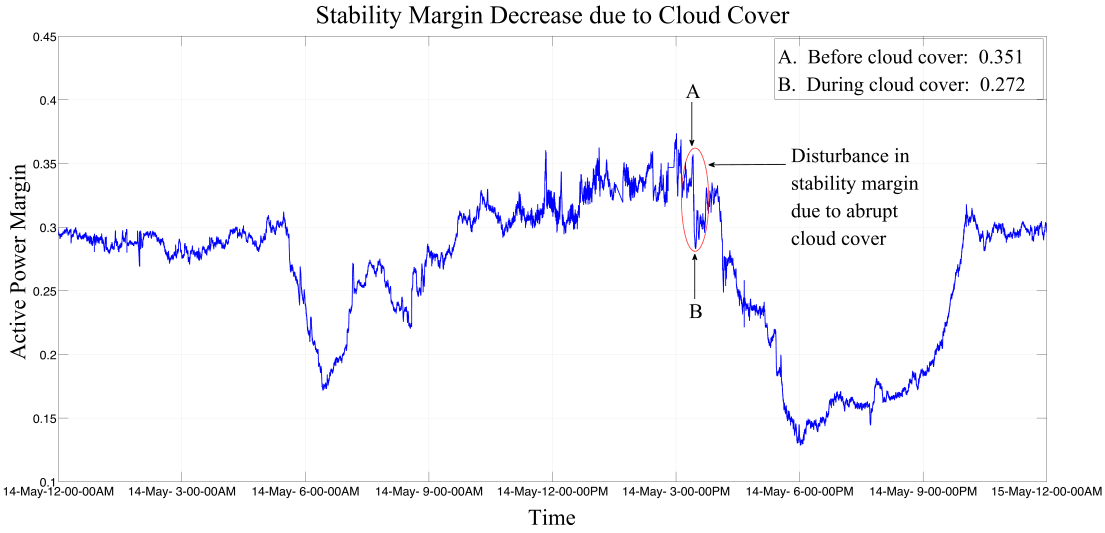

Figure 5-12: The VSM over a 24-hour period

The profile in Figure 5-12 can prove to be a simplistic means to monitor voltage stability. It provides a platform for visual tracking of VSM in real-time.

The goal is to operate the distribution system such that the VSM does not come too close to zero. A zero VSM on the profile represents operation at the nose of the P-V curve, which is where the distribution system enters the unstable area of operation.

The indicated shift on the profile represents a 7.9% VSM reduction due to the cloud cover across the PV power plant during the afternoon. This impact of the clouds is also noted in the voltage phase angle, shown in Figure 5-13.

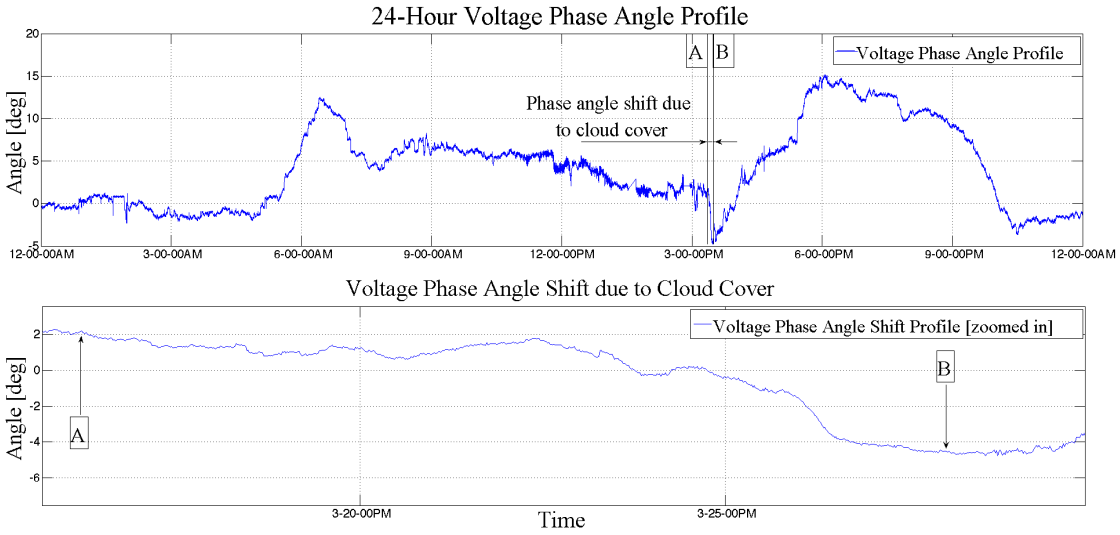

Figure 5-13: Voltage phase angle across the line over a 24-hour period (above) with the detail shown in the lower graph.

The angular shift reacts to the loss in PV power for roughly seven minutes and is not an instantaneous shift as initially perceived. Such a duration is too long for the disturbance to be classified as transient and the system is considered to remain in steady-state.

The change in phase angle across the line can be lastly illustrated on P-V curves. Stability can be evaluated by comparing the voltage stability just before the clouds set in with the voltage stability during full cloud cover shown in Figure 5-14.

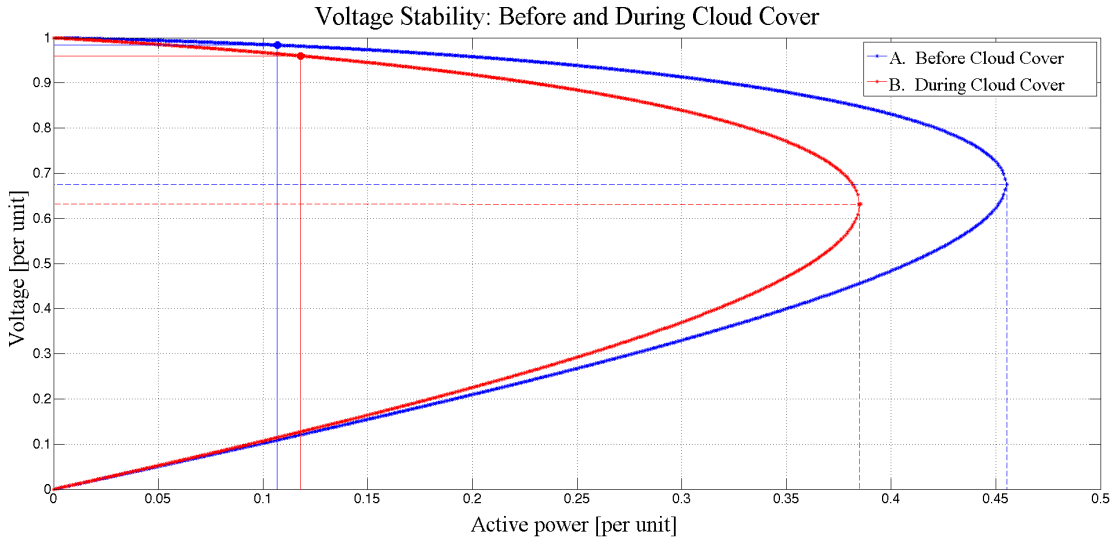

Figure 5-14: Voltage stability comparison during cloud coverage

The clouds caused the operating point to minimally shift towards the nose of the P-V curve. Loss in PV production on the P-V curve is visible, but only imposed a marginal impact on the voltage stability.

5.3.2.1 Voltage Stability Tracking on 3-Dimensional P-V Curves

Chronological voltage stability tracking can also be conducted by adding the time-stamping identities of the micro-synchrophasors as the 3rd dimension to the P-V curves. An improvement in the visualisation of the change in the P-V curves is achieved by Figure 5-15.

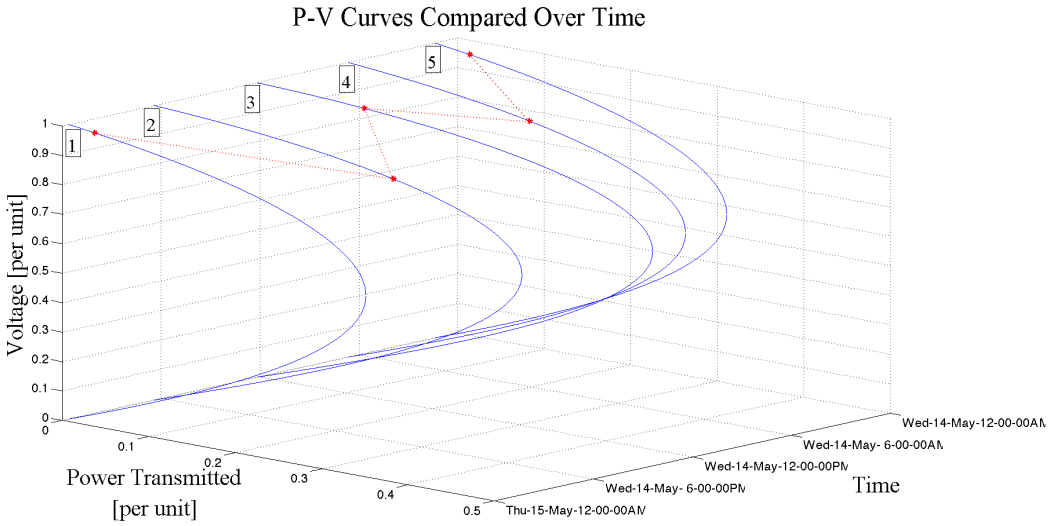

Figure 5-15: 3-dimensional P-V curves to visualize voltage stability over time

The introduction of a 3rd axis on the P-V curves presents new monitoring opportunities. These 3D displays are not only limited to time-based classifications, but can also include opportunities to simultaneous monitor voltage stability between different nodes in a network.

By strategically implementing micro-synchrophasor recorders on various buses at different locations will enable wide-area supervision on the voltage stability in a system. Such applications possible with micro-synchrophasors can provide advanced monitoring applications in distribution networks.

5.4 Conclusion

Micro-synchrophasor recordings proved to be valuable in evaluating the interaction between a PV plant and a distribution network. Field data was recorded at the PoC of a 75 MW PV plant and an upstream sub-transmission switching station serving as PCC.

Micro-synchrophasors used in this chapter were recorded over a 24-hour period. The 132 kV distribution line of just more than 100 km has sufficient impedance to result in a detectable phase angle variation across the line. The steady-state voltage profiles at the PoC and the PCC were improved during PV generation, since strain over the line was relieved.

The recorded micro-synchrophasor field data were utilised to visually analyse the steady-state and voltage stability. This was conducted by evaluating the operational changes on the power-transfer and P-V stability curves.

To holistically demonstrate the changes in stability, five data samples, each at a different interval of the recording period, were used. On average, the phase angle across the line during PV generation was 7.44° less than during peak power consumption and a reduction of 0.13 p.u. in power transmitted from the PCC to the PoC.

Maximum PV generation improved the voltage stability by increasing the VSM by 21% compared to high network loading without PV generation. It was found that sudden cloud coverage that caused a 40 MW loss in PV production, which only induced a marginal decrease in the VSM. Stability was not threatened since the fault level of this network was sufficient.

A means to chronologically track the VSM was presented based on the trend of VSM. This profile of VSM showed that no concern to steady-state voltage instability exists over the analysed 24-hour period.

A 3-D visualisation of the P-V curves by plotting the P-V curves against time was lastly shown to be helpful in chronologically tracking the change in these curves. It was also noted that these curves can also be applied to simultaneously monitor stability interactions between different locations.

This chapter presented the viability of the micro-synchrophasor to visualise stability analysis used to evaluate the interaction of the PV plant integrated with the distribution system. Results from the field recordings showed PV integration to be beneficial for the steady-state and voltage stability of the distribution network.

Chapter 6: Conclusion

6.1 Summary

The aim of this research was to evaluate the opportunity of applying high-precision synchrophasors, termed micro-synchrophasors, to monitor RPPs integrated onto distribution systems. This research topic was formulated in response to the need for advance network supervision over widespread integration of RPPs on the South African power grid.

To effectively visualise distribution network operation highly accurate recordings were required. Therefore, micro-synchrophasors in principle needed to have high-resolution metrological capabilities with a time stamping certainty better than 1 μ-second between the recorders.

Due to these strict requirements, the metrological capabilities of an IEC 61000-4-30 Class A ed. 3 certified PQ instrument were first verified for the ability to micro-synchrophasor level recordings. Once the verification tests proved that this recorder to is capable of micro-synchrophasor measurements, field recordings were conducted to quantify the impact of a 75 MW PV power plant on a distribution network.

The work conducted in this research can be categorised in 2 sections:

a) Tests to verify the metrological capabilities of the IEC 6100-4-30 Class A ed. 3 PQ recorder used for micro-synchrophasor measurements. The accuracy and certainty in measurement were determined by an Omicron CMC 256plus™. Results were verified by using the proposed micro-synchrophasor requirements [19] as benchmark. A second set of tests was performed on a LV distribution cable, which served as a supplementary verification.

b) Field recordings using micro-synchrophasors to quantify the interaction of a 75 MW PV power plant connected to an upstream distribution station. The network steady-state and voltage stability were quantified by visually evaluating the change in points of operation on power-transfer (δ-P) and P-V stability curves. This study validated the usefulness of micro-synchrophasors to monitor the impact of an RPP integrating with a distribution network.

The field study results showed that the integrated PV power plant improved the stability of this distribution network. It improved the steady-state and voltage stability by alleviating

the energy flow from the PCC towards the downstream loads. Although the energy production of this PV plant was shown to be able to change significantly when not expected, no adverse effects on voltage stability resulted.

Results of the work conducted in this research demonstrated the viability of using micro-synchrophasors to evaluate the integration of a RPP with the distribution system. Visualisation of stability by means of micro-synchrophasors is but one useful feature, which can assist engineers and operators in the better understanding of how sources of renewable energy interact with a distribution network.

6.2 Evaluation of results

6.2.1 Phase angle accuracy

Phase angle is of specific concern when micro-synchrophasors is considered as the phase angle across distribution network impedances cause less phase displacement between synchrophasors. The ability of the IEC 61000-4-30 Class A ed. 3 PQ instrument used was evaluated by means of emulating different conditions with an Omicron CMC 256plus™.

The results of these tests, conducted in Chapter 3.2.1, are summarised below:

Table 6-1: Phase angle test results

	Average Difference from Generated Phase Angle	**Total Vector Error (TVE)**
5.00° - 1.00°	0.00058°	0.05%
1.00° - 0.10°	0.00073°	0.70%
0.10° - 0.01°	0.00033°	0.30%

The micro-synchrophasor recorders provided sufficient resolution to accurately measure phase angles between 1.00° and 0.01°. All phase angles were recorded with a TVE less than 1.00%.

6.2.2 Certainty in measurement

The certainty in measurements presented an absolute error in phase angle measurements of 0.00192 °, indicating a time-stamp uncertainty of 107 ns between two instruments. The true spread was calculated to revolve around 0.00038° (as opposed to an ideal 0.00°).

The time uncertainties of these results are compared with the proposed micro-synchrophasor sampling requirements [19] on a logarithmic time scale:

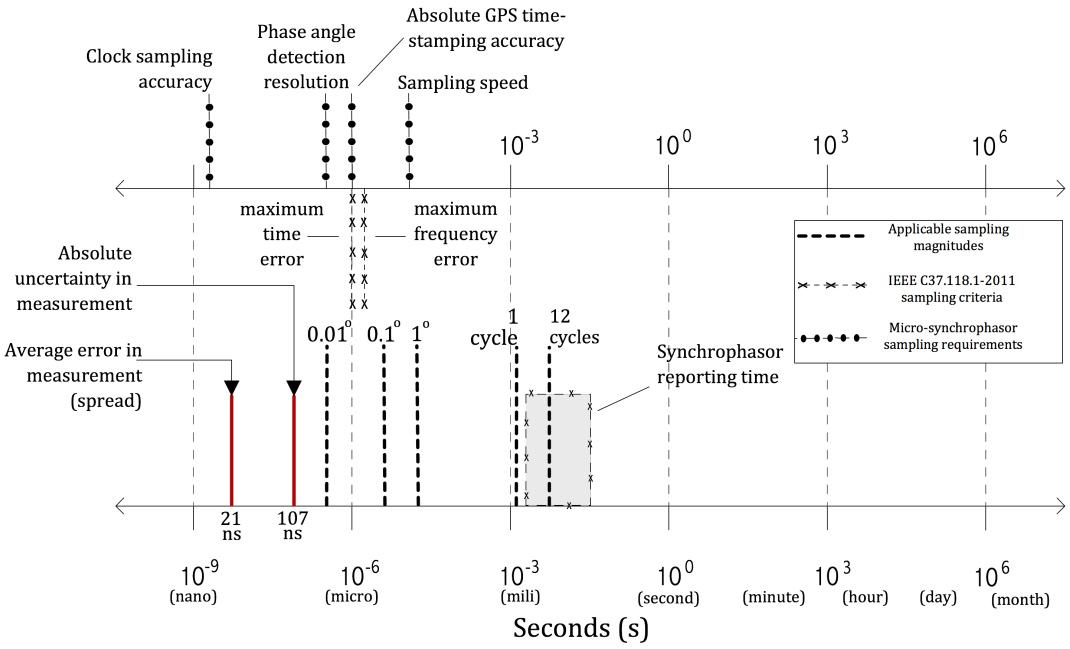

Figure 6-1: Results (in red) compared to proposed requirements

The absolute uncertainty of 107 ns is nearly ten times smaller than the maximum time error of 1.00 μs for a 50 Hz fundamental waveform. This indicated that the recording instruments presented sufficient metrological capabilities of the instruments to accurately measure micro-synchrophasors.

It is worth mentioning that no other publication at the time was found to report an instrument to have a better certainty in synchrophasor measurements.

6.2.3 Impedance measurement of a LV distribution cable

The supplementary verification test on a LV distribution cable was done by using a reference impedance as benchmark.

The reference impedance was recorded with a EN 6090-0 certified loop impedance tester. On average, the line impedance calculated with micro-synchrophasors deviated from the reference impedance by 1.65% ($1.92\angle 0.02^\circ$ $m\Omega$).

Taking into account that the EN 6090-0 impedance recorder did not have the level of precision the CMC 256plus™, the test results presented a realistic measure of micro-synchrophasor capabilities in a practical environment.

6.2.4 Simulated results vs field recordings

The field recorded steady-state and voltage stability results in Chapter 5 corresponded with the simulated results in Chapter 4. In both cases the steady-state and voltage stabilities were more secure with PV generation injected into the grid.

The field recorded results on steady-state and voltage stabilities are compared below:

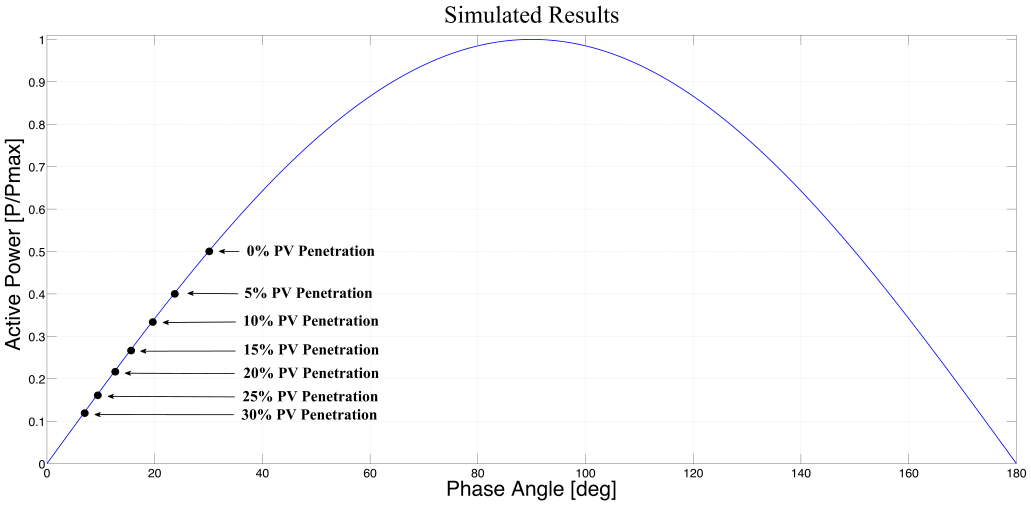

(a) Simulated steady-state stability results

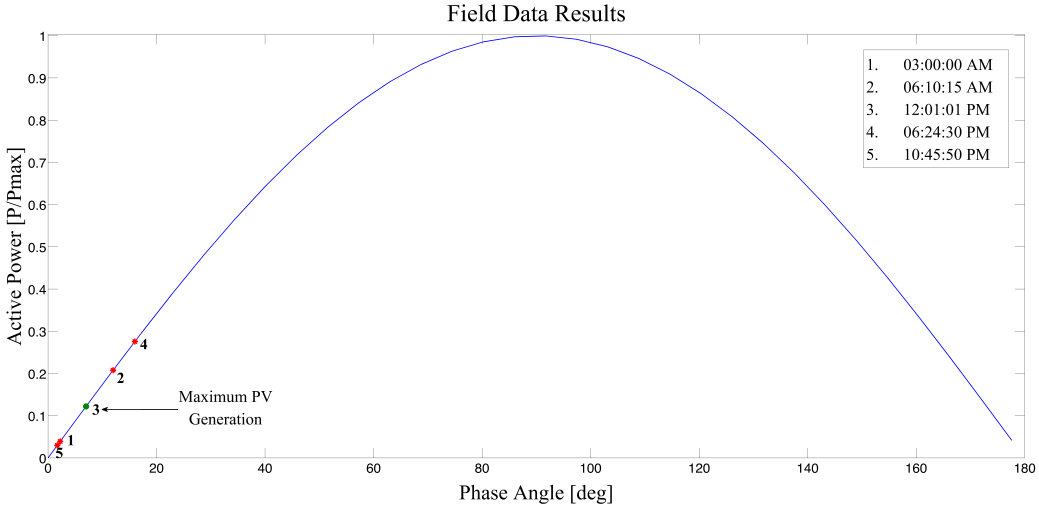

(b) Field recorded steady-state stability

Figure 6-2: Simulated and field recorded steady-state stabilities

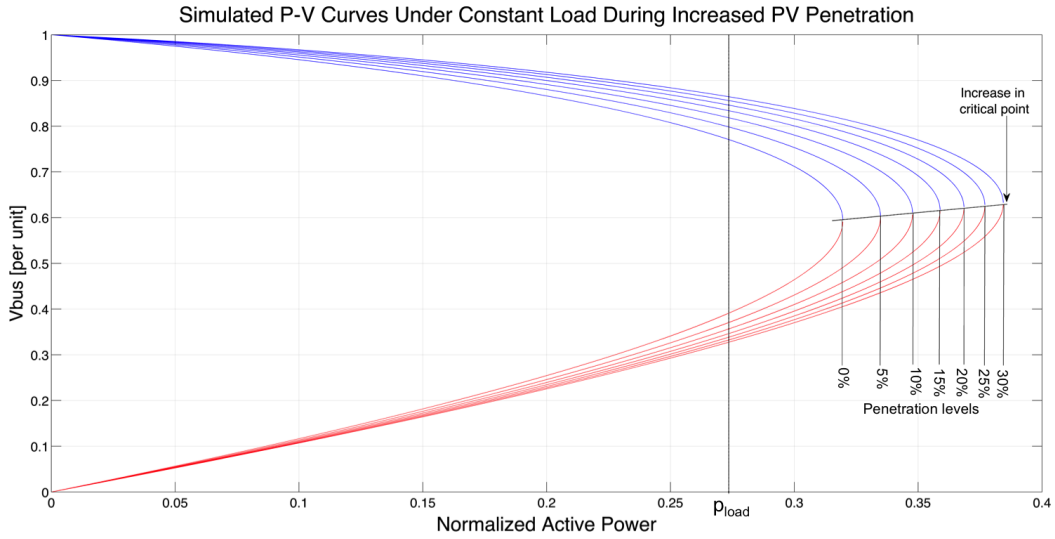

(a) Simulated voltage stability results

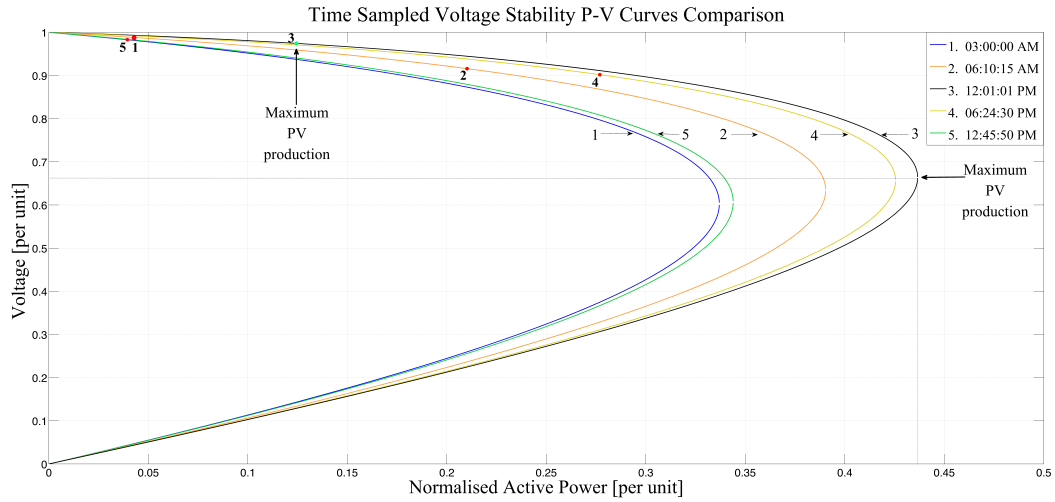

(b) Field recorded voltage stability result

Figure 6-3: Simulated and field recorded voltage stability results

On both accounts the following similarities were found:

- The δ-P value on the power-transfer curves was lowest during maximum PV production.
- Voltage stability was improved due to increases in the VSM as PV generation increased

6.2.5 Maximum PV production vs peak loading

Visualisation on steady-state and voltage stability proved the integrated PV power plant to be an asset in grid resiliency. Peak loading conditions was the leading parameter to measured instabilities, which occurred when the PV plant was not generating power. The operating points provided a measure of improved stability induced by the addition of PV generation.

Comparison of the steady-state stability demonstrated a difference in the δ-P relation of 7.44°-0.13 pu, as shown in Figure 6-4.

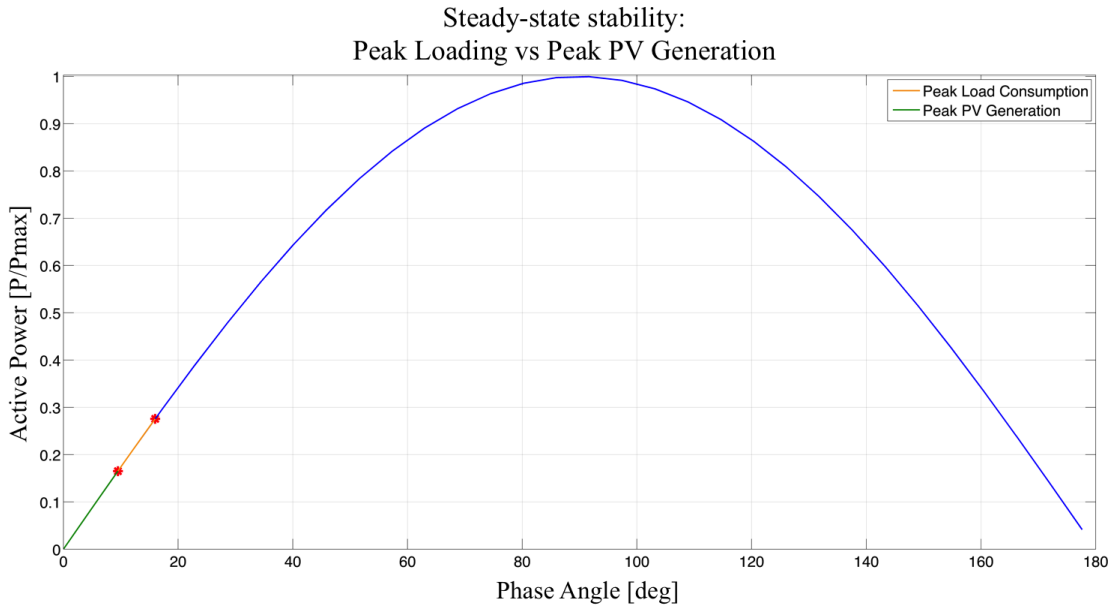

Figure 6-4: Maximum PV compared to peak loading steady-state stability

The difference in voltage stability is demonstrated by means of comparing the VSM in Figure 6-5, which showed that maximum PV generation improved the VSM by 0.21 pu (21%).

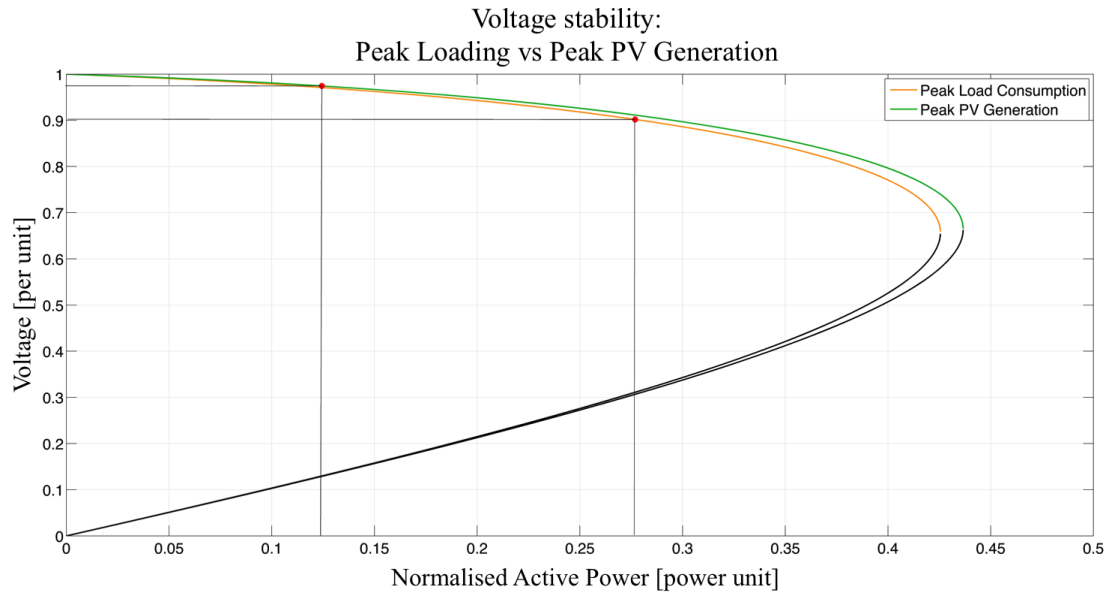

Figure 6-5: Maximum PV compared to peak loading voltage stability

These comparisons provided a visual confirmation of the contribution by the PV power plant of improving the resilience in the network stability.

6.2.6 Instability due to cloud cover

Afternoon cloud cover caused a 40 MW loss in PV production, which caused a 3° change in the voltage phase angle. The resulting effect on the VSM was not cause for concern, since voltage stability was still higher than during the peak loading intervals.

When comparing the VSM during cloud cover with peak loading intervals, the VSM at peak loading is still 0.14 (14%) lower than during cloud cover.

Such a minor impact from cloud coverage indicated that the PV plant does not have the capacity to degrade network stability, as opposed to the network loading that has been found to dictate stability levels.

6.3 Conclusion

The contents of this research demonstrated the usefulness of micro-synchrophasors to evaluate the interaction of a RPP, in this case a 75 MW PV power plant, integrated onto a sub-transmission network.

The initial metrological tests conducted to verify and validate the instruments for micro-synchrophasor recordings provided the following findings:

- The synchrophasor instruments used in this research comprised the required metrological capabilities to perform micro-synchrophasor level recordings.
- The synchrophasor recorder could measure phase angles of 0.01° with sufficient certainty, which is the smallest proposed angular detection requirement for micro-synchrophasor recordings [19].
- Phase angles were recorded with an uncertainty of 0.00192°, indicating a time synchronization certainty of 107 ns between the instruments when used in 50 Hz systems.
- The ability of recording small phase angles was practically verified by applying micro-synchrophasors to measure line impedance of a cable

The opportunity of applying micro-synchrophasors for a better understanding of RPPs integrated onto distribution systems was demonstrated by visualization of power transfer- and voltage stability parameters.

The micro-synchrophasor recordings provided visibility over:

- Voltage and current profiles at the PoC of the PV power plant and upstream distribution station (PCC).

- The voltage phase angle offset between the PoC and PCC.
- Active power transferred and energy flow between the PoC and PCC.
- Abrupt changes on PV generation due to cloud cover.
- Steady-state stability, quantified by the δ-P operational relation.
- Voltage stability, quantified by the VSM.

Analysis of the micro-synchrophasor field recordings of the PV power plant resulted in the following conclusions:

- Contingencies such as steady-state, voltage stability and phase angle response due to changes in PV generation and power consumption could be quantified using micro-synchrophasor recordings.
- The steady-state stability was improved during PV production due to the injected energy suppressing the phase angle difference between the PoC and PCC.
- PV generation presented strong characteristics to improve voltage stability, since the stability margins and critical points were highest during PV production.
- The resolution of the micro-synchrophasors was suffcient to detect millidegree phase angle shifts during the field recordings.
- Network power consumption dictated the phase angle profile and subsequently influenced the instability levels on a negative manner.
- Cloud disruptions also directly affected the phase angle value, but did not cause concerning instability levels.
- The integrated PV power plant had a positive impact on the distribution system by making the system more resilient against voltage instabilities.

The field study also illustrated the opportunity of using micro-synchrophasor technology for simultaneous supervision over different RPPs using a 3D visibility platform able to incorporate several P-V curves simultaneously.

The opportunity of applying micro-synchrophasors to monitor RPP distribution grid integration was validated by the results of the field study on an integrated 75 MW PV power plant.

Given the amount of current and prospective integrated RPPs, network operators would require a support basis to be in place to monitor and manage these sources of renewable energy. This research provided substantiation of the utilisation of micro-synchrophasor recorders to be a viable solution for such applications.

6.4 Recommendations

Micro-synchrophasors can be considered to improve the operation of a distribution system where significant distributed generation exist and based on sources of renewable energy.

6.4.1 A micro-synchrophasor monitoring platform

Synchrophasor-based support tools to visualise and track the stability of a power system are being utilised in for example Europe and the USA, but not in Africa.

A platform needs to be developed that offers visualisation of micro-synchrophasor data as a monitoring support tool. The fundamental purpose of such a platform is to report wide area operations in real-time on a simplistic and effective manner. With an increasing number of IPPs connected onto the South African power grid, such a platform can equip the systems operator to manage and supervise these newly integrated sources.

6.4.2 Improved data management infrastructure

The rates at which micro-synchrophasors report data can easily cause a data overflow over the network. It is important to ensure a broadband network with minimal signal latency is used for data reporting. Power systems (mainly in the USA and Europe) that use synchrophasors for wide-area monitoring have implemented data concentrators to accommodate high data capacity.

With synchrophasors only now starting to be installed in the South African power system, these data concentrators must also be implemented to ensure secure data reporting.

6.4.3 Ensuring feasible cost of micro-synchrophasor recorders

A large number of instruments would be required for wide-area monitoring in distribution networks. To keep the cost of such recorders low, it is recommended to incorporate micro-synchrophasor technology into any recording instrument that has time-coherent measurement capabilities. This it would eliminate the added cost of a dedicated μPMU and can also present new opportunities to integrate synchrophasor-based monitoring with recorded PQ trends.

6.5 Future work

The results of the work conducted in this research have presented a list of new research opportunities.

6.5.1 Using micro-synchrophasors for wide-area supervision in distribution networks

Wide-area supervision has already been realised at transmission systems, but not yet in distribution networks. The next step in micro-synchrophasor supervision will focus on applying several instruments at different locations in a distribution network. The goal would be to achieve the same level of visibility that wide-area monitoring systems incorporates in transmission systems.

6.5.2 Monitoring renewable energy at residential level

Consumer-based power generation, such as rooftop PV arrays often supplies power back onto the residential grid. This is also of concern since LV networks are not designed to incorporate reverse power flow.

By installing micro-synchrophasor recorders at LV locations with renewable power sources, the impact on steady-state parameters (δ, V, P, Q) can be evaluated. The goal will be to analyse the impact on LV grids, while using visual applications to manage the injected power so that residential network can operate securely.

References

[1] South Africa, National Planning Commission, *National Development Plan 2030 Our Future-make it work*. Union Buildings, Pretoria: Department: The Presidency, 2011, ISBN: 9780621411805.

[2] D. B. Martins, T. Zungu, N. Magubane, and Y. Chetty, *Annual Performance Plan 2014/15*. Union Buildings, Pretoria: Department of Energy, 2014, ISBN: 978-0-621-42503-1.

[3] C. Yelland, *Huge renewable, nuclear build ahead for SA, but coal is here to stay | Daily Maverick*, Mar. 2011. [Online]. Available: http://www.dailymaverick.co.za/article/2011-03-30-huge-renewable-nuclear-build-ahead-for-sa-but-coal-is-here-to-stay (visited on 07/11/2014).

[4] Forsom Labs, *Meteorological Data*. [Online]. Available: https://www.folsomlabs.com/modeling/environment/meteorological (visited on 08/14/2014).

[5] Department of Energy, *Renewable Energy*, en-US, 2014. [Online]. Available: http://www.energy.gov.za/files/renewables_frame.html (visited on 11/26/2014).

[6] Department of Energy, *Integrated Resource Plan of Electricity 2010-2030*, Pretoria, 2013. [Online]. Available: http://www.doe-irp.co.za/content/IRP2010_updatea.pdf (visited on 11/27/2014).

[7] IEEE Standards Coordinating Committee 21, *IEEE Guide for Smart Grid Interoperability of Energy Technology and Information Technology Operation with the Electric Power System (EPS), End-Use Applications and Loads*, IEEE Std 2, IEEE-SA Standards Board and American National Standards Institute, Eds., September. New York: IEEE, 2011, ISBN: 9780738167275.

[8] N. A. Hidayatullah, B. Stojcevski, and A. Kalam, "Analysis of Distributed Generation Systems, Smart Grid Technologies and Future Motivators Influencing Change in the Electricity Sector," *Smart Grid and Renewable Energy*, vol. 02, no. 03, pp. 216–229, Aug. 2011, ISSN: 2151-481X. DOI: 10.4236/sgre.2011.23025.

[9] K. E. Martin, D Hamai, M. G. Adamiak, S Anderson, M Begovic, G Benmouyal, G Brunello, J Burger, J. Y. Cai, B Dickerson, V Gharpure, B Kennedy, D Karlsson, A. G. Phadke, J Salj, V Skendzic, J Sperr, Y Song, C Huntley, B Kasztenny, and E Price, *IEEE Transactions on Power Delivery*,

[10] M Wache and D. C. Murray, "Application of Synchrophasor Measurements for Distribution Networks," in *2011 Power and Energy Society General Meeting*, San Diego, CA: IEEE, 2011, pp. 1–4, ISBN: 9781457710025. DOI: 10.1109/PES.2011.6039337.

[11] S. F. Bush, "Synchrophasor Applications," in *Communication-Enabled Intelligence for the Electric Power Grid*, 1st, Chichester, West Sussex: John Wiley and Sons, Ltd., 2014, ch. Synchropha, pp. 415–434, ISBN: 978-1-119-97580-9.

[12] IEEE Power and Energy Society, *IEEE C37.118.1-2011 - Standard for Synchrophasor Measurements for Power Systems*, IEEE Standards Association, Ed., December. New York, NY: IEEE, 2011, vol. 2011, ISBN: 9780738168111.

[13] J. D. Glover, M. S. Sarma, and T. J. Overbye, *Power System Analysis and Design, SI Edition*, 5th, H. Gowans and S. Meherishi, Eds. Stamford, CT: Gentage Learning, Global Engineering, 2012, ISBN: 9781111425791.

[14] A. G. Phadke, "Synchronized phasor measurements - a historical overview," *Transmission and Distribution Conference and Exhibition 2002: Asia Pacific. IEEE/PES*, vol. 1, pp. 476–479, 2002. DOI: 10.1109/TDC.2002.1178427.

[15] A. G. Phadke, T. Hlibka, M. Ibrahim, and M. G. Adamiak, "A Microcomputer Based Symmetrical Component Distance Relay," in *IEEE Conference Proceedings Power Industry Computer Applications Conference, 1979. PICA-79.*, New York, NY: IEEE, 1979. DOI: 10.1109/PICA.1979.720045.

[16] A. G. Phadke, J. S. Thorp, and M. G. Adamiak, "A New Measurement technique for tracking voltage phasors, local system frequency, and rate of change of frequency," *Transactions of IEEE on PAS*, pp. 1025–1038, 1982.

[17] B. Barker, "Synchrophasors: progeny of a blackout," in *Public Power*, vol. 69, APPA, May 2011, pp. 1–5.

[18] USA. (Jun. 2015). Synchrophasor applications in transmission systems. U. D. of Energy, Ed., [Online]. Available: https://www.smartgrid.gov/recovery_act/program_impacts/applications_synchrophasor_technology.html (visited on 07/20/2015).

[19] A. V. Meier, D. Culler, and A. Mceachern, "Micro-Synchrophasors for Distribution Systems," in *Innovative Smart Grid Technologies Conference (ISGT), 2014*, Washington. DC: IEEE, 2014, pp. 1–5. DOI: 10.1109/ISGT.2014.6816509.

[20] I. M. El-Amin and M. K. Ahmed, "Impact of a PV system on a power grid," in *International Symposium on Power Electronics, Electrical Drives, Automation and Motion*, IEEE, Jun. 2014, pp. 966–970, ISBN: 978-1-4799-4749-2. DOI: 10.1109/SPEEDAM.2014.6872082.

[21] J. Xu, B. Li, Y. Zou, C. Li, X. Mao, X. Mao, S. Pan, and N. Zhou, "Characteristics of static voltage stability for distributed generation integrated into power system and its impacts analysis," in *2013 IEEE PES Asia-Pacific Power and Energy Engineering Conference (APPEEC)*, Hong Kong: IEEE, Dec. 2013, pp. 1–6, ISBN: 978-1-4799-2522-3. DOI: 10.1109/APPEEC.2013.6837204.

[22] C. Paton, *Department of energy delays frustrate power producers | Energy | BDlive*, Johannesburg, Nov. 2014. [Online]. Available: http://www.bdlive.co.za/business/energy/2014/11/20/department-of-energy-delays-frustrate-power-producers (visited on 12/05/2014).

[23] M. Duckheim, J. Reinschke, P. Gudivada, and W. Dunford, "Voltage and power flow oscillations induced by PV inverters connected to a weak power distribution grid," in *IEEE Power and Energy Society General Meeting*, Vancouver, BC: IEEE, 2013, pp. 1 –5, ISBN: 9781479913039. DOI: 10.1109/PESMG.2013.6672830.

[24] J. Desmet, B. Verhelst, and C. Debruyne, "Test Field for LV Distribution Systems," in *22 nd International Conference on Electricity Distribution (CIRED)*, Stockholm: CIRED, 2013, pp. 10–13.

[25] H. Teng, C. Liu, M. Han, S. Ma, and X. Guo, "IEEE9 Buses System Simulation and Modeling in PSCAD," in *2010 Asia-Pacific Power and Energy Engineering Conference*, Chengdu: IEEE, 2010, pp. 1–4, ISBN: 978-1-4244-4812-8. DOI: 10.1109/APPEEC.2010.5448242.

[26] R Hiiseyin and B. S. Guru, *Electric Machinery and Transformers*, Third. Oxford, United Kingdom: Oxford University Press, Inc., 2001, ISBN: 9780195138900.

[27] H. Jóhannsson, R. Garcia-Valle, J. T. G. Weckesser, A. H. Nielsen, and J. Ø stergaard, "Real-time stability assessment based on synchrophasors," in *2011 IEEE PES Trondheim PowerTech: The Power of Technology for a Sustainable Society, POWERTECH 2011*, Trondheim: IEEE PES, 2011, pp. 1–8, ISBN: 9781424484195. DOI: 10.1109/PTC.2011.6019236.

[28] C. W. Taylor. University of Michigan, MI, United States: McGraw-Hill Ryerson, Limited, ISBN: 9780070631847.

[29] S. Shahrtash and H. Khoshkhoo, *IET Generation, Transmission & Distribution*, no. 11, pp. 1143–1152, ISSN: 1751-8687. DOI: 10.1049/iet-gtd.2011.0771.

[30] G. Cipriani, R. Miceli, and I. C. Spataro, "Uncertainty evaluation in the measurements for the electric power quality analysis," *2013 International Conference on Renewable Energy Research and Applications (ICRERA)*, no. October, pp. 20–23, 2013.

[31] Joint Committee for Guides in Metrology (JCGM), *Evaluation of measurement data: Guide to the expression of uncertainty in measurement*, September. JCGM publications, 2008, p. 120, ISBN: 9267101889. DOI: 10.1373/clinchem.2003.030528. [Online]. Available: http://www.bipm.org/en/publications/guides/gum.html$\backslash$nhttp://www.bipm.org/utils/common/documents/jcgm/JCGM_100_2008_E.pdf.

[32] K. Draxler and R. Styblikov á, "Influence of instrument transformers on quality of electrical power and energy measurement," in *IEEE International Symposium on Industrial Electronics*, San Diego, CA: IEEE, 2007, pp. 1317–1321, ISBN: 1424407559. DOI: 10.1109/ISIE.2007.4374790.

[33] D. Belega and D. Petri, "Accuracy analysis of the multicycle synchrophasor estimator provided by the interpolated dft algorithm," *Instrumentation and Measurement, IEEE Transactions on*, vol. 62, no. 5, pp. 942–953, 2013, ISSN: 0018-9456. DOI: 10.1109/TIM.2012.2236777.

[34] G. Barchi, D. Macii, and D. Petri, "Synchrophasor estimators accuracy: a comparative analysis," *Instrumentation and Measurement, IEEE Transactions on*, vol. 62, no. 5, pp. 963–973, 2013, ISSN: 0018-9456. DOI: 10.1109/TIM.2012.2236776.

[35] G. Barchi, G. S. Member, D. Fontanelli, D. Macii, S. Member, and D. Petri, "On the Accuracy of Phasor Angle Measurements in Power Networks," *IEEE Transactions on Instrumentation and Measurement*, vol. 64, no. 5, pp. 1129–1139, 2015.

[36] E. Demeter, S. O. Faried, and T. S. Sidhu, "Signal phase shifting during synchrophasor measurements," in *Canadian Conference on Electrical and Computer Engineering (CCECE)*, vol. 1, Saskatoon: IEEE, 2005, pp. 557–560, ISBN: 0-7803-8885-2. DOI: 10.1109/CCECE.2005.1556992.

[37] H. S. Hirlekar, B. H. Chowdhury, and S. Member, "Towards On-Line Voltage Stability Assessment Using Synchrophasors," *Power and Energy Society General Meeting, IEEE*, pp. 1–6, 2012. DOI: 10.1109/PESGM.2012.6344774.

[38] M. H. J. Bollen, *Integration of distributed generation in the power system*, First. New Jersey, NY: John Wiley and Sons, Ltd., 2011, ISBN: 9781118029039 1118029038 9781118029015 1118029011. [Online]. Available: http://site.ebrary.com/id/10494547.

[39] G. N. Tiwari and D. Swapnil, *Fundamentals of Photovoltaic Modules and their Applications*, J. Hunt, Ed. Delhi, New Delhi, India: RSC Energy Series, 2010, p. 402, ISBN: 978-1-84973-020-4. DOI: 10.1039/9781849730952.

[40] A. Luque and S. Hegedus, *Photovoltaic Science Handbook of Photovoltaic Science*, Second, A. Luque and S. Hegedus, Eds. Chichester, West Sussex: John Wiley and Sons, Ltd., 2011, ISBN: 9780470721698.

[41] A. von Meier and G. D. Rodriguez, "Monitoring for impacts of distributed resources: Initial planning considerations," in *2013 IEEE Power & Energy Society General Meeting*, Vancouver, BC: IEEE, 2013, pp. 1–5, ISBN: 978-1-4799-1303-9. DOI: 10.1109/PESMG.2013.6672386.

[42] RSA Grid Code Secretariat, *Grid Connection Code for Renewable Power Plants (RPPs) Connected to the Electricity Transmission System (TS) or the Distribution System (DS) in South Africa*, version 2.6, Pretoria, 2012.

[43] S. Arifin, M. Masum, S. Khan, and A. Haque, "Improvement of Load-Margin and Bus Voltage of Bangladesh Power System with the Penetration of PV Based Generation," in *2013International Conference on Informatics, Electronics and Vision (ICIEV)*, Dhaka: IEEE, 2013, pp. 1–5, ISBN: 9781479904006.

[44] R. Shah and N. Mithulananthan, "Interconnection of PV based generator and its impact on Bangladesh power system stability," in *1st International Conference on the Developments in Renewable Energy Technology (ICDRET), 2009*, Dhaka: IEEE, 2009, pp. 1–6, ISBN: 978-1-4244-6012-0. DOI: 10.1109/ICDRET.2009.5454240.

[45] Weather Underground. (2014). Weather History for De Aar, South Africa | Weather Underground, [Online]. Available: http://www.wunderground.com/history/airport/FADY/2014/5/14/DailyHistory.html?req_city=De+Aar\&req_state=\&req_statename=South+Africa\&reqdb.zip=00000\&reqdb.magic=1\&reqdb.wmo=68538\&MR=1 (visited on 05/25/2014).

Appendix A:
Instrument details and specifications

Instrument Name: ImpedoDUO®.

Manufacturer: CTLab (Pty) Ltd.

Year Released: 2014.

Description

The ImpedoDUO® is a dual channel, multifunctional power quality monitoring instrument with GPS time synchronisation sampling. It contains two independent GPS synchronised units, with four current and voltage inputs. A rugged machined aluminium enclose are used as protection housing for the instrument.

(a) Front view (b) Rear view

Figure A-1: The ImpedoDUO®

All analogue signals are sampled at 0.5 MHz. The waveform is digitised, from which the parameters and events are calculated. The data is afterwards down-sampled to a user configurable range between 1 kHz - 50 kHz in order to reduce data size.

The Snapshot® and Xross-Trigger® synchronous measurement features are embedded in the sampling algorithms. The Xross-Trigger® mechanism enables a remote command via the IP network to all connected instruments to sample and store synchronised data samples that can collectively be displayed using Snapshot®.

The ImpedoDUO® is certified for the following metering applications:

- Power Quality: IEC 61000-4-30, Class A
- Billing Meter: IEC 62053-22/33, Class 0.2
- Harmonic and Inter-harmonics: IEC 61000-4-7
- Flicker Measurements: IEC 61000-4-15
- SCADA: IEC 61850

Connections and Interface Ports

- Two independent recording units per instrument, each with 4 × voltage and current inputs
- Baseline Linux processing with Android user interface
- Multi-touch man-machine screen interface
- 2 × Gigabit Ethernet ports
- 2 × powered USB 2.0 ports - 480 Mbit
- 2 × Embedded GPS units (1 per recording unit)

Measured Parameters

Table A-1: Parameters Measurable by the ImpedoDUO®

Voltage	Current	Power
Frequency	Waveform	Waveform
Waveform	Current Phasor	Active Power RMS
Voltage Phasor	Current RMS	Reactive Power RMS
Voltage RMS	Fundamental (%)	Apparent Power RMS
Nominal (%)	Phase Angle	Distinction Between Import and Export Power
Fundamental (%)	Unbalance (%)	Power Angle
Phase Angle	Zero, Positive and Negative Sequence Amplitude	kWh Metering
Unbalance (%)	Zero, Positive and Negative Sequence Angle	Power Factor
Zero, Positive and Negative Sequence Amplitude	Total Current Harmonic Distortions (CTHD)	IEC Conformance Flag
Zero, Positive and Negative Sequence Angle	Crest Factor	
Under Voltage Deviation	K-Factor	
Over Voltage Deviation		
Total Voltage Harmonic Distortions (VTHD)		
Flicker		

Appendix B:
Loop impedance tester specifications

Instrument Name: IMP57® 16th Edition.

Manufacturer: Hellermann Tyton Italia.

Year Released: 2013.

Instrument Details

The IMP57® is a 4-wire high-resolution loop impedance measurement and prospective short-circuit calculation device. The instrument was designed to conform to the following standards:

- EN 60909-0
- VDE 0413
- EN 61557-3

In addition to the afore mentioned standards the instrument also complies to the following criteria:

- EN 61010
- EN 61557

Over voltage category:

- CAT III 240 V (to ground)
- CAT III 415 V (between inputs)

Insulation:

- Class 2 - Double insulated

Environment:

- Reference temperature: 23°C ± 5°C
- Operating temperature: 0 °C - 40°C
- Storage temperature: -10 °C - 60°C
- Operating Humidity: < 80 % HR

Technical Features

The instrument capabilities are indicated as a % of reading plus the number of digits. Calibration and tests were done under following atmospheric conditions: a temperature of 23 °C ± 5 °C with a relative humidity less than 60% HR. The impedance meter is rated to perform measurements up to a maximum current of 202 A.

Table B-1: Tester impedance measurement capabilities

Impedance Measurement		
Range	**Resolution**	**Accuracy**
0.1 - 199.9 mΩ	0.1 mΩ	± 5% reading + 1 mΩ
200 - 1999 mΩ	1 mΩ	

Table B-2: Tester resistance and reactance measurement capabilities

Resistance and Reactance Measurement		
Range	**Resolution**	**Accuracy**
0.1 - 199.9 mΩ	0.1 mΩ	± 10% reading + 2 mΩ
200 - 1999 mΩ	1 mΩ	

Table B-3: Impedance tester prospective short circuit current capabilities

Resistance and Reactance Measurement		
Range	**Resolution**	**Accuracy**
0.0 - 1999.0 A	1.0 A	± 5% reading +1 mA
2.0 - 9.9 kA	0.1 kA	
10.0 - 1999.0 kA	1.0 kA	

Table B-4: Impedance tester voltage detection capabilities

Voltage Measurement		
Range (50 Hz±5%)	**Resolution**	**Accuracy**
190 ± 460 V	1.0 V	± 1.0% reading + 2 digit

Table B-5: Impedance tester frequency detection capabilities

Frequency Measurement		
Range	**Resolution**	**Accuracy**
47.5 -52.5 Hz	0.1 Hz	± 0.2 Hz

Appendix C:
Simulated PV power plant model

The 75 MW PV power plant model design in Simulink® comprised four main plant sections. Each section was identical in magnitude and design, the sub-system model of the PV plant sections and sub-sub system models of the DC-AC inverter and DC-DC boost converter with MPPT controller are presented in Figures C-1-C-4 below.

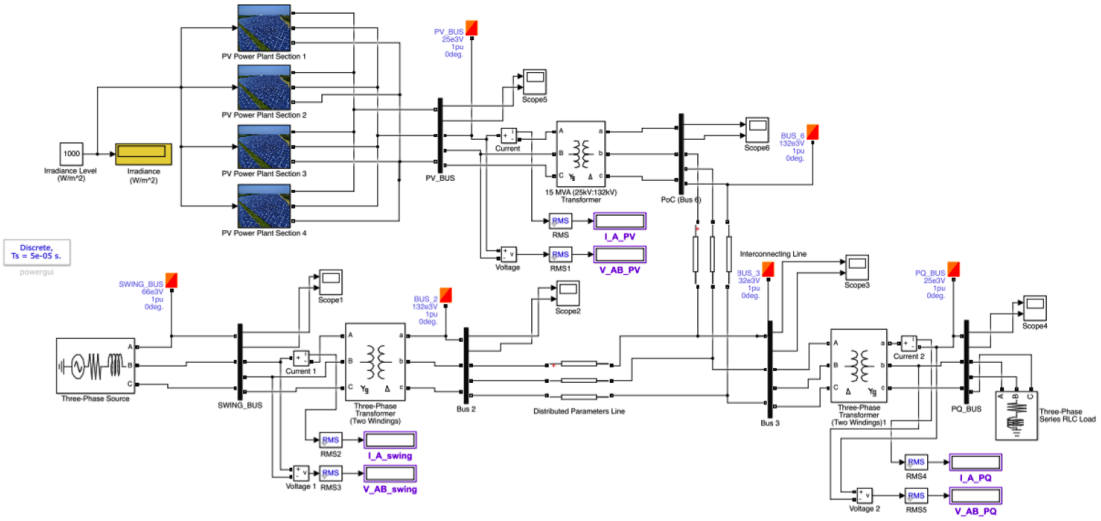

Figure C-1: The Simulink® model

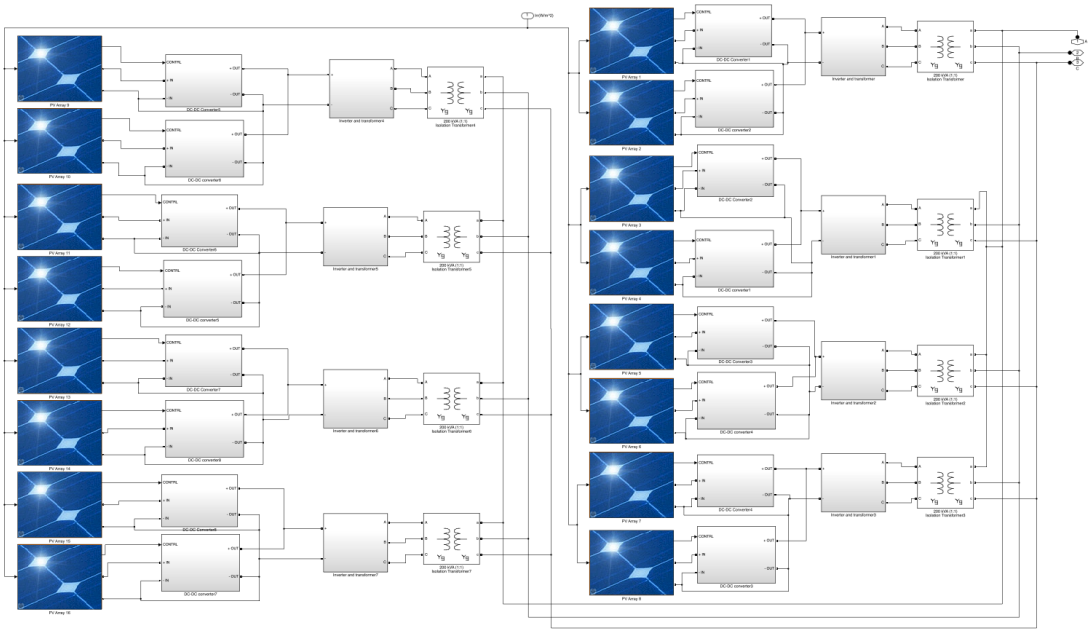

Figure C-2: Sub system model: Layout of PV plant section

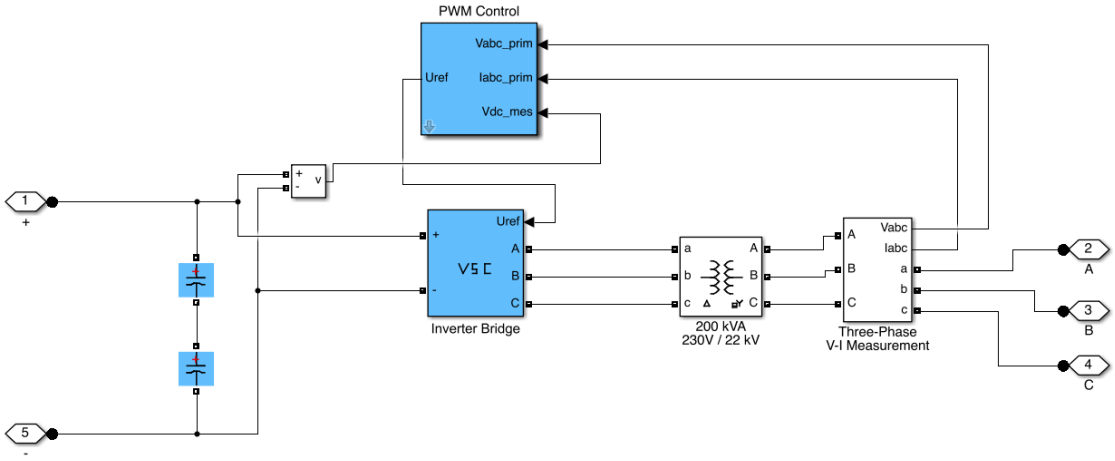

Figure C-3: Sub-sub system model: DC-AC Inverter

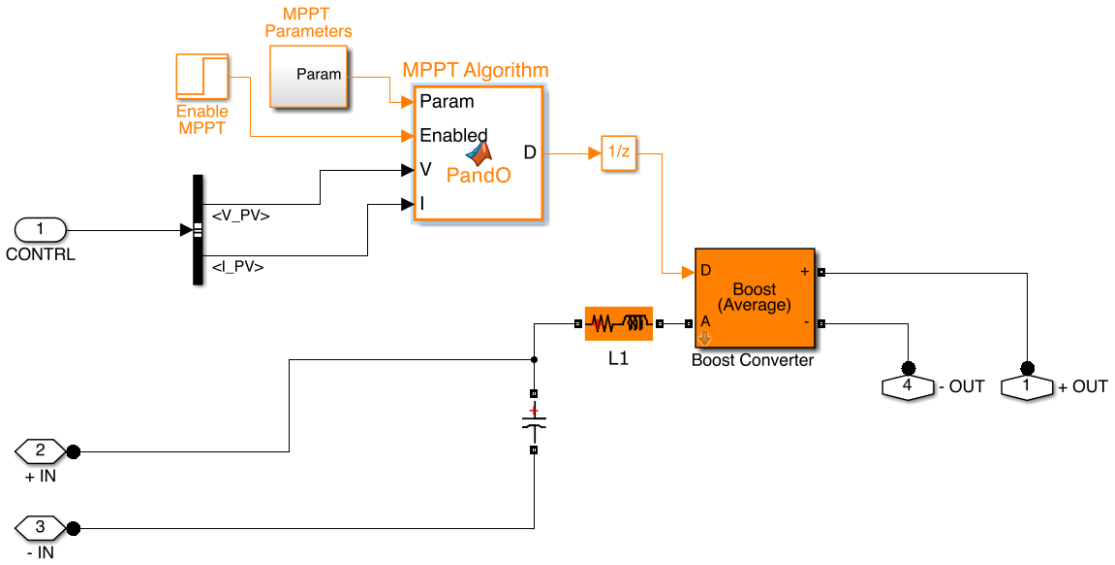

Figure C-4: Sub-sub system model: DC-DC Converter

Appendix D:
Weather report

Reported weather conditions during the field recordings [45].

Table D-1: Weather Report: 14 May 2014

Time (SAST)	Temp. (°C)	Dew Point (°C)	Humidity (%)	Pressure (hPa)	Visibility (km)	Wind Direct.	Wind Speed (km/h)	Precip. (%)	Events	Conditions
02:00	11	4	56	hPa	-	SE	7.4	-		
05:00	9	5	70	hPa	24	SSE	9.3	-		Haze
08:00	9	5	67	hPa	24	SSE	14.8	-		Haze
08:44	11	5	67	1027	0	ESE	13.0	N/A		Clear
09:47	14	5	48	1027	-	E	18.5	N/A		Clear
10:36	16	5	48	1026	-	E	14.8	N/A		Clear
11:00	17	5	34	hPa	40	E	13.0	-		Clear
11:36	19	5	40	1026	-	E	9.3	N/A		Clear
12:55	21	3	31	1024	-	N	9.3	N/A		Clear
14:00	22	3	19	hPa	40	NW	11.1	-		Scattered Clouds
17:00	20	1	18	hPa	40	WNW	13.0	-		Scattered Clouds
20:00	17	3	27	hPa	40	N	5.6	-		Clear
23:00	13	4	40	hPa	-	SE	7.4	-		